

## 5. SITE 835<sup>1</sup>

### Shipboard Scientific Party<sup>2</sup>

#### HOLE 835A

**Date occupied:** 31 December 1990  
**Date departed:** 2 January 1991  
**Time on hole:** 1 day, 15 hr, 12 min  
**Position:** 18°30.061'S, 177°18.162'W  
**Bottom felt (rig floor; m, drill-pipe measurement):** 2916.5  
**Distance between rig floor and sea level (m):** 10.81  
**Water depth (drill-pipe measurement from sea level, m):** 2905.7  
**Total depth (rig floor; m):** 3076.00  
**Penetration (m):** 155.5  
**Number of cores (including cores with no recovery):** 18  
**Total length of cored section (m):** 159.50  
**Total core recovered (m):** 160.07  
**Core recovery (%):** 100  
**Oldest sediment cored:**  
Depth (mbsf): 155.10  
Nature: volcanic siltstone  
Earliest age: late Pliocene  
Measured velocity (km/s): 1.6  
**Hard rock:**  
Depth (mbsf): 155.10  
Nature: basalt  
Measured velocity (km/s): 3.76  
**Basement:**  
Depth (mbsf): 155.10  
Nature: basalt  
Measured velocity (km/s): 3.76

#### HOLE 835B

**Date occupied:** 2 January 1991  
**Date departed:** 3 January 1991  
**Time on hole:** 1 day, 23 hr, 45 min  
**Position:** 18°30.050'S, 177°18.192'W  
**Bottom felt (rig floor; m, drill-pipe measurement):** 2916.5  
**Distance between rig floor and sea level (m):** 10.90  
**Water depth (drill-pipe measurement from sea level, m):** 2905.6  
**Total depth (rig floor; m):** 3099.50  
**Penetration (m):** 183.00  
**Number of cores (including cores with no recovery):** 7  
**Total length of cored section (m):** 49.8  
**Total core recovered (m):** 8.7

**Core recovery (%):** 17.5

**Oldest sediment cored:**  
Depth (mbsf): 155.50  
Nature: claystone  
Earliest age: late Pliocene  
Measured velocity (km/s): 2.1

**Hard rock:**  
Depth (mbsf): 155.50  
Nature: basalt  
Measured velocity (km/s): 4.62

**Basement:**  
Depth (mbsf): 155.50  
Nature: basalt  
Measured velocity (km/s): 4.62

**Principal results:** Site 835 is located in the west central Lau Basin, approximately 200 km east of the foot of the remnant arc of the Lau Ridge, and about 80 km west of the propagating ridge of the Central Lau Spreading Center (CLSC). The site is on crust about 3 m.y. old, according to the most consistent interpretations of magnetic anomaly patterns. Its regional setting is on the eastern flank of the broad, north-south bathymetric high centered on 18°35'S, 177°25'W, which rises to 1650 m from a water depth of around 2700 m in the vicinity of Site 834. The rocks forming the bathymetric high are of unknown composition, but they may represent the location of an extinct spreading ridge, abandoned after eastward migration or jump of the backarc spreading axis. The principal objectives of the site were (1) to assess the ages and chemistry of the basement rocks, and to determine their petrogenetic relationship to those recovered at Site 834; (2) to sample the overlying sedimentary sequence to review variations in carbonate, clay, and volcanoclastic components, and to assess their stratigraphic relationships to marker units identified at Site 834; and (3) to identify the tectonic setting of the site in terms of models of backarc ridge relocation by ridge jump, ridge migration, or asymmetric spreading.

The sedimentary sequence recovered at Site 835 consists of 155 m of clayey nannofossil oozes, mud-clast conglomerates, turbiditic foraminiferal sands and oozes, and clayey nannofossil mixed sediments (Fig. 1). Many of these units are interbedded with epiclastic and volcanic silt layers. These epiclastic layers are much more common below 130 mbsf. The sediments of Site 835 are divided lithologically into clayey nannofossil ooze (Unit I) and volcanic sand and silt (Unit II). Calcareous nannofossils are abundant and well preserved throughout sediments of all cores, but planktonic foraminiferal assemblages are less diverse and poorly preserved in Cores 135-835A-3H and -4H of Unit I and the lower part of Unit II. The sediments at this site range in age from middle Pleistocene to late Pliocene. The middle Pleistocene fauna occurs between Cores 135-835A-1H and -3H, and the boundary of the middle/lower Pleistocene is thought to be at the base of Core 135-835A-3H. The Pleistocene/Pliocene boundary (base of nannofossil Subzone CN14a of Okada and Bukry, 1980) is within Core 135-835A-9H. However, upper Pliocene calcareous nannofossils, ranging from Subzones CN12a to CN13a, were found from the lower part of Core 135-835A-6H to the upper part of Core 135-835A-8H. This section is interpreted as being allochthonous, emplaced as a slump block into the basin during the early Pleistocene. The sediments just above the basaltic basement contain late Pliocene fauna and flora, indicating Subzone CN12a of Okada and Bukry (1980) and Zone N21 of Blow (1969).

The lithostratigraphy of Site 835 can be correlated on sedimentologic criteria with that of Site 834, with 130 mbsf marking the boundary between Units I and II, also described at Site 834. However,

<sup>1</sup> Parson, L., Hawkins, J., Allan, J., et al., 1992. *Proc. ODP, Init. Repts.*, 135: Ocean Drilling Program (College Station, TX).

<sup>2</sup> Shipboard Scientific Party is as given in the list of participants preceding the contents.



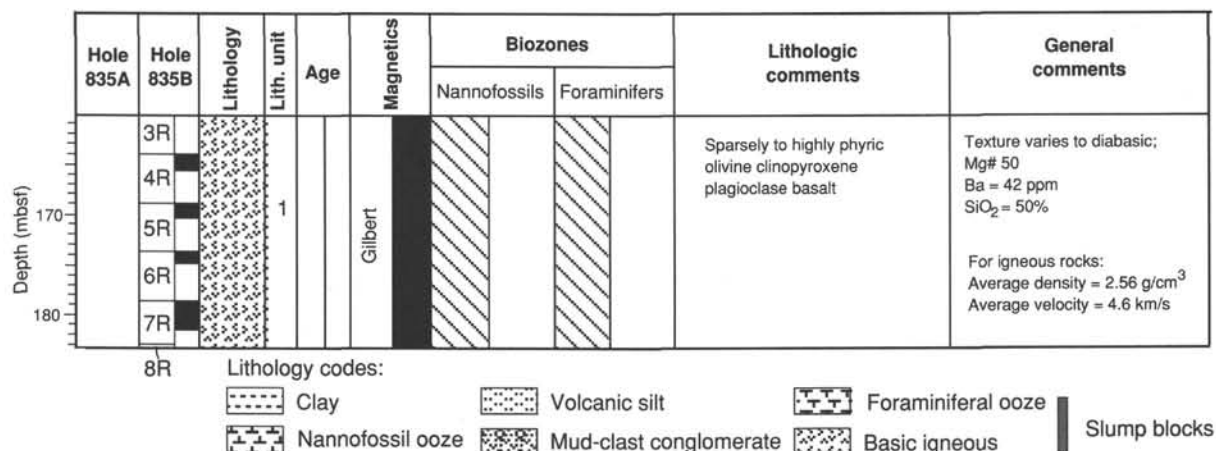


Figure 1 (continued).

Unit I at Site 835 is much thicker than at Site 834. At Site 835, it contains a significant proportion of resedimented material, including mud-clast conglomerates several meters thick that may possibly be debris-flow deposits. These are commonly overlain by thick turbidite deposits. Unit I at Site 835 also contains several more ashy horizons than the corresponding unit at Site 834.

The magnetostratigraphic record of the sediments of Hole 835A shows a complicated pattern of reversals that cannot be interpreted as a simple time sequence. Parts of the sequence appear to carry magnetic overprints, are tectonically or sedimentologically disturbed, and give scattered or abnormal remnant directions. Combining biostratigraphic information with the polarity record, it is possible to obtain a coherent stratigraphic interpretation, which suggests that the topmost 55 m of Hole 835A reaches back into the Jaramillo Subchron (ca. 0.95 Ma), overlying a slump or allochthonous unit showing truncated reversal sequences of parts of the Matuyama and Gauss polarity chrons. This allochthonous sequence in turn discordantly overlies the lowermost 84 m (69–153 mbsf) of the sequence, which covers the interval between the Jaramillo Event and the Gauss Polarity Chron, including the Mammoth Subchron (ca. 3.2 Ma).

Inorganic chemistry data from Site 835 were remarkably similar to those for Site 834, in that there was little change in the interstitial water chemistry throughout the section. This observation suggests that rapid seawater circulation in the sedimentary column is occurring here. Only background levels of hydrocarbons were detected throughout the section. A positive gas pressure was observed in Sections 135-835A-9H-5 and -6 at the surface, but was not caused by hydrocarbons. The identity of the gas is unknown, but it is likely it was carbon dioxide or air.

Sparsely to highly phyrlic, fresh to moderately altered olivine-clinopyroxene-plagioclase basalts were recovered from below 154.5 mbsf at Site 835. The basalts are highly variable with respect to grain size, degree of vesicularity, and overall texture, but there are enough mineralogical similarities to warrant the classification as a single unit. Porphyritic glassy pillow margins and diabasic fragments were recovered, with no clear relationship to depth in the core. Changes between these textural types are often gradational. The relative proportions of the silicate phases vary throughout the unit, but plagioclase and clinopyroxene dominate. The rocks are generally highly vesicular, except for the 2–3 cm adjacent to glassy margins. Many parts of the unit appear to have a fine-scale high porosity because of the abundance of microvesicles in the groundmass. Large (several centimeters), dark, globular regions are filled with very highly vesicular (70%–80%), quenched-textured basalt. These features are similar to those seen in many of the units at Site 834 and in rocks dredged elsewhere in the Lau Basin.

The physical properties of the sediments drilled at Site 835 show little change with depth or lithology, although slight changes in the velocity and the shear strength appear to be correlated with the base and top of the slumped Pliocene section. *P*-wave shear velocities within the basalts average 4.6 km/s, which is slightly higher than the uppermost basalts sampled at Site 834. The geothermal gradient, established by five temperature measurements in the sediments, is

extremely low for young crust (about 15°C/km), as compared with the 50°C/km gradient measured at Site 834. The low geothermal gradient and the minor change in physical properties with depth indicate that rapid fluid circulation through the sedimentary section may be dissipating heat derived from the young backarc crust.

Downhole logging measurements using the induction, sonic, and density tools at Site 835 readily distinguished sediments from igneous basement. Sedimentary interbeds among the flows showed low resistivity, bulk density, and sonic velocity and corresponding high porosity signatures. Logs provided strong evidence for the presence of sediment interbeds in areas of low recovery, particularly unit boundaries. The boundary between lithologic Units II and III was also tentatively recognized using a combination of chemical parameters on the unprocessed geochemical data. The FMS records processed on-board ship supported identification of variations in volcanoclastic input in the sediment units and aided structural interpretations for the basement section.

## BACKGROUND AND OBJECTIVES

### Background

#### Location and Bathymetry

Site 835 is located in the west central Lau Basin, approximately 100 km east of the foot of the remnant volcanic arc of the Lau Ridge, and about 90 km west of the propagating ridge of the CLSC (Fig. 2). According to the most consistent interpretations of magnetic anomaly patterns, the site overlies crust about 3 m.y. old. Its regional setting is in a fault-bounded graben more than 2900 m deep, which we informally refer to as "Basin 835" (Fig. 3). This trough is located on the eastern flank of a broad, north-south bathymetric high centered on 18°35'S, 177°25'W, which rises to about 1650 m at its summit. This shoal area corresponds to one of the upstanding blocks that, along with intervening broad basins and troughs, are recognized as characterizing the western Lau basin topography, as discussed in the "Introduction and Principal Results" chapter (this volume). The rocks forming the bathymetric high adjacent to Site 835 are of unknown composition; however, on the basis of correlation with rocks dredged from similar ridge structures in the southwestern Lau Basin, it is likely to be basalt and have a composition intermediate to arclike basalts and the MORB-like basalts of the CLSC (Hawkins and Melchior, 1985). Parson et al. (1990) suggested that this crest may represent the line of an extinct spreading ridge, abandoned after eastward migration (or jump) of the backarc spreading axis. Site 835 was placed to test this hypothesis.

In detail, Site 835 is located in 2916.5 m of water toward the eastern margin of Basin 835, a southerly tapering feature extending from 18°35'S northward to at least 18°24'S (Fig. 3). A morphotectonic synthesis of the area has been derived from a compi-

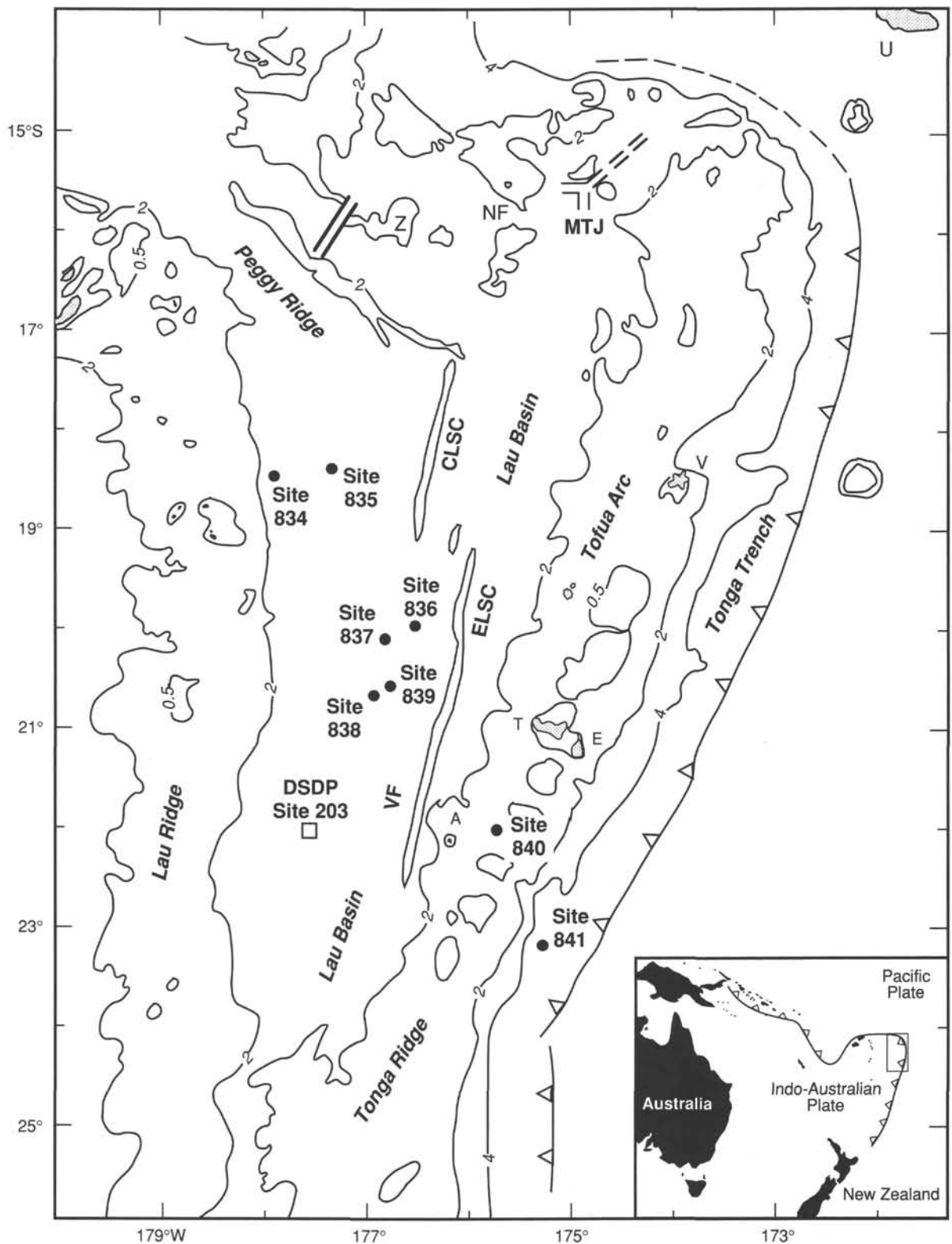


Figure 2. Regional bathymetry of the Lau Basin and location of Site 835. The figure also illustrates the regional setting for the locations of other drill sites in the Lau Basin and the major geologic features of the Tonga Trench and Lau Basin system. Z = Zephyr Shoal; islands include T = Tongatapu, E = 'Eua, V = Vavau, NF = Niua Fo'ou, A = Ata, and U = Upolu. Locations of the Central Lau (CLSC) and Eastern Lau (ELSC) spreading centers, Valu Fa (VF) Ridge, and Mangatolu Triple Junction (MTJ) are from von Stackelberg (1990), Parson et al. (1990), Hawkins et al. (1989), and Nilsson et al. (1989). The location of DSDP Site 203 is shown as an open square. Contours in thousands of meters.

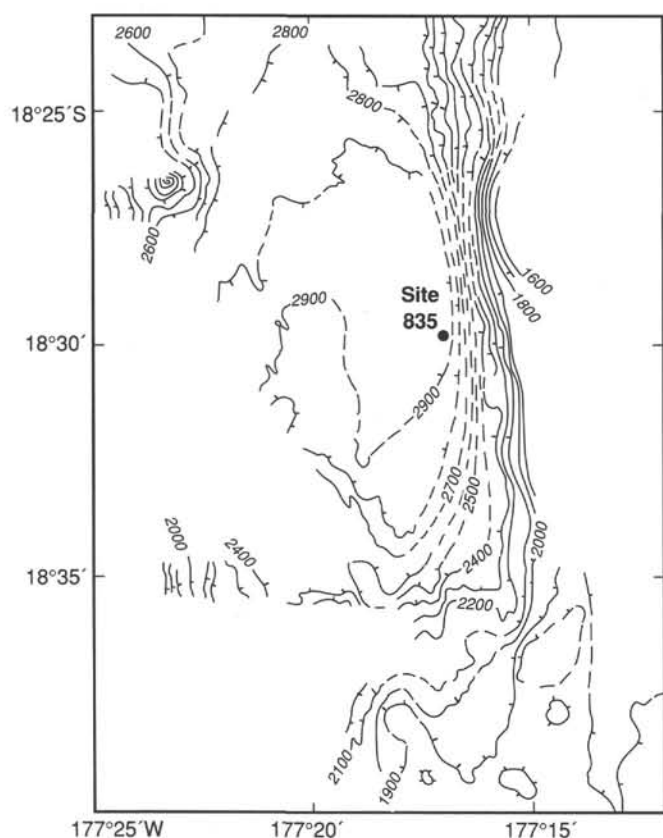


Figure 3. Detailed bathymetry at Site 835 based on SeaBeam and conventional bathymetric profiles. Contours in meters.

lation of sidescan sonar and swath bathymetric data (Fig. 4). Parts of the basin close to the drill site exceed 2900 m water depth, and the regional bathymetric floor drops steadily toward the north to more than 3000 m. The basin is locally flanked by scarps that rise to the east and west by 1150 and 200 m, respectively. A number of isolated seamounts rising to <2000 m have been mapped to the west of the basin, and their images show up well on SeaBeam and GLORIA long-range sidescan sonar records (Parson et al., 1990, and this volume).

Long-range sidescan sonar (GLORIA) and multibeam bathymetric data define a regional linear tectonic fabric trending north through the area; this fabric is defined by highly backscattering linear features approximately 0.5 km in width and up to 20 km in length (Parson et al., this volume). These are interpreted as a complex series of faults, with the scarp faces showing a consistent sense of facing inward to Basin 835. This facing direction, similar to that described at slow spreading mid-ocean ridges, has been part of the evidence used to support models of an arcward ridge jump considered by previous workers (Parson et al., 1990). Less convincing evidence based on the correlation of poorly developed magnetic anomaly patterns is discussed below and in the "Introduction and Principal Results" chapter (this volume).

#### Geologic Setting

The geological setting of Site 835 is similar to that of Site 834, in that it lies within the western Lau Basin between the CLSC and the Lau Ridge on crust of unknown composition and age. We will give a brief outline of the regional geology of the site; a more detailed discussion is given in the "Introduction and Principal Results" chapter (this volume).

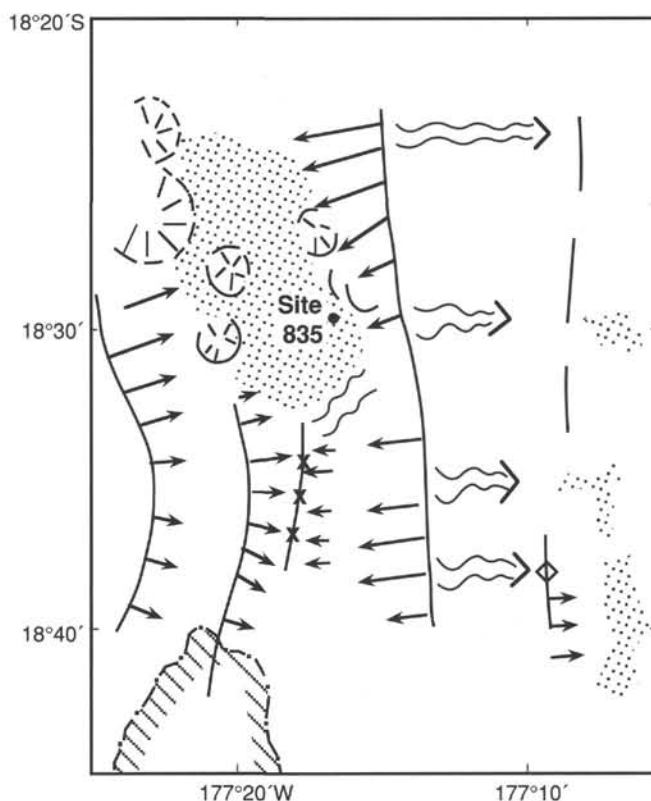


Figure 4. Morphotectonic summary of the area around Site 835. Continuous bold lines locate scarp shoulders, arrows indicate slope down and facing direction. Stipple locates planar, flat-lying basin floor. Subcircular features are interpreted as submarine volcanoes. Hatched area is high backscatter zone on GLORIA sidescan, suggesting possible neovolcanism. Wavy paired lines indicate areas of hummocky or undulose stratified sediment. Standard antiformal and synformal structural annotation.

The CLSC is a major morphologic/tectonic feature of the Lau Basin and is presently the site of magma leakage and backarc spreading at the latitude of Site 835 (Fig. 2). The CLSC is propagating southward into the basin at the expense of the Eastern Lau Spreading Center (ELSC), approximately along the line of longitude of 176°30'W. The regional fabric is defined by the predominantly inward-facing fault pattern, which in this area varies from 350° to 010° azimuth. This fault pattern can be seen to be both locally controlling and being cut by the propagator. The age of the CLSC is equivocal because the magnetic anomaly pattern is unclear, but it appears to have initiated from the southeastern termination of the Peggy Ridge and has advanced southward for at least 1 m.y. and possibly as much as 2 m.y. The propagator tip is located at around 19°16'S, 176°32'W, some 120 km from Basin 835. Rocks from the CLSC include depleted N-MORB-type tholeiitic basalts and fractionated basalts, "oceanic andesites and dacites," and Fe-Ti basalts (Hawkins, 1974, 1976, 1989; Hawkins and Melchior, 1985).

Nearly 200 km to the northeast of Site 835, the northwest-striking Peggy Ridge truncates the western sector of the central Lau Basin. Rising to less than 1000 m, the ridge extends over 300 km northwest from the northern limit of the CLSC axis. It presently marks a line of right-lateral motion associated with the spreading on the CLSC coupled with a component of east-west backarc extension associated with the spreading on the CLSC. It was originally proposed that the Peggy Ridge was a spreading center

(Chase, 1971), but Sclater et al. (1972) demonstrated that this speculation was not supported by the magnetic data and proposed instead that it marked the location of a major subplate boundary that was possibly acting as a transform fault. This interpretation is supported by the first-motion earthquake data of Eguchi (1984) and more recently by Hamburger and Isaacs (1986). Rocks from the Peggy Ridge are tholeiitic basalt and are generally similar to the depleted N-MORB-type basalts that characterize the CLSC (Hawkins, 1974, 1976; Hawkins and Melchior, 1985).

The western side of the Lau Basin is bounded by the islands and atoll reefs of the Lau Ridge, the arcs of which lie some 130 km west of Site 835. It comprises emergent and coral-capped parts of a remnant volcanic arc, active until the late Miocene or early Pliocene, or 5–3.5 Ma (Gill, 1976; Cole et al., 1985; Woodhall, 1985). The Lau Ridge is postulated to be a remnant of a more extensive volcanic arc that originally included part of the present Tonga Ridge. The Tonga Ridge (frontal arc) comprises the active volcanic arc (the Tofua Arc) and Pliocene to Holocene platform limestone and atoll reefs capping a “basement” presumed to be igneous crust. It has been generally accepted that the Tonga Ridge separated from the Lau Ridge during the extensional development of the Lau Basin (e.g., Karig, 1970; Sclater et al., 1972; Hawkins, 1974; Woodhall, 1985; Cunningham and Anscombe, 1985). A more complete discussion of the geology of the Tonga and Lau ridges is in the “Introduction and Principal Results” chapter (this volume).

### Seismic Stratigraphy

Published and unpublished single-channel and multichannel seismic reflection data have been used to assess the tectonic setting of Site 835 in the context of the geological evolution of the Lau Basin region (Hawkins, 1988, 1989; Parson et al., 1989). The ships' tracks on which these data have been recorded are given in Figure 5A. Ship tracks for the *JOIDES Resolution* site survey and approach are illustrated in Figure 5B. Seismic reflection profiler data collected during the pre-site survey is included in Figure 6A as well as seismostratigraphic interpretation and line drawing interpretations in Figures 6B–6C. A full description of the seismic stratigraphy throughout the Lau Basin is included in the “Introduction and Principal Results” chapter (this volume), and so we have only summarized the details relevant to Site 835 here.

Figures 6A–6B illustrate seismic reflection data recorded by the *JOIDES Resolution* across Site 835. In the vicinity of the site, the seismic reflection profiles indicate a 0.183-s-thick TWT sedimentary section overlying an irregular acoustic basement. The basement appears as a blocky, stepped surface, provisionally interpreted as a normally faulted extensional rift fabric. The upper 0.08 s TWT of the seismic section is obscured by the decaying water-gun pulse, but the lower part of the section down to basement is imaged as a weakly layered seismic unit, with flat-lying, closely spaced reflectors. At the eastern margin of the basin, the regional uppermost seismic Unit A (see “Introduction and Principal Results” chapter, this volume) is interrupted on a number of parallel seismic reflection profiles by a westerly tapering transparent unit that transgresses the lower seismic events of the decaying water-gun pulse (Fig. 6B). The unit is interpreted as a wedge-shaped slide or slump mass-wasted from the eastern scarp (see “Biostratigraphy” and “Paleomagnetism” sections, this chapter). To the east, at its shallowest, the upper surface of this unit is at around 0.06 s TWT below seafloor and overlies a planar acoustic horizon that we interpret to be a paleosurface at around 0.08 s TWT below seafloor. An approximate maximum thickness for the allochthonous unit is 18 m.

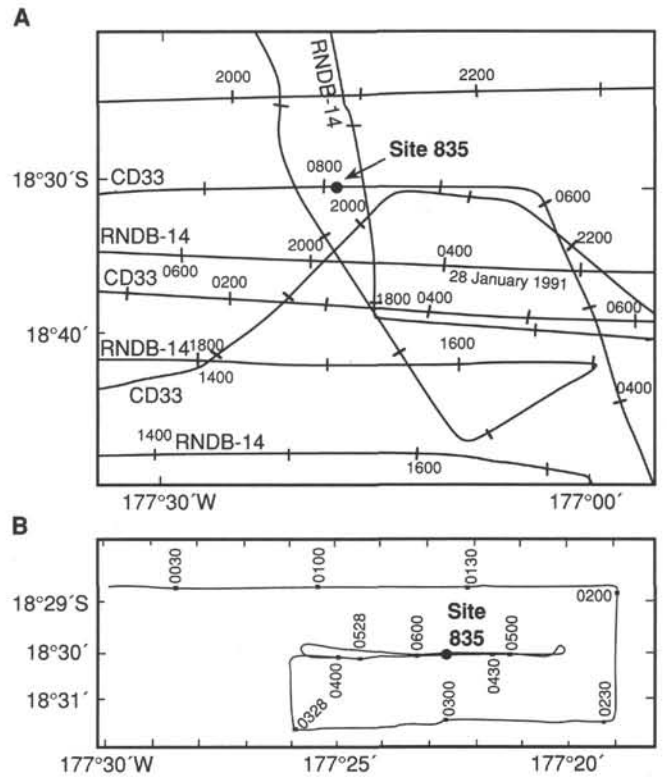


Figure 5. A. Track chart showing lines of *Charles Darwin* (CD33, Parson et al., 1989) and *Thomas Washington* (RNDB-14, Hawkins, 1989). B. Track chart of the site approach and survey lines of *JOIDES Resolution* at Site 835.

### Magnetic Data

As discussed in the “Introduction and Principal Results” chapter (this volume), the magnetic data for the Lau Basin have proved difficult to interpret. Attempts to model the crustal structural fabric and ages of magnetic lineations in terms of plate tectonic theory have met with only limited success and have yielded widely varying interpretations for the age of the earliest backarc crust in the Lau Basin. These ages range from an original estimate of 5–10 Ma (Sclater et al., 1972) to 3 Ma (Malahoff et al., 1982). Some of the rationale for drilling at Sites 834, 835, and 836 was to resolve uncertainties about the age of the beginning of opening of the basin.

Weissel (1977) identified anomalies as old as 2' (3 Ma) in the western Lau Basin between 17°00'S and 18°45'S. He suggested that the seafloor occupying the intervening basin between these anomalies and the eastern flank of the Lau Ridge aged westward and was generated at an earlier zone of magmatic accretion, active between 3 and 6 Ma. These ages are the equivalent to ages of volcanic rocks from the Lau Ridge (Gill, 1976). The most recent revision of the aeromagnetic data (Malahoff et al., in press) indicates the presence of a 3' anomaly (5.8 m.y.) along the western foot of the slope of the Lau Ridge. Site 835 is situated in the eastern part of this zone of “old anomalies.” If the crust at Site 835 has been generated by “normal” seafloor spreading, the best age estimate is around anomaly 2' (between 3.4 and 2.5 Ma). A new compilation of marine and aeromagnetic data is presented in Figure 7, combined with a provisional interpretation revised from Murthy (1990). North-south linear correlations of profile anomalies are possible over only a maximum of 35 km, and anomaly

amplitude is highly variable throughout. Local along-strike variations between 300 and -250 nT over periods of 25 km are common.

### Scientific Objectives

Site 835 was planned as the intermediate age site along a west to east transect expected to sample progressively younger crust from a site near the Lau Ridge remnant arc to sites on relatively young crust near the active axial ridge. The scientific objectives for Site 835, as for the other sites drilled on Leg 135, were to sample the sedimentary column and the igneous "basement" and to collect paleontologic and geophysical data in order to understand the geologic evolution of the Lau Basin. Although this transect was not on a true time-flow line, we hoped that an evolutionary pattern from old to young crust would be established. The data would be important not only for regional geology but also for comparing the history of the Lau Basin with that of other western Pacific backarc basins to improve our models for backarc basin evolution.

Site 835 was selected to sample crust thought to have been formed in the earliest stages of basin extension. Specific objectives were as follows:

1. To obtain samples of the igneous rocks that form the basement to the sedimentary fill. It was assumed that the basement would be oceanic crust formed during the spreading of the basin, and that recovery of samples and the basal sedimentary sediments would give information about the timing of crustal accretion as well as the composition of the contributing magma source, or sources. It is recognized that the history of the Lau Basin may have been much more complex than that implied by a simple rifting model where old crust is ruptured and is replaced by new oceanic crust (see models discussed in the "Introduction and Principal Results" chapter, this volume). Other models for basin evolution are equally plausible; the basins may represent fault-bounded basins underlain by blocks of tilted and attenuated arc/forearc crust overlain by a composite filling of sediments and flows, sills, and dikes of basalt. The sediments may have been derived from several different sources including the Lau Ridge, local "basement" ridge(s), and pelagic input. The petrology and chemistry of the igneous rocks forming the basement or fill in the basins would be critical in determining whether or not oceanic or arc material, or a hybrid mixture of the two, is the major component of the crust. The chemical signature of flows, dikes, or sills recovered at the site would provide crucial information concerning the nature of the source or sources for the lavas, and the petrologic evolution of basement constituents. A more complex model for Lau Basin evolution can be envisaged in which the anomalous topography of the western part of the Lau Basin has developed through the repeated rifting and formation of volcanic constructs, before establishing a conventional seafloor spreading center (e.g., the ELSC) adjacent to the present arc. The striking contrast in the basement topography as interpreted from GLORIA and SeaBeam data supports this suggestion of a protracted period of spreading-axis formation (Parson et al., this volume).

2. To core the sediment column to get a record of the history of basin subsidence and sedimentation. These samples would enable us to investigate the petrology, stratigraphy, and paleontology of the sedimentary column and to understand the depositional environment, the provenance of the sediments, sediment accumulation rates, and the alteration and diagenesis of the sediments. Volcanism was active on the nearby Lau Ridge during the Miocene and the Pliocene, and the presence of interbedded ash layers and fossiliferous horizons in the basin would help in recognizing episodicity in this volcanism. The cores would also be useful in interpreting the record of the subsidence history of the

Lau Basin and the concurrent uplift and erosion history of the Lau Ridge. In more detail, the combination of facies variations, structural controls on the form and degree of sedimentary transport linkage of the basins and sub-basins, and regional provenance studies would offer a powerful control on sedimentation patterns within the evolving backarc basin. The quantification of effects of hydrothermal activity on the sediments, and their variations in input and chemistry would help to constrain models of ridge activity and hydrothermalism.

3. To determine the regional relations among lithostratigraphy, biostratigraphy, and magnetic stratigraphy, combine these results with those from other sites, and use these data to determine the age of the beginning of crustal extension and magmatic activity in the Lau Basin and the record of Lau Ridge volcanism as expressed in the clastic rocks and ash layers of the sedimentary fill.

4. To establish the age of the crust underlying the adjacent bathymetric high to test suggestions of the presence of an extinct north-south spreading axis in the vicinity of the site. In the event of establishing the presence of an extinct spreading ridge proximal to the site, the objective would be to identify the petrological signature of a dying ridge system.

## OPERATIONS

### Transit to Site 835

The *JOIDES Resolution* left Site 834 at 2100 hr UTC on 30 December 1990, taking a westerly course for 4 nmi before turning to make a final easterly pass through the site at 6 kt. This additional line was collected to secure a further 3.5-kHz high-resolution seismic profile for correlation with the site lithostratigraphy (see "Lithostratigraphy" section, this chapter). Full transit speed was resumed at 2200 hr UTC on 29 December 1990, and passage was then made to Site 835, 61 km to the east. A site survey began at 0018 hr UTC on 31 December and was completed by 0514 hr UTC (Fig. 5B). Weather conditions were good, with mild sea state and light winds.

### Site Approach and Site Survey

Site 835 is situated in a linear, north-south, parallel-sided basin characterized by a flat, sedimented floor that deepens to more than 2900 m water depth. The basin is approximately 7.5 km wide at its widest point. The basin floor tapers and gradually shoals toward the north and south, reaching <5 km width and >2800 m water depth by 18°23'S. The flat-lying floor is interrupted in the south about 5.5 km from the site by a complex series of discrete ridges and minor fault scarps. In addition, several isolated and subcircular seamounts can be identified within the valley on both long-range sidescan sonar and multibeam swath bathymetry records (Figs. 3-4).

The Site 835 area was selected using a number of intersecting single-channel seismic reflection profiles acquired by the *Charles Darwin* and the *Thomas Washington* during 1988 and 1989, respectively, and relevant tracks from these surveys are located in Figure 5A. These data were used to identify a suitably thick (i.e., >100 m) sedimentary section overlying acoustic basement, in a water depth of 2916 m. Seismic profiles recorded by the *JOIDES Resolution* during the pre-site survey illustrate a seismic sequence that comprises a series of subparallel planar acoustic reflections defining a basin flanked by steep scarps, which converge at depth to form a notch in the acoustic basement at a depth of 0.16 s below seafloor (Fig. 6). The acoustic basement (see "Background and Objectives" section, this chapter) is defined here by a series of hummocky surfaces characterized by a series of stacked, low-frequency seismic reflectors. The experience of sampling a relatively low-velocity sedimentary sequence (*P*-wave

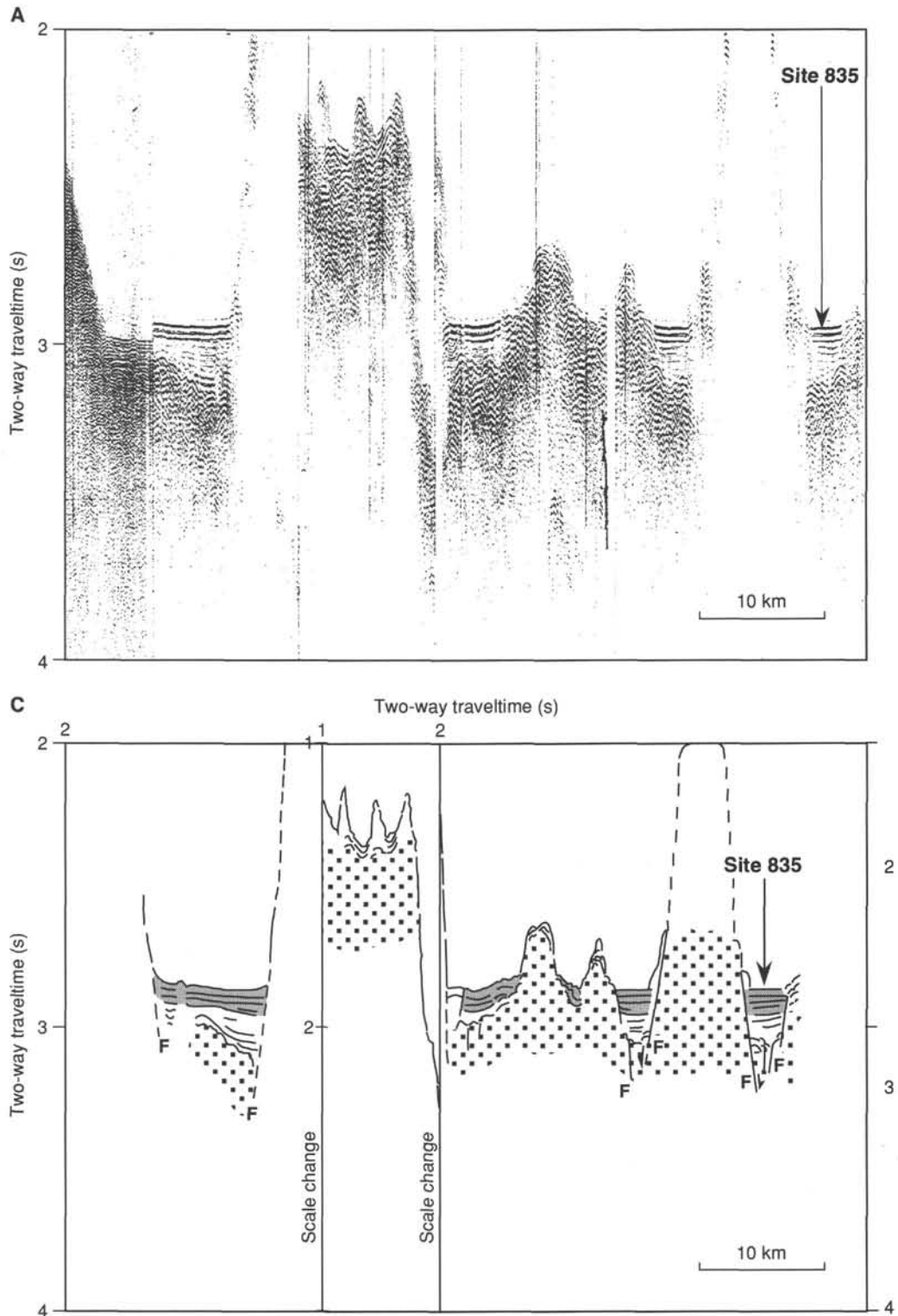


Figure 6. Seismic data for Site 835. **A.** Single-channel seismic reflection profile across Site 835, recorded by *JOIDES Resolution*. **B.** Lithostratigraphic correlation to seismic stratigraphy. **C.** Line drawing interpretation of seismic profile of Figure 6A. Bold stippled areas identify the acoustic basement; lighter stippled area, seismic Unit A; the unornamented section is interpreted as seismic Unit B. F = fault.

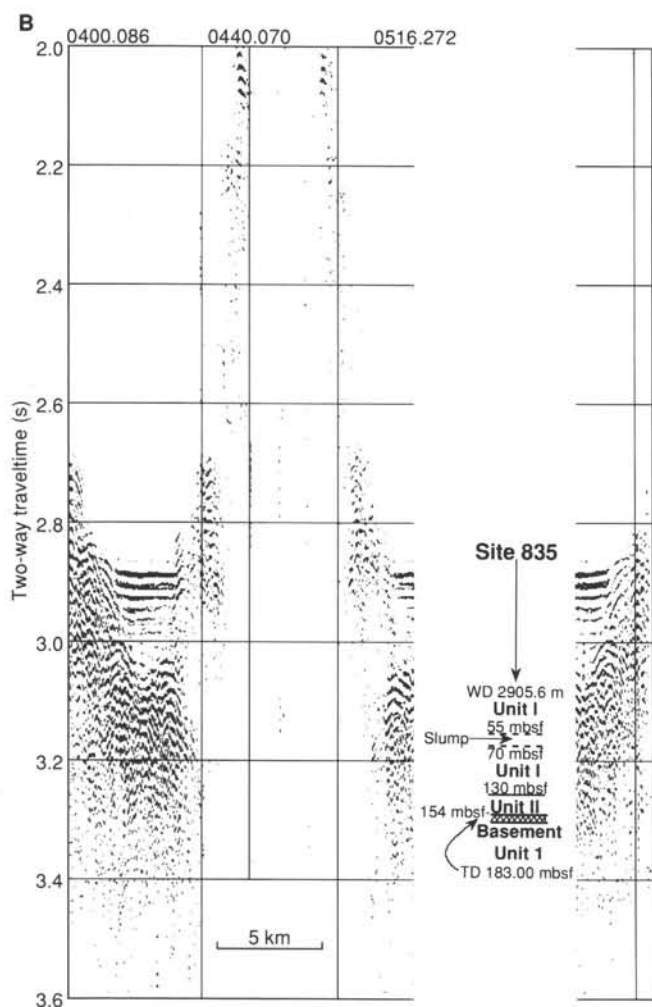


Figure 6 (continued).

velocity of 1500 m/s) at Site 834 led us to estimate a sedimentary thickness at the site of about 120 m. To ascertain the regional seismic stratigraphy and structure of the basin, two short east-west seismic profiles were collected using the full shipboard underway geophysics system during the pre-site survey to bracket the site (Fig. 5B).

To conduct the pre-site survey, the ship slowed at 0018 hr UTC on 31 December to deploy the underway geophysical equipment, comprising two 80-in.<sup>3</sup> water guns, the single-channel 60-element Teledyne hydrophone, and the magnetometer (Fig. 5B). This was completed by 0514 UTC, ending after a final east-west survey line was taken through the site to drop the beacon at 0516 UTC, at 18°29.99'S, 177°18.156'W. Underway geophysical gear was recovered after completing the pass across the basin, with the ship returning to the site to begin coring operations at 0630 UTC on 31 December 1990.

### Drilling and Logging Summary

Our plan was to drill two adjacent holes at Site 835, with the principal objective of attaining 50 m of basement penetration. Hole 835A was planned to be cored with the advanced hydraulic piston corer (APC) and the extended core barrel (XCB), with the goal of obtaining a complete and relatively undisturbed sediment section. Hole 835B was to be an rotary core barrel (RCB) hole that washed through most of the sediments, beginning coring just

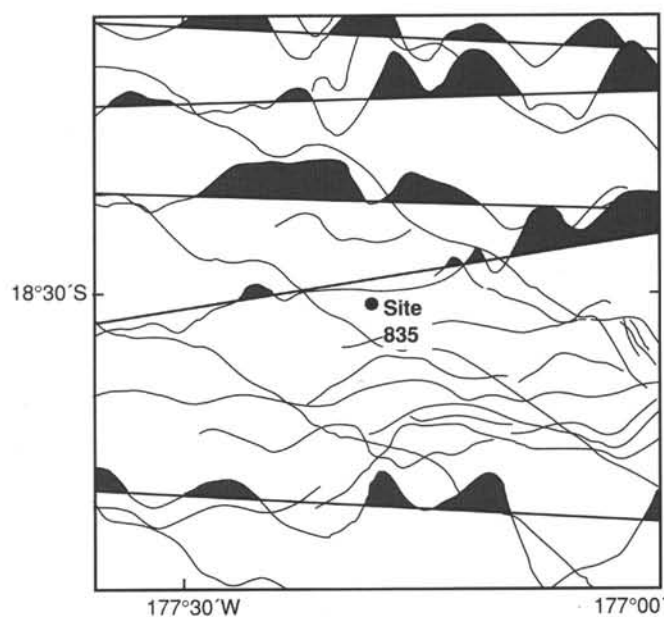


Figure 7. Magnetic anomaly data plotted along track for the area of Basin 835. Maximum positive anomalies do not exceed 200 nT, and positive portions of representative profiles are shaded.

above the sediment-basement interface and continuing to 50 m basement penetration or bit destruction. The sedimentary section and sediment-basement interface in Hole 835B would then be logged.

### Hole 835A

Hole 835A was spudded in at 1313 UTC, 31 December 1990, at 18°30.061'S, 177°18.162'W after the initial water core failed to establish the mud line. Spud Core 135-835A-1H was shot at 2916.5 m and recovered 9.59 m. This depth was accepted as the mud line. Seventeen cores (135-835A-1H to -17H) were taken with the APC down to 154.5 mbsf, for a recovery of 159.38 m (103.2%) of nanofossil clays and ooze. A nonmagnetic drill collar was used, and oriented cores were taken using the multishot tool on Cores 135-835A-3H to -17H (Table 1). Temperature measurements were made with the downhole water sampler temperature probe (WSTP) at 38.0, 57.0, 76.0, 95.0, 114.0, 133.0, and 154.5 mbsf. A 2.5-m partial stroke at Core 135-835A-17H ended the APC sampling at 1110 hr UTC. A single XCB core (135-835A-18X) was then taken from 154.5 to 159.5 mbsf, with 5 m cored and 0.69 m recovery (13.8%) in basalt. The sediments appeared stiff at depth for the most part, although very loose muds occurred just above mid-section, at 57.0–58.0 mbsf. Core liners were split from Cores 135-835-15H downward, with Core 135-835-17H recovering only 1.86 m of indurated sediment and basalt fragments.

Paleomagnetic measurements detected a 30° offset in the orientation of the APC cores in Hole 834A. Subsequent inspection of the orienting tool found a defective piston-rod lock pin, resulting in a 30° error in orientation of all cores from Sites 834 and 835.

### Hole 835B

The ship was positioned 20 m north of Hole 835A, and Hole 835B was spudded in at 0506 hr UTC on 2 January 1991, at 18°30.050'S, 177°18.192'W. The water depth indicated by the precision depth recorder (PDR) was the same as for Hole 835A, and two punch cores were taken to establish the mud-line level at

Table 1. Coring summary, Site 835.

Core no.	Date (1990-91)	Time (local)	Depth (mbsf)	Cored (m)	Recovered (m)	Recovery (%)	Age
135-835A-							
1H	Dec 31	1230	0.0-9.5	9.5	9.59	101.0	Pleistocene
2H	Dec 31	1330	9.5-19.0	9.5	9.74	102.0	Pleistocene
3H	Dec 31	1450	19.0-28.5	9.5	9.77	103.0	Pleistocene
4H	Dec 31	1540	28.5-38.0	9.5	9.98	105.0	Pleistocene
5H	Dec 31	1745	38.0-47.5	9.5	9.96	105.0	Pleistocene
6H	Dec 31	1835	47.5-57.0	9.5	9.94	104.0	upper Pliocene
7H	Dec 31	2050	57.0-66.5	9.5	9.94	104.0	upper Pliocene
8H	Dec 31	2140	66.5-76.0	9.5	9.97	105.0	Pleistocene
9H	Jan 1	0025	76.0-85.5	9.5	9.96	105.0	upper Pliocene
10H	Jan 1	0115	85.5-95.0	9.5	9.96	105.0	upper Pliocene
11H	Jan 1	0417	95.0-104.5	9.5	9.92	104.0	upper Pliocene
12H	Jan 1	0500	104.5-114.0	9.5	9.84	103.0	upper Pliocene
13H	Jan 1	0700	114.0-123.5	9.5	9.46	99.6	upper Pliocene
14H	Jan 1	0745	123.5-133.0	9.5	9.99	105.0	upper Pliocene
15H	Jan 1	0940	133.0-142.5	9.5	9.53	100.0	upper Pliocene
16H	Jan 1	1025	142.5-152.0	9.5	9.98	105.0	upper Pliocene
17H	Jan 1	1110	152.0-154.5	2.5	1.85	74.0	upper Pliocene
18X	Jan 1	1410	154.5-159.5	5.0	0.69	13.8	upper Pliocene
Coring totals				159.5	160.07	100.4	
135-835B-							
1R	Jan 2	0520	0.0-11.5	11.5	0.19	1.7	Pleistocene?
2R	Jan 2	0840	144.7-154.3	9.6	0.55	5.7	upper Pliocene
3R	Jan 2	0945	154.3-164.0	9.7	1.63	16.8	upper Pliocene
4R	Jan 2	1200	164.0-169.0	5.0	1.17	23.4	
5R	Jan 2	1405	169.0-173.7	4.7	1.03	21.9	
6R	Jan 2	1650	173.7-178.7	5.0	0.83	16.6	
7R	Jan 2	1945	178.7-183.0	4.3	3.27	76.0	
8M	Jan 2	2000	183.0	0	0.19	N/A	
Coring totals				49.8	8.86	17.8	

Note: Core 135-835B-8M represented no advance. N/A = not applicable.

2916.5 m below rig floor (mbrf). A 9 $\frac{7}{8}$ -in. hole was drilled from 11.2 to 144.7 mbsf. Cores 135-835B-2R to -7R were taken from 144.7 to 183.0 mbsf, with 38.3 m cored and 8.48 m recovered (22.1% recovery; Table 1). The objective was to penetrate basement to a depth of 50 m; however, the relatively young basalt proved to be highly unstable, causing high infill rates. Core 135-835B-8M was the final recovery attempt, but it recovered only drilling rubble with no additional penetration. Coring ended with 41 m of basalt penetration.

After conditioning the hole for logs with a short trip of the drill string, the bit was dropped using the hydraulic bit release (HBR). The open end of the pipe was pulled to 82.6 mbsf, and logging began at 0200 hr UTC on 3 January 1991. The Schlumberger "Quad Combo" tool rig was split into two parts, minimizing the tool length, and thus affording the best chance of penetration into the basement section and the logging of the basement/sediment interface. Mainly because of unfavorable hole conditions indicated by caving-in of the lower section, we decided not to run the geochemical tool and risk losing it in the hole. The lack of a good basement section precluded the use of the borehole televiewer (BHTV) at this site. The order of tool runs was as follows:

Run No. 1: Formation microscanner (FMS)/gamma ray. The FMS failed the surface calibration, and a backup tool had to be rigged, losing 1 hr, 15 min. The log found bottom at 15.0 m above the drillers' total depth and took a further 2 hr, 35 min to run.

Run No. 2: Induction/sonic. The log found bottom 15.0 m above the drillers' total depth and took 2 hr, 40 min to run.

Run No. 3: Density/neutron. The log found bottom 11.5 m above the drillers' total depth and required 2 hr, 40 min to run.

The HBR cleared the seafloor at 1605 hr UTC on 3 January 1991. The Datasonics beacon was recalled, but it did not release. The *JOIDES Resolution* left Site 835 at 2118 hr UTC for the transit to begin the site survey around Site 837.

## LITHOSTRATIGRAPHY

### Introduction

The sedimentary sequence recovered at Site 835 consists of 155.1 m of clayey nannofossil oozes, turbiditic foraminifer sands and oozes, mud-clast conglomerates, and clayey nannofossil mixed sediments. Frequently, these units are interbedded with epiclastic vitric volcanic silt layers. The epiclastic layers are much more common below 130 mbsf. The age of the sedimentary sequence ranges from the late Pliocene to the Holocene. Below 155.1 mbsf, vesicular basalts were cored.

Two holes were drilled at Site 835 (Table 1; see "Operations" section, this chapter). All sediment cores were visually described and sampled for smear slide description, carbonate analysis, vitric ash refractive index, and X-ray diffraction (XRD) studies. Our lithologic summary (Fig. 8) is derived from a composite of both holes. We have divided the sedimentary sequence at Site 835 into two lithologic units, based on differences in sediment composition, particularly on the occurrence of epiclastic vitric volcanic sands and silts (Fig. 9). Downcore color variations in the calcareous sediment sections of Hole 835 are shown in Figure 9, with color designations being taken from the 10YR HUE of the Munsell color chart (1975). These have been grouped into nine fields using the same scheme as for Hole 834 (see "Lithostratigraphy" section, "Site 834" chapter, this volume).

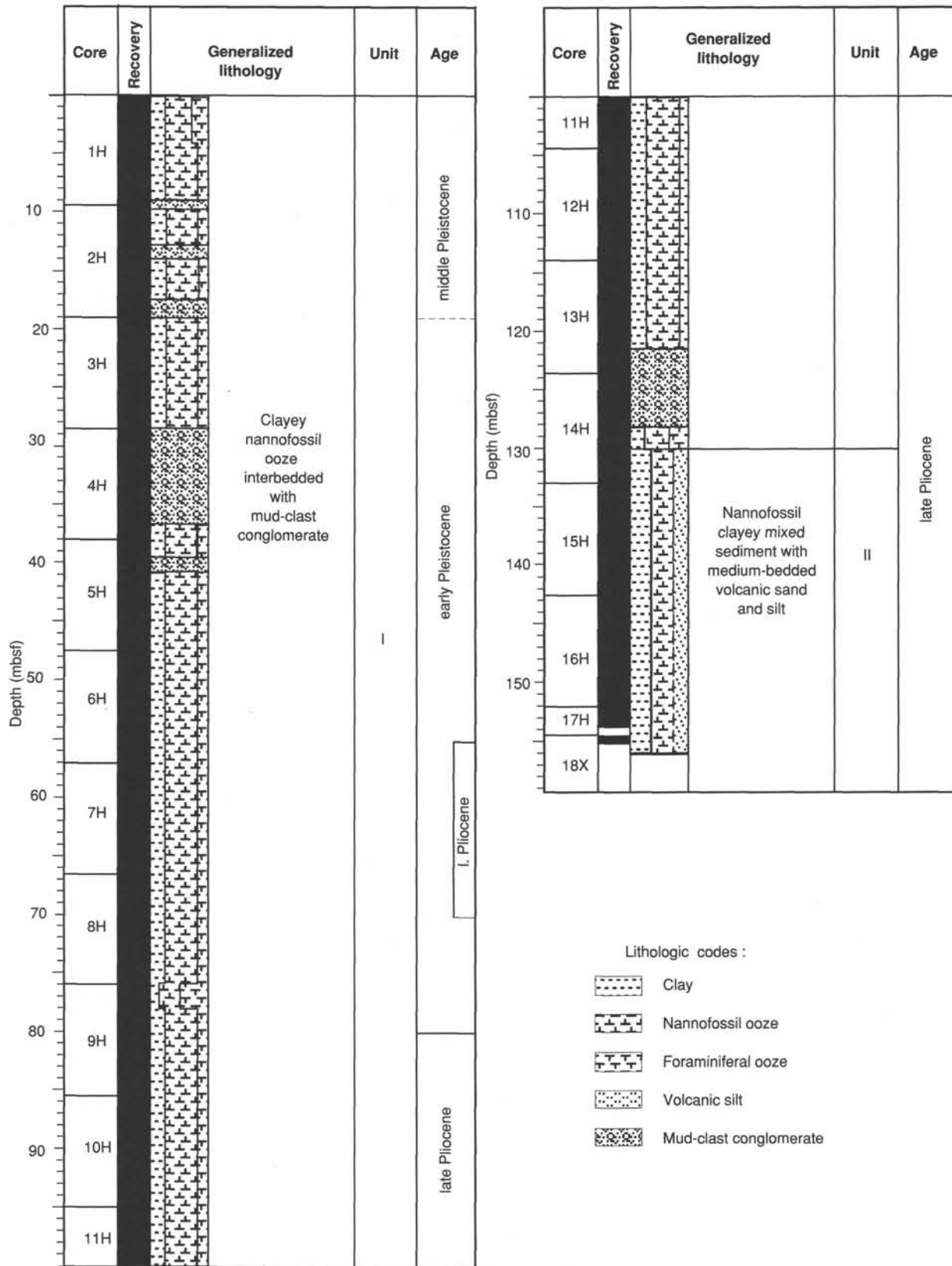


Figure 8. Lithologic summary for Hole 835A, illustrating the main lithologic units and ages as well as a generalized graphic lithology for Site 835.

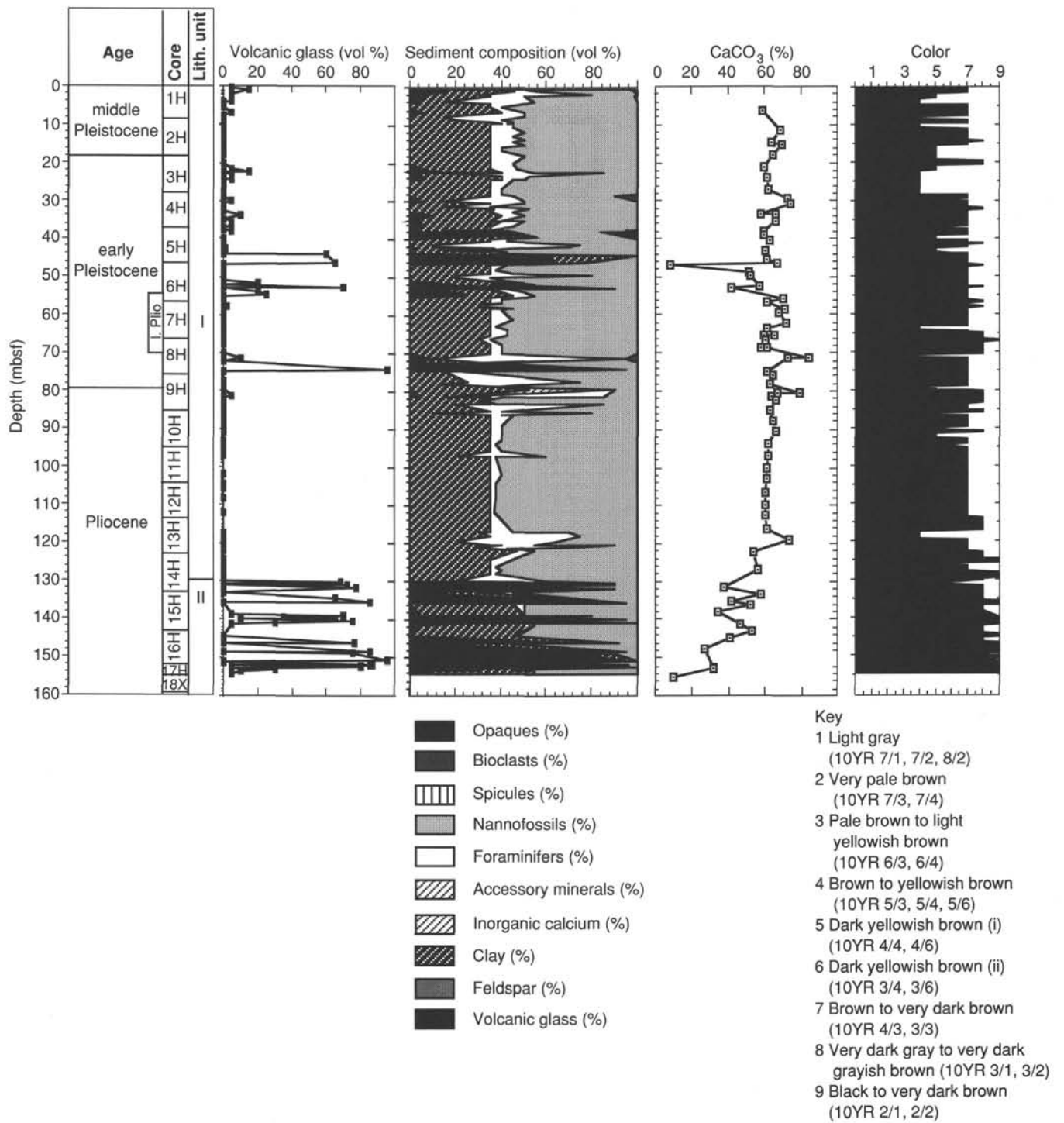


Figure 9. Downcore plots of volcanic glass occurrence (in volume percent); sediment composition (based on analysis of 165 smear slides); CaCO<sub>3</sub> profile; and color variations in the clayey calcareous ooze sediments cored in Hole 835A. Note the sharp increase in the volume percent of volcanic glass at the beginning of Unit II, the increase in clay downcore in Unit II, and the decrease in abundance of foraminifers. Peaks of foraminifer abundance in Unit I mark the presence of calcareous turbidites. Color fields 1–9 represent combinations of colors as defined in the Munsell color chart (1975) and are listed in the key.

## Unit I

Intervals: Sections 135-835A-1H-1 through -14H-4 and Section 135-835B-1R-1  
Depth: 0–130 mbsf

Unit I is 130 m thick and is composed predominantly of brown to very dark brown, iron-oxhydroxide-stained, clayey nannofossil ooze with occasional interbeds of thin vitric volcanic silts, thin foraminifer sands and foraminifer nannofossil oozes, and thick mud-clast conglomerates. Color variations in Unit I (Fig. 9) show some variability, reflecting interbeds of the lighter colored foraminifer sand and foraminifer nannofossil ooze and the presence of darker clasts within the paler mud-clast conglomerate matrix. Vitric volcanic silt layers are present within Unit I, particularly within the intervals 35–55 and 70–75 mbsf, although volcanoclastic material is very rare in the sediment column between 75 and 130 mbsf.

### Clayey Nannofossil Ooze

Clayey nannofossil ooze comprises the thickest depositional sequence in Unit I. Smear slide analysis of the clayey nannofossil ooze indicates it contains about 35% clay-size material, with the rest of the sediment being composed primarily of calcareous nannofossils (55–65 vol%) and a much smaller percentage of planktonic foraminifers (3%–10%) (Fig. 9). The ratio of clay-size particles to calcareous microfossils (foraminifers and nannofossils) remains fairly constant throughout Unit I and is reflected in the  $\text{CaCO}_3$  content, which remains fairly constant at around 60%–65% (Fig. 9). The nannofossil and clay-size particles are stained with amorphous iron oxyhydroxides, giving the sediment a distinctive brown to very dark brown color. In many sections of Unit I, clayey nannofossil ooze occurs as thick homogeneous beds. From Sections 135-835A-11H-1, 17 cm, through -13H-3, 38 cm, for example, there is a 20-m-thick unit without interbeds or internal structure. However, some planar lamination within the clayey nannofossil oozes occurs as upward-fining layers, grading from sand or silt up into silt or clay (e.g., in Sections 135-835A-2H-5, 100–135 cm, and -13H-5, 72–98 cm). Both thinly and thickly laminated layers occur. Some intervals (e.g., in Sections 135-835A-8H-3, 105 cm, through -8H-4, 20 cm, and in Section 135-835A-9H-3, 15–53 cm), are thin to very thinly bedded (1–4 cm thick) and show planar lamination.

Although the clayey nannofossil ooze is frequently homogeneous over long intervals, mottled areas occur throughout the sequence. Pumice fragments (up to 2 cm in diameter) occur as scattered fragments that have been weathered to a rusty brown color. Mottling also occurs as a result of grain-size variations, with small inclusions of silt-size to fine sand-size sediment within the clayey and foraminifer-rich nannofossil oozes. These inclusions are 1–5 mm in diameter and are lighter in color than the adjacent sediment. Mottling caused by chemical processes is widespread and is seen within the clayey nannofossil oozes as slight color changes affecting small areas; such mottling often resembles bioturbation. In Section 135-835A-7H-5, 133–134 cm, a very pale brown halo surrounds an altered pumice fragment within brown clayey nannofossil ooze (Fig. 10). This color variation is secondary in origin and related to *in situ* weathering of the pumice fragment. Burrows and bioturbated structures are quite common in the clayey nannofossil oozes of Unit I.

In Section 135-835A-5H-1, 10 cm, a small  $4 \times 2 \times 2$  cm allochthonous pebble of indurated sediment occurs. This is overlain by volcanic ash that appears to be cemented with manganese oxide. Similar manganese oxides have been described from the Tonga-Kermadec Ridge (Cronan et al., 1982) and the Valu Fa Ridge, central Lau Basin (Herzig et al., 1990) and have been shown to be hydrothermal in origin.

### Mud-clast Conglomerate

Beds of mud-clast conglomerates occur as distinct lithologies in Cores 135-835A-1H, -2H, -4H, -5H, -13H, and -14H. The mud-clast conglomerates generally consist of rounded to angular clasts and blocks of clayey and foraminifer-rich nannofossil ooze enclosed in a matrix of clayey nannofossil ooze. Matrix-supported conglomerates are the most common, although clast-supported conglomerates occur. The mud clasts are usually rounded (e.g., in Section 135-835A-2H-5, 24–34 cm; Fig. 11), but fragmented, subangular to subrounded clasts also occur (e.g., in Section 135-835A-14H-1, 103–124 cm).

Some of the mud-clast conglomerate sequences appear to be very thickly bedded. Individual mud-clast conglomerate sequences may represent several depositional events. Pumice fragments are common, especially in Sections 135-835A-13H-5, 145 cm, through -13H-7, 12 cm, whereas basalt pebbles occur only sporadically. The lower boundaries of the conglomerate beds are often sharp and steeply dipping (up to  $47^\circ$ ) erosional surfaces that cut into clayey nannofossil ooze (Fig. 12).

Three separate mud-clast conglomerate beds can be distinguished in Sections 135-835A-1H-7 through -2H-7 (9.0–19.0 mbsf). These are 1.65, 1.30, and 4.0 m thick, respectively, and consist of matrix-supported, irregular to rounded clasts of dark brown clayey nannofossil ooze and weathered pumice in a lighter yellowish brown groundmass of clayey nannofossil ooze. Individual pumice clasts are as large as 5 cm in diameter, whereas mud clasts are as large as 10 cm in diameter. The clasts appear to show a subvertical alignment in the core. The mud-clast conglomerate deposit in Core 135-835A-4H (28.5–38.0 mbsf) is 5.55 m thick and appears to be a single deposit. It consists of matrix-supported, angular to rounded clasts of dark brown, clayey nannofossil ooze as large as 20 cm in diameter, fragments of weathered pumice as large as 3 cm in diameter, and rare angular vesicular basalt clasts as large as 3 cm in diameter. Smear slide analysis of the clayey nannofossil ooze groundmass shows it consists primarily of calcareous nannofossils (70 vol%), but it also contains minor amounts of volcanic glass (10 vol%), foraminifers (10 vol%), and clay-size material (10 vol%). The mud-clast conglomerate in Sections 135-835A-13H-5 through -14H-4 is 6.8 m thick and also appears to be a single deposit. The upper part of the bed is normally graded with much smaller sized (maximum clast diameter = 3 cm), generally well-sorted clasts grading downward into a much coarser deposit consisting of large (as much as 20 cm in diameter), matrix-supported, angular to rounded, very dark brown to pale brown mud clasts. Rusty-colored, yellowish brown, weathered pumice clasts appear more common in the upper part of the bed (Fig. 13) and, even when found in the lower part of the deposit, are generally much smaller than the associated mud clasts. The clasts show an apparent subvertical orientation in the lower part of the bed and are held in a nannofossil, clayey, mixed sediment groundmass that contains common sinuous mottles, interpreted as water escape structures. The mud-clast conglomerate is directly overlain by a 4-m-thick clayey nannofossil foraminifer ooze that has a graded base. Foraminifers become more abundant toward the base of the unit, and the base of the deposit is a foraminifer sand, containing coarse sand- and gravel-size mud clasts and pumice fragments. The graded base is overlain by laminated foraminifer mud (interpreted as Bouma Division  $T_d$ ), which is in turn overlain by a thick, homogeneous nannofossil foraminifer ooze with clay (interpreted as Bouma Division  $T_e$ ). The thickness of this depositional unit (interpreted as a turbidite) is uncertain because of the difficulty in identifying the top of the bed, but it is at least 3.6 m thick.

The most commonly occurring soft-sediment deformation structures with the mud-clast conglomerates are areas of sinuous

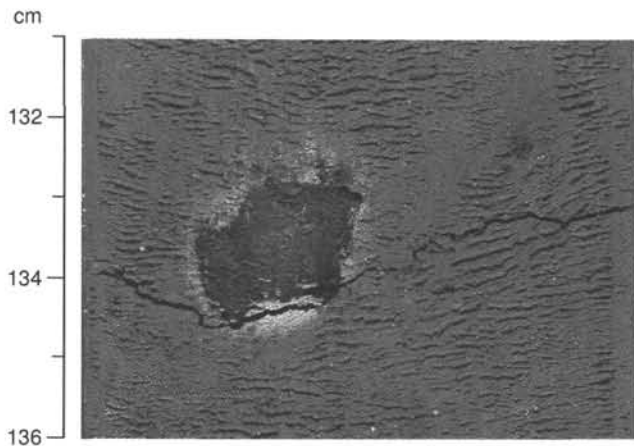


Figure 10. Color halo surrounding weathered pumice fragment (interval 135-835A-7H-5, 131–136 cm).

mottling, interpreted as water escape pillars. These are seen in Sections 135-835A-2H-3, -2H-4, -13H-6, -13H-7, -13H-CC, -14H-1, -14H-2, and -14H-3. The water escape pillars vary in length from a few centimeters to up to 20–30 cm long, and usually show an anastomosing pattern upward through the core (Fig. 14). They are often easily recognizable because of color changes along the walls of the pillars and the grain-size variations. A very pronounced vertical alignment of the clasts in the conglomerate is often associated with the water escape structures. Mud clasts up to several centimeters in length and with their long axis oriented vertically within the core also occur (e.g., in Section 135-835A-13H-6, 1–30 cm; Fig. 13).

The occurrence of water escape structures and the vertical to subvertical alignment of mud clasts in some but not all mud-clast sequences, which are otherwise similar in lithology, suggests that these features are likely to be sedimentary in origin and not an artifact caused by drilling.

#### *Foraminifer Sand Interbeds*

White to light gray interbeds of foraminiferal sands and oozes occur throughout Unit I. Their locations are summarized in Table 2. These characteristically show sharp basal contacts with bases that frequently show normally graded bedding and planar laminations. The tops of the interbeds are typically bioturbated and gradational with the overlying sediment, which is commonly clayey nannofossil ooze. They range from 1–2 cm to 2 m or more in thickness. The thickest units frequently show graded bases of foraminiferal sand, fining upward into foraminiferal ooze, which is often laminated, and then grading into iron-oxyhydroxide-stained clayey nannofossil ooze with foraminifers. These are interpreted as representing single depositional units deposited by carbonate-rich turbidity currents. The upper boundary of these turbidites with the overlying sediment is often indistinct, especially where the overlying sediment is homogeneous clayey nannofossil ooze. The white to gray foraminiferal sand/ooze interbeds are particularly common in Cores 135-835A-8H to -11H (66.5–95 mbsf). Within this interval, two thick calcareous turbidites occur (thickness = 0.3–2 m) together with several much thinner ones (as thick as 10 cm). These have an irregular depositional cyclicity of 0.05–6.8 m. Compositionally, these beds consist of planktonic foraminifers, reworked carbonate rock fragments (intraclasts), rare molluscan shells, redeposited nannofossils, and clay-size material. Benthic foraminifers comprise <1% of the sediment and are generally deep-water varieties. Cross-stratification occurs in Section 135-835A-11H-2, 40–48 cm. This 8-cm-thick, fine-grained to medium-grained, foraminifer ooze

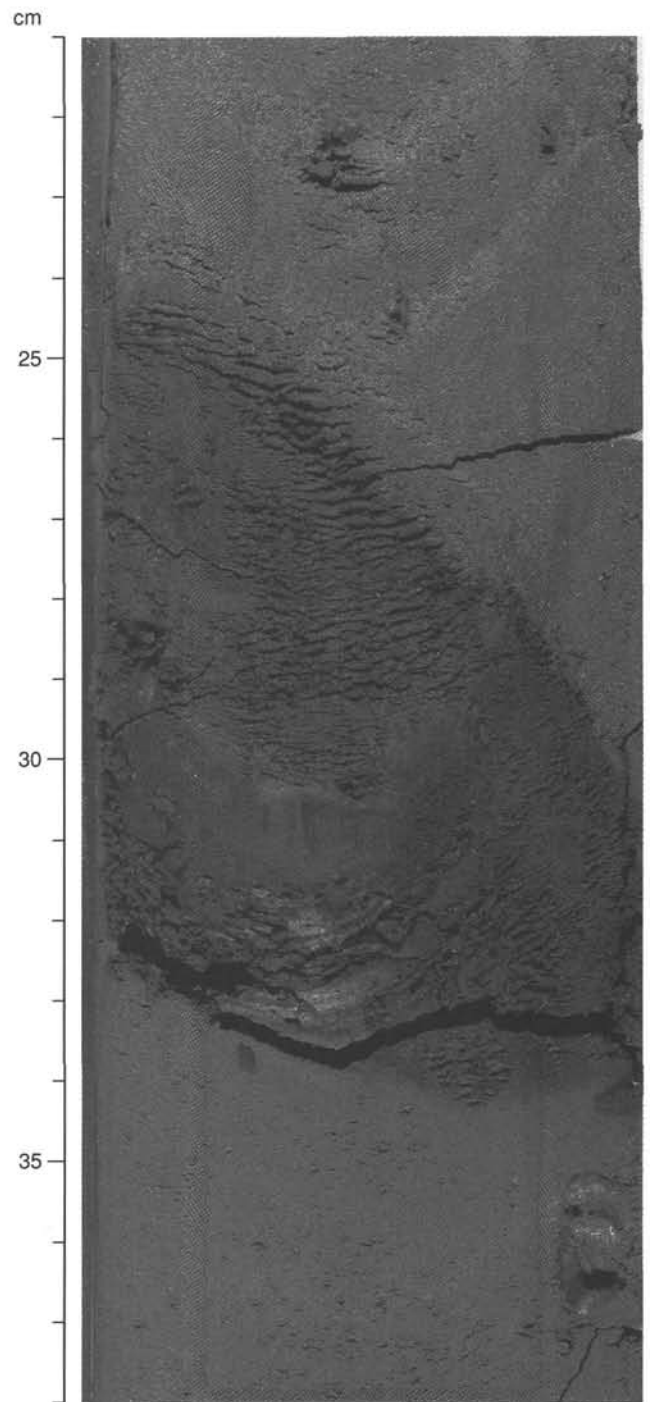


Figure 11. Isolated mud clast in nannofossil ooze in Section 135-835A-2H-5, 21–38 cm. Note the rounded shape of the mud clast. The interval shown is part of a thicker sequence of mud-clast conglomerates.

interval contains inclined foreset beds with an apparent dip of  $5^{\circ}$ – $10^{\circ}$ . The foreset beds are 1–5 cm thick and are occasionally graded. Underlying this cross-stratified interval is a planar-eroded base overlain by a 4-cm-thick, normally graded interval and then a 6-cm-thick, thickly laminated to thinly bedded interval. Above, there is a gradual transition into nannofossil ooze with clay. The turbidite described here represents the most complete Bouma sequence (Bouma, 1962) seen at Site 835. From the base upward there is an eroded base, a massive graded interval ( $T_a$ ), a planar

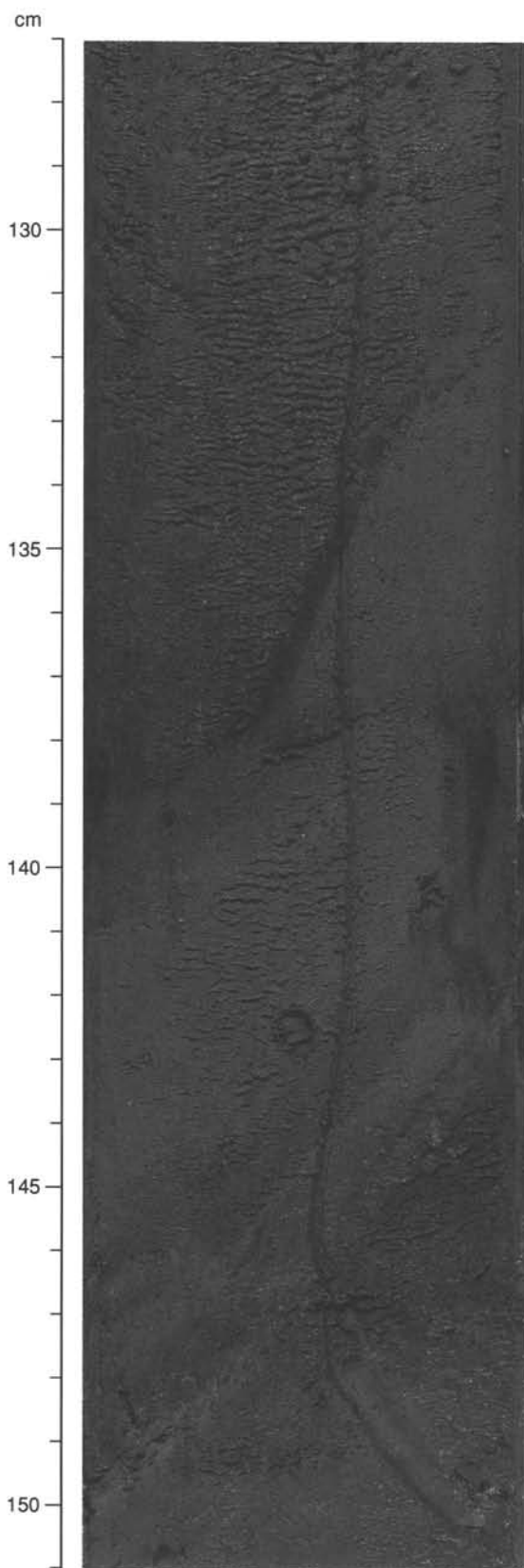


Figure 12. Sharp, steeply dipping erosional scour at Section 135-835A-1H-6, 127–151 cm, separating the nannofossil ooze with foraminifers and clay (below) from the foraminifer nannofossil ooze with clay (above).

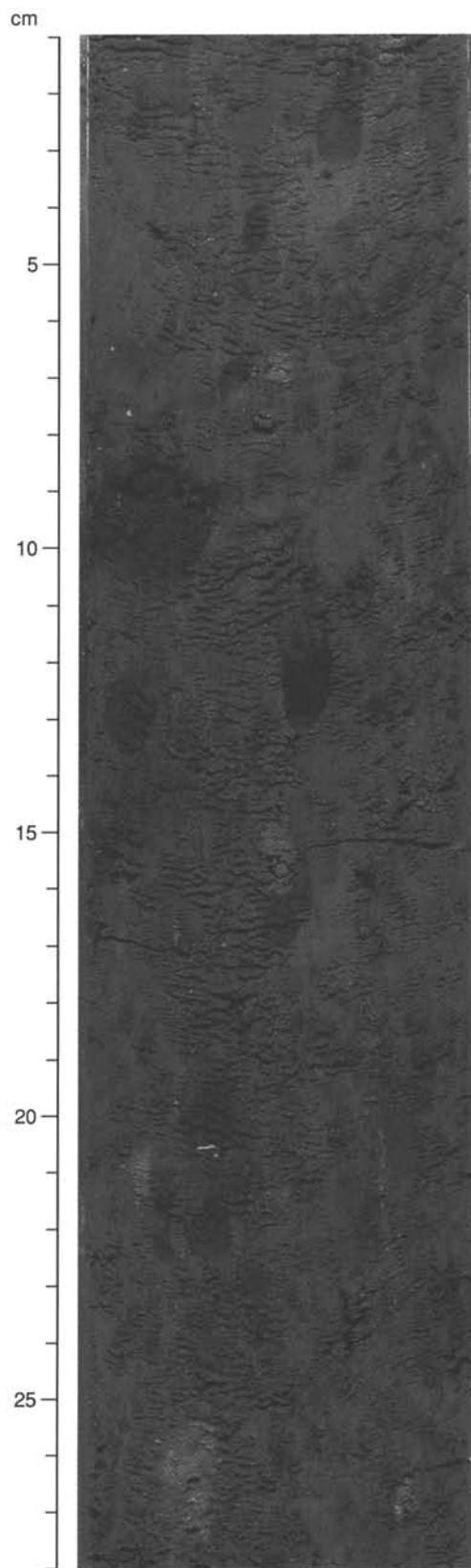


Figure 13. Mud-clast conglomerate with numerous pumice fragments in Section 135-835A-13H-6, 1–28 cm. Note the probable water-escape pillars and the subvertical arrangement of mud clasts caused by water expulsion.

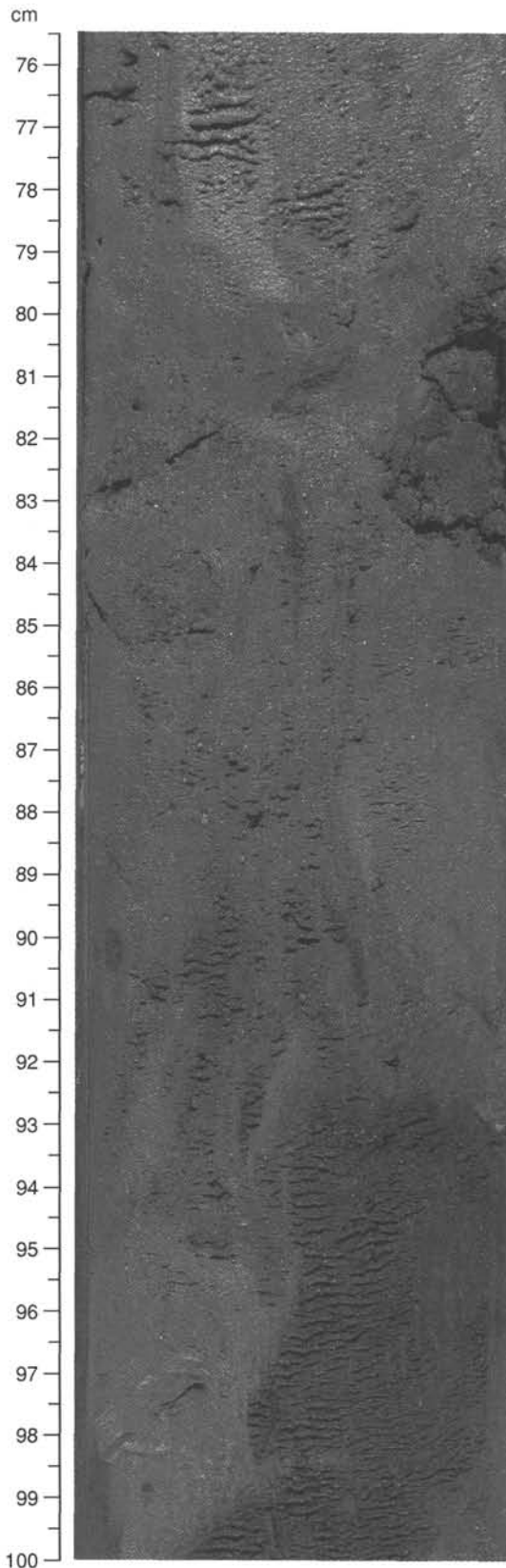


Figure 14. Probable water-escape pillars in mud-clast conglomerate in Section 135-835A-2H-3, 75.5–100 cm. Note that the light-colored, sub-vertical pipes are slightly coarser grained than the surrounding sediments because of the removal of clay-size material. The clay has been redeposited along the margins of the pipes (dark).

Table 2. Location of foraminiferal sand interbeds at Site 835.

Core, section, interval (cm)	Depth* (mbsf)	Thickness of interbed (cm)
135-835A-		
1H-2, 11–12	1.61	1
1H-2, 21–22	1.71	1
1H-2, 105–106	2.55	1
1H-3, 57–68	3.57	11
3H-3, 5–40	22.05	35
4H-6, 128–130	37.28	2
4H-6, 130–135	37.30	5
4H-6, 135–149	37.35	14
4H-7, 0–8	37.50	8
4H-7, 8–22	37.58	14
4H-7, 22–32	37.72	10
5H-1, 120–140	39.20	20
5H-2, 131 to 5H-3, 3	40.81	22
5H-3, 30–50	41.30	20
5H-3, 105–120	42.05	15
5H-4, 89–91	43.39	2
5H-6, 15–23	45.65	8
6H-2, 55–57	49.55	2
7H-3, 103 to 8H-4, 42	61.03	89
9H-2, 46–51	77.96	5
9H-3, 14–53	79.14	39
9H-3, 119–124	80.19	5
9H-4, 78–81	81.28	3
9H-4, 121–123	81.71	2
9H-5, 141 to 9H-6, 2	83.41	11
9H-6, 122–125	84.72	3
9H-7, 47–51	85.47	4
10H-1, 55–62	86.05	4
10H-3, 20–25	88.70	7
10H-4, 90–95	90.90	5
11H-2, 30–52	96.80	22

\*Depth to top of interbed.

laminated interval ( $T_b$ ), a cross-stratified interval ( $T_c$ ), a graded interval of turbiditic mud/clay ( $T_e$ ), and pelagic/hemipelagic ooze.

#### Volcanic Silt

Epiclastic vitric volcanic silts are rare in most of Unit I. However, there are three ash layers at 47.00, 52.71, and 74.26 mbsf, ranging in thickness from 5 to 21 cm (Table 3; see “Volcaniclastic Sediments” discussion, below). However, smear slide analysis suggests that volcanic glass is more widely distributed within the upper part of Unit I, particularly between 30 and 55 mbsf (Fig. 9). Microscopically distinguishable vitric-glass-bearing layers (horizons containing 15% or more volcanic glass) can be identified from smear slides at 0.79, 22.27, 51.72, 53.8, and 54.68 mbsf. These may represent very thin vitric volcanic silt layers whose continuity has been destroyed by bioturbation. The interval 82–130 mbsf appears to be totally devoid of volcaniclastic material.

Based on paleomagnetic and biostratigraphic data (see “Sediment Accumulation Rates” section, this chapter), the age span of Unit I is 0–2.8 Ma, with an average sedimentation rate of 46 mm/k.y.

#### Unit II

Intervals: Sections 135-835A-14H-4 to -18H-1 and Sections 135-835B-2R-1 to -3R-1

Depth: 130.0–155.5 mbsf

Unit II is composed of clayey nannofossil mixed sediment interbedded with epiclastic vitric ash layers and volcanic silts. Compositionally, Unit II is characterized by a marked increase in volcaniclastic material, especially glass (Fig. 9). Unlike Unit I,

Table 3. Characteristics of discrete ash layers and ash turbidites in Hole 835A.

Core, section, depth	Depth to top (mbsf)	Depth to base (mbsf)	Smear slide	Thickness (cm)	Type of unit	Glass (vol%)	Maximum grain size ( $\mu\text{m}$ )	Significant shard morphologies				Igneous minerals present (>1 vol%)
								Tubular	Bubble wall	Angular	Rounded	
135-835A-												
5H-7, 19	47.00	47.21	x	21	E, G		270				x	plag, augite, opaques
6H-3, 72	52.71	52.76	x	5	E, H	70					x	
8H-6, 30	74.26	74.32	x	6	E, G	95	700	x	x	x		plag, opx
14H-5, 105	130.54	130.56	x	2	E, G	68	120		x	x		plag (very rare)
14H-6, 3	130.99	131.06	x	7	E, G	72	90		x	x		plag
14H-6, 85	131.83	131.87	x	4	E, G	77	350	x		x		plag
15H-2, 122	135.66	133.73	x	7	E, G	85	500	x	x	x		plag, augite
15H-5, 2	138.90	139.06	x	16	E, G	70	170	x	x	x		plag, augite, opaques
*15H-5	139.06	139.32		26	E, G							
*15H-5	139.32	139.53		21	E, G							
15H-5, 59	139.53	139.59	x	6	E, G	35						
15H-5, 86	139.59	139.87	x	28	E, G	65	400	x	x	x		plag, augite, opaques
15H-6, 88	141.16	141.39	x	23	P, H	95	1300	x			x	plag, augite, opx, (ox) hbl, opaques
16H-3, 67	145.84	146.21	x	37	E, G	76	200	x	x	x		plag
16H-4, 150	148.43	148.56	x	13	E, G	85	200	x	x	x		plag
16H-5, 38	148.81	148.92	x	11	E, G	75	1200	x	x	x		plag, augite
16H-7, 36	151.61	151.91	x	30	E, G	85	200	x				plag, augite
17H-1, 30	152.28	152.30	x	2	E, H	80	400	x	x	x		plag, augite
*17H-1	152.39	152.56		17	E, G							
*17H-1	152.93	153.11		18	E, H							
*18H-1	155.02	155.10		8	E							

Notes: Core, section, depth to smear slide sample (cm); asterisk (\*) indicates ash layer from which no smear slide was made, and only the core and section in which the ash layer occurs are indicated. Type: P = pyroclastic, E = epiclastic, H = homogeneous, and G = graded. Glass (vol%): Glass content normally indicates maximum mode estimated from smear slides; however, glass content may be highly variable, especially in the graded sequences. Dominant morphologies: tubular = pumiceous shards with tubular vesicles, bubble wall = bubble-wall shards, angular = angular shards. Igneous minerals present: Igneous mineral content is noted when more than trace amounts (>1%) are present. Key: plag = plagioclase, cpx = clinopyroxenes, opx = orthopyroxenes, hbl = hornblende, and ox = oxidized.

Unit II shows a gradual increase in clay content downcore, whereas the content of foraminifers decreases downcore, becoming rare below 130 mbsf (Fig. 9). The clayey nannofossil oozes/mixed sediments of Unit II are darker than those of Unit I, showing very dark gray to very dark grayish brown and very dark brown to black colors (Fig. 9), similar to those of Unit II at Site 834 (see "Site 834" chapter, this volume).

#### Clayey Nannofossil Ooze

Clayey nannofossil ooze is the predominant sediment type in the upper part of Unit II, although its clay content steadily increases downcore, so that by 140 mbsf the sediment becomes a "mixed sediment" in the classification of Mazzullo et al. (1987). This is reflected in the decreasing  $\text{CaCO}_3$  content of the clayey nannofossil ooze/mixed sediment, which constitutes around 50% of the sediment in the upper part of Unit II but decreases to around 30% toward the base of the Unit (Fig. 9). The clayey nannofossil oozes show slight to moderate mottling throughout Unit II, similar to that seen in Unit I, and sometimes contain isolated pumice and mud clasts. The clayey nannofossil oozes of Unit II are more intensely stained by iron oxyhydroxides than Unit I, often reaching a very dark brown color.

#### Manganese Oxide Fragments

Toward the base of Unit II (Sections 135-835A-17H-1, 93–150 cm, and -17H-CC, 0–32 cm), small fragments of black manganese oxide crust are sparsely distributed within the clayey nannofossil ooze. The fragments range in size from sub-millimeter to 1.5 cm across; are generally subrounded to angular, massive, brittle; and have a purplish black metallic to submetallic lustre. X-ray diffrac-

tion shows basal  $d$ -spacings at 9.6 and 4.8 Å, with prismatic reflections at 2.4 and 1.4 Å, characteristic of todorokite (10 Å manganese). Both the morphology and mineralogy indicate a hydrothermal origin for the manganese oxide fragments. Similar manganese oxides, in the form of platy crusts, have been reported from surficial settings in the central Lau Basin (Herzig et al., 1990) and the Tonga-Kermadec Ridge (Cronan et al., 1982), and have been shown to be hydrothermal in origin based on metal accumulation rates.

#### Volcanic Silt

Volcaniclastic material comprising epiclastic turbidites make up 12% of the total bulk of Unit II. Individual ash layers range from 1 to 37 cm in thickness. Many of the epiclastic ash units show graded silty bases overlain by silty planar- and cross-laminated Bouma Tc and Td units. Most of the epiclastic vitric volcanic silts are composed of colorless, apparently unaltered volcanic glass, although some contain small amounts of anhedral-subhedral feldspar and pyroxene grains (see "Volcaniclastic Sediments" below).

#### Nannofossil Chalk and Siltstone

At the base of the sedimentary sequence cored at Hole 835A (Section 135-835A-18H-1), 60 cm of very dark brown clayey nannofossil chalk was recovered. This overlies 10 cm of indurated planar-laminated volcanic siltstone containing burrows of very dark brown clayey nannofossil chalk. In Section 135-835B-3R-1, 1.2 m of laminated vitric to crystal-rich siltstones containing well-rounded mud clasts were cored. Dark laminae are mainly made up of pyroxene crystals, whereas the lighter laminae are

composed of varying proportions of plagioclase and pale brown glass shards. These laminae are interbedded with vitric siltstone containing millimeter- to centimeter-size mud clasts. These sediments are the deepest recovered at Site 835 (154.3–155.5 mbsf), and they directly overlie basaltic basement.

Paleomagnetic and biostratigraphic data (see "Sediment Accumulation Rates" section, this chapter) have been used to determine the age span of Unit II as 2.8–3.4 Ma, with an average sedimentation rate of 43 mm/k.y.

#### Volcaniclastic Sediments

We recovered 21 sediment layers rich in volcanic silt at Site 835. These mainly occur in Unit II. All but one occurrence in the lower part of Unit II (141.39 mbsf) show the influence of major reworking or redeposition, mainly by turbidity currents. Isolated, lapilli-size pumice clasts occur throughout the core.

We examined 16 ash samples from Hole 835A in smear slides. Refractive indices of optically clear, isotropic glass shards were determined in seven samples to evaluate their SiO<sub>2</sub> concentrations, using the method detailed in the "Lithostratigraphy" section of the Site 834 chapter (this volume).

#### Primary Volcaniclastics

A single, greenish gray layer of coarse vitric ash with sharp upper and lower boundaries occurs in the lower part of Unit II at 141.39 mbsf (Section 135-835A-15-6H, 66 cm), corresponding to an age of about 3.1 Ma (Fig. 15 and Table 3). This layer is 23 cm thick and very homogeneous, showing only faint internal bedding. The sediment has maximum grain sizes of about 1.3 mm, is extremely well sorted, almost completely devoid of clay- and silt-size components, and contains little biogenic material. The shard population comprises four major types:

1. Colorless, angular to subangular pumice clasts with characteristic tubular vesicles. These dominate the deposit. They often show low first-order birefringence, most likely caused by hydration.
2. Extremely delicate and fibrous shards that form a significant minor component, unique to this layer. They are rather sparsely vesiculated, very elongated, and needlelike with extreme aspect ratios of up to 25. It is highly unlikely that these would have survived any major redeposition event.
3. Angular to subangular colorless and clear platy bubble-wall and bubble-junction shards, some containing internal, slightly oval vesicles. These are quite abundant in the smaller grain-size fractions.
4. Rare, brown, mainly subangular shards with abundant round to slightly oval vesicles.

The mineral assemblage of this vitric ash layer comprises plagioclase, augite, hypersthene, (oxidized) hornblende, and opaques. The colorless shards are of dacitic composition (69 wt% SiO<sub>2</sub>; Fig. 16), based on their refractive indices ( $n = 1.515$ ). This, however, has to be considered with special care as hydration could lower the refractive index, although the refractive indices of these shards are fairly constant. Brown vitric shards have an andesitic composition ( $n = 1.542$ ; 61 wt% SiO<sub>2</sub>).

We interpret this layer as a primary tephra mainly because of (1) homogeneous bedding and composition, (2) sharp upper and lower boundaries, (3) the occurrence of very delicate shards that would not have survived any major redeposition event, and (4) a lack of biogenic input. The occurrence of brown andesitic shards may indicate either a range of chemistry during eruption, or the erosion and incorporation into this tephra layer of glass, andesitic in composition, from an "older" deposit. The thick nature of the

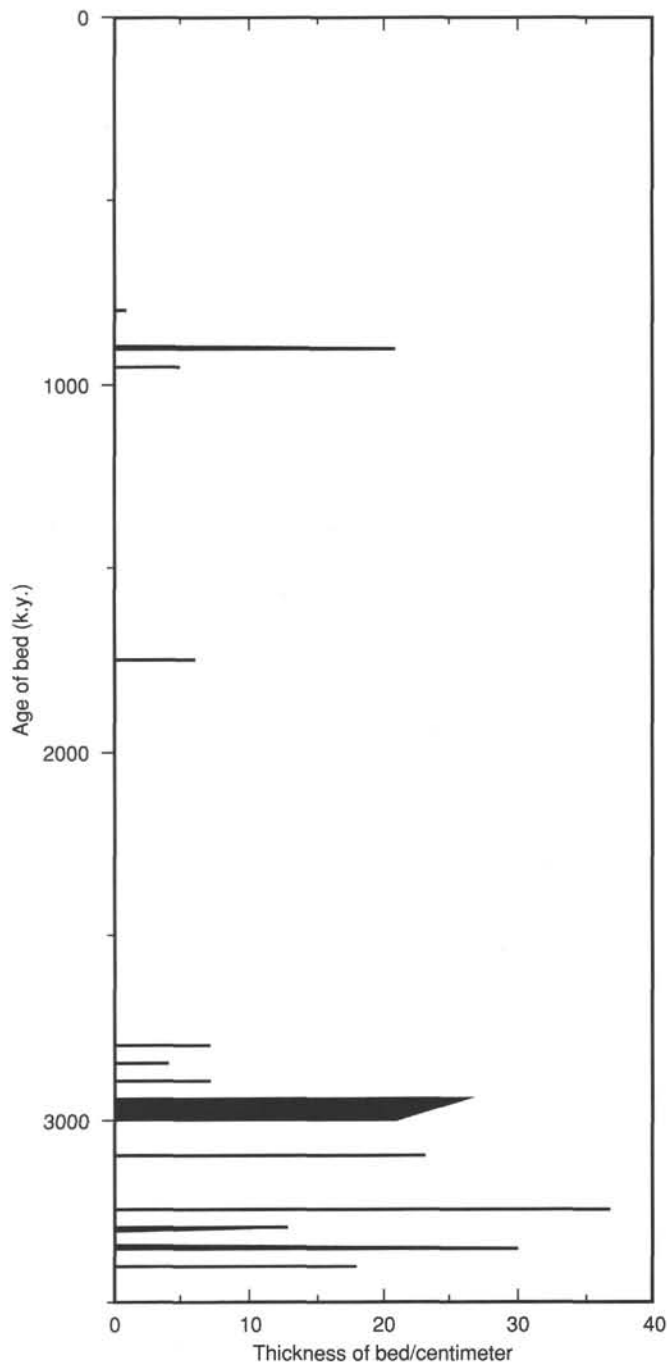


Figure 15. Variations in thickness of volcaniclastic turbidites, which show volcanic-enriched bases (VEBs), with time in Hole 835A.

bed and its relatively coarse grain size suggests a medial to proximal distance to the eruptive center. A compilation by Ninkovich et al. (1978) shows that ash particles >1 mm are hardly ever found at distances >100–200 km from the source, with the possible exception of unusually powerful eruptions (e.g., Toba, Sumatra). These distances have to be regarded as maximum values that depend on the wind direction during eruption. This means, however, that both the Lau Ridge and the Tofua Arc are potential locations for the source of tephra for Site 835 since, at the time of eruption, the Lau Basin was likely to have been considerably narrower than it is at present.

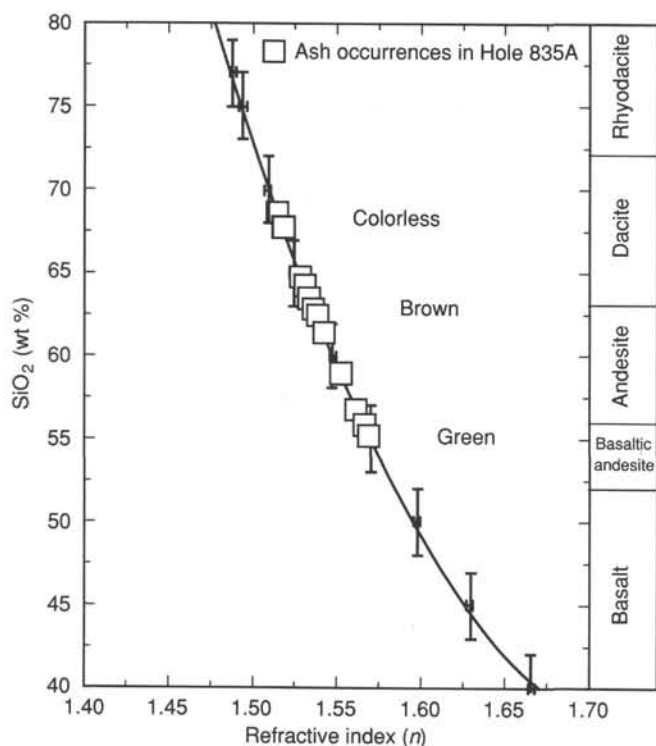


Figure 16. Correlation of refractive indices ( $n$ ) and  $\text{SiO}_2$  concentrations of volcanic glass after Church and Johnson (1980) and Schmincke (1981). The predominant colors of the glass shards, correlated with their probable chemical composition, are indicated.

The scarcity of primary tephra layers at Site 835 probably does not reflect the original input of fallout ashes into this area and cannot be interpreted as indicating a lack of major explosive eruptions in the region during the past 3.4 m.y. It is more likely that heavy reworking, abundant slumping, and mass flows in the whole of Unit I and turbidites in Unit II destroyed most of the original record of fallout deposits.

#### Pumice Lapilli

Lapilli-size pumice clasts, which occur throughout the core, normally have diameters  $<1$  cm, but may reach maximum diameters of about 7 cm. Most are heavily altered to soft, dark reddish brown, orange, and yellowish brown clay and hydrated iron oxide.

It is likely that the majority of pumice lapilli in Site 835 originated from proximal eruptions on the Lau Ridge and Tofua Arc, although additional inputs from more distant sources may have occurred.

#### Reworked Volcaniclastics (Epilastic Deposits)

##### General Characteristics

Reworked volcaniclastics, ranging in thickness from 2 to 37 cm (Table 3), occur in variable amounts within the turbidite deposits. In addition, minor amounts of volcanic glass occur within nanofossil ooze and foraminifer-rich calc-turbidites throughout Units I and II. This glass probably represents thin pyroclastic layers that have been extensively mixed into the nanofossil ooze by bioturbation. Apart from two thin, isolated occurrences (Sections 135-835A-5H-1, 10 cm, and -8H-6, 30 cm) in Unit I, epilastic volcanic sediments are restricted to Unit II. These turbidites form a significant proportion of Unit II (below 130 mbsf; Table 3), but are still exceeded in volume by nanno-

fossil ooze. Unlike Unit III of Hole 834A, no part of the sequence is dominated by volcanoclastic material. The sediments consist mainly of well-sorted beds that normally show a distinct grain-size grading within the silt-size range and a strong compositional grading. As at Site 834, zones of high concentrations of volcanoclastic material (80–100 vol%) are restricted to the bases of the beds (volcanic-enriched base, or VEB). The VEBs usually show distinct light yellow and gray colors and normally make up 15%–25% of the total thickness of individual beds. The upper boundary of the VEBs is gradational, unlike the sharply eroded lower contact, although it is generally quite pronounced where the sediment grades rapidly into brown and dark brown nanofossil ooze with clay. There are much smaller amounts of volcanoclastic material in the central and upper parts of individual turbidite cycles, and mottling, related to burrowing, often occurs there. This internal structure of the turbidites often results in a sharp, partly eroded contact with the beds below, which is characterized by strong contrasts in color, grain size, and composition. Internally, the epiclastic ash layers are usually structureless, although some parallel lamination occurs, especially close to bases.

##### Specific Characteristics and Composition

VEBs throughout Unit II show remarkably few petrological variations, being largely composed of silt-size, colorless to pale brown/green vitric shards (up to 95 vol% in individual layers), though the former are slightly less abundant than at Site 834. Shards are mainly angular, platy, bubble-wall, subangular, pumiceous, and elongate fibrous clasts that occur in varying proportions in the VEBs. The latter two types generally represent the largest clasts within individual VEBs. Minerals of igneous origin are usually present only in small amounts. Plagioclase laths, often showing multiple twinning, are the most common mineral. Green clinopyroxene (augite), opaque oxides, and pale brown hypersthene only occur in trace amounts (hypersthene in two occurrences at Sections 135-835A-8H-6, 30 cm, and -15H-6, 88 cm).

Refractive indices of volcanic glasses in the VEBs range from 1.569 to 1.515 (Table 4 and Figs. 16–17), corresponding to green/brown basaltic andesite to andesite and colorless andesite to dacite.  $\text{SiO}_2$  concentrations range from 55 to 69 wt%. Morphologically, the two compositional groups are rather similar, although fibrous pumice with tubular vesicles is restricted to the andesite and dacite compositions. Overall, glasses with andesitic composition are relatively more abundant than at Site 834. Mixtures of shards with different compositions also occur more fre-

Table 4. Refractive indices ( $n$ ) and  $\text{SiO}_2$  concentrations (estimated after Church and Johnson [1980] and Schmincke [1981]) of vitric glass shards (63–36  $\mu\text{m}$  size fraction) from turbidites in Hole 835A.

Core, section, interval (cm)	Depth (mbsf)	Comments	$n$	$\text{SiO}_2$ (wt%)
135-835A-				
835A-3H-3, 4	22.04	Fibrous	1.518	67.7
835A-3H-3, 4	22.04	Green	1.552	59.0
835A-3H-3, 24	22.24	Clear (lower limit)	1.518	67.7
835A-3H-3, 24	22.24	Brown (upper limit)	1.562	56.8
835A-5H-7, 5	47.05	Clear	1.538	62.4
835A-5H-7, 5	47.05	Green	1.566	55.9
835A-14H-5, 150	131.00	Clear	1.531	64.2
835A-14H-5, 150	131.00	Fibrous	1.529	64.8
835A-14H-6, 82	131.82	Clear	1.536	62.9
835A-15H-5, 80	139.45	Clear	1.534	63.5
835A-15H-5, 80	139.45	Green	1.569	55.2
835A-15H-6, 79	141.04	Clear fibrous	1.515	68.6
835A-15H-6, 79	141.04	Brown	1.542	66.6

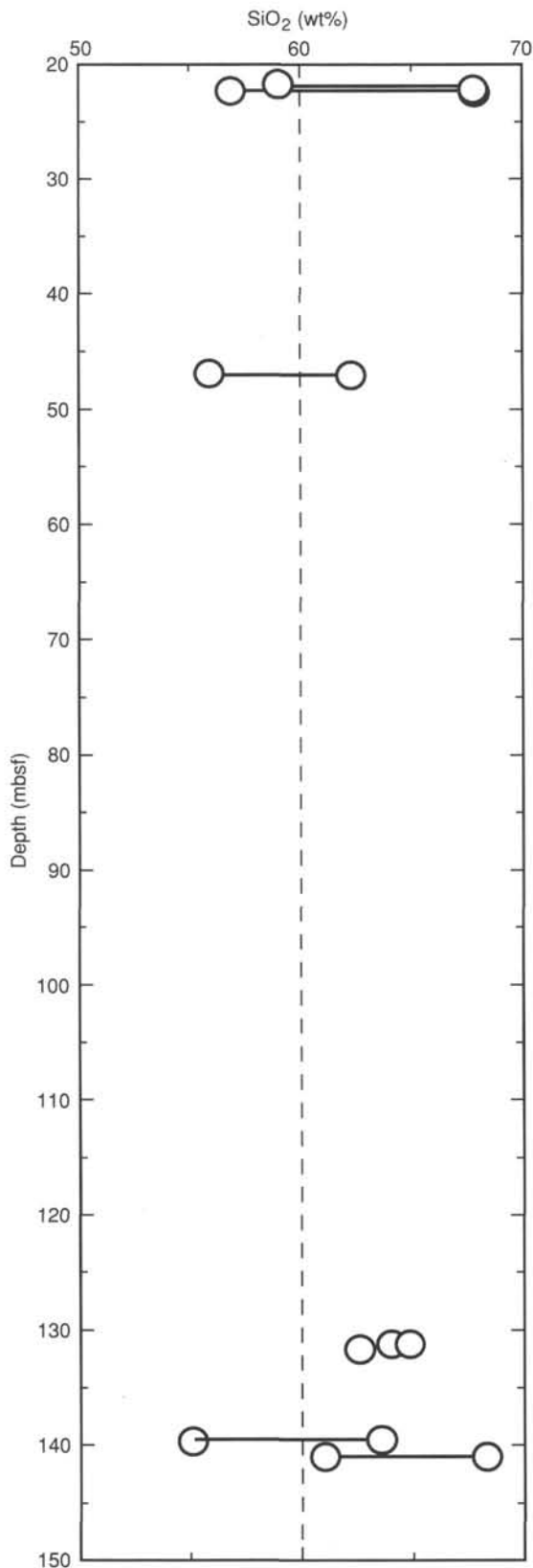


Figure 17. Variations of  $\text{SiO}_2$  in optically clear volcanic glass shards with depth, Hole 835A. The occurrence of two distinct populations of shards in individual samples is indicated by the connecting lines.

quently than in Site 834. The relatively short time interval in which most of the ashes were deposited between 2.8 and 3.4 Ma does not allow interpretations in terms of temporal changes of magma compositions.

#### *Origin and Source of Ash Turbidites in Lithologic Unit II*

Site 835 is located in the center of a narrow, north-trending basin about 150 km from the axis of the Lau Ridge. A number of basement ridges situated to the west define the basin and protect the site from any directly east-flowing sediment supply from the Lau Ridge. Thus, flow is inferred to have been predominantly along the axis of the basin. The greater distance from the arc compared to Site 834 may account for the relative decrease in the amount, thickness, and duration of epiclastic sedimentation. The more intermediate nature of glass compositions in Site 835 compared to Site 834, partly within the same time span, may indicate a different source area for Site 835 turbidites, and that spatial variations existed in the composition of Lau Basin area volcanism in the middle Pliocene.

#### *Alteration of Glass Shards*

Throughout the core, almost all glass shards appear optically clear (isotropic) with the possible exception of the prominent fallout layer at 141.39 mbsf (Section 135-835A-15-6H, 66 cm). The similar optical properties in most individual samples indicate that hydration, generally the first alteration process of silicic glasses and well-known to modify their refractive index (e.g., Ross and Smith, 1955), is generally only at a very early stage.

The abundance of clay-size material within some sediment sections could have locally prevented open-system conditions for vertical seawater exchange, although pore-water chemistry and physical properties data (see "Inorganic Geochemistry" and "Physical Properties" sections, this chapter) suggest such conditions prevail. The fresh nature of volcanoclastics found in the turbidite sequences suggests submarine redeposition fairly soon after eruption.

#### **Depositional History**

Sedimentation at Site 835 was initiated at about 3.4 Ma (upper Pliocene) with the deposition of a sequence of clayey nannofossil oozes and epiclastic volcanoclastic turbidites (Unit II), deposited directly over basaltic lavas. There is no sedimentary evidence to suggest that paleowater depths throughout the Pliocene-Pleistocene were substantially different from those found today. Sedimentation during the latest Pliocene was marked by the periodic emplacement of epiclastic volcanoclastic turbidites. The bimodal compositions of volcanic glasses from the turbidite bases indicate a source area primarily containing shards of silicic andesitic composition, but with a persistent minor basaltic andesite component. This is consistent with derivation from either the Tofua Arc or Lau Ridge, although local intrabasin sources (e.g., Zephyr Shoal) cannot be ruled out. At 3.1 Ma, during the period of volcanoclastic turbidite deposition, a coarse air-fall tephra was deposited. This tephra, mainly of dacitic composition, was deposited from an eruption within  $200 \pm 100$  km of the site, again consistent with derivation from either the Tofua Arc or the Lau Ridge. Volcanoclastic sedimentation never reached the proportions or thicknesses observed at Site 834. Nevertheless, it continued to contribute to the basin between 3.4 and about 2.8 Ma.

After 2.8 Ma, the supply of volcanic turbidites was sharply reduced, with none being deposited after 0.8 Ma. The presence of individual glass grains within nannofossil sediments younger than 2.8 Ma (Unit I) shows that the adjacent arcs continued to contribute minor amounts of volcanoclastic debris to the sub-basin. By that time, arc volcanism was located too far to the east for debris to reach Site 835. For its part, the Lau Ridge, after falling inactive

at about 2.5 Ma, had decreased in importance as a source of epiclastic sediments. Instead, the most prominent volcanic contributions appear to have been in the form of weathered pumice pebbles, which are found throughout the sedimentary section.

The late Pliocene and particularly the Pleistocene were marked by episodes of catastrophic reworking and slumping. Evidence for this is seen in two forms. First, thick mud-clast conglomerates occur that were probably deposited by slumping and muddy debris flows. Second, a coherent section of Pliocene clayey nannofossil ooze has been identified on micropaleontological grounds within the early Pleistocene sequence and is interpreted as a coherent sediment raft. The erosion of thick sedimentary sequences from the margins of the sub-basin probably occurred, as the slump sheets and mud clasts have yielded ages as old as the early late Pliocene, in contrast to the early Pleistocene-aged matrix surrounding them. During periods of clayey nannofossil ooze accumulation, as seen in the upper sections of Unit I, redeposition occurred on a smaller scale in the form of calcareous turbidites. These are dominated by foraminiferal oozes likely to be derived from the carbonate platform fringing the volcanically inactive Lau Ridge. In addition, proximity to active spreading centers and their associated hydrothermal systems is shown throughout the history of the basin by the dark brown staining of the clayey nannofossil oozes by iron-oxyhydroxide minerals, as seen previously at Site 834. Furthermore, the occurrence of fragments of manganese crust of hydrothermal origin in the sediment section immediately overlying basement suggests the likely existence of an active hydrothermal system during the early stages of sediment deposition.

## STRUCTURAL GEOLOGY

### Sediments

The sedimentary section of Hole 835A has suffered considerably more tectonic disturbance than that at Hole 834A. Sedimentation rates also appear to have been significantly higher (see "Sediment Accumulation Rates" section, this chapter). No fault structures are preserved in Hole 835A core; however, evidence for slumping and large-scale reworking of material, in addition to substantial turbidite influx, is widespread at certain horizons. The sedimentological aspects of these features are addressed in the "Lithostratigraphy" section (this chapter). The present section briefly examines the structural information from the core, and the constraints that this information can place upon models for the origin of the tectonic activity.

Two lithologic units were recognized by the sedimentologists (see "Lithostratigraphy" section, this chapter). Unit I (0–130 mbsf; 0–2.5 Ma) is composed predominantly of brown nannofossil ooze, with interbedded foraminiferal sand or volcanic silt turbidite horizons. In addition, mud-clast conglomerate horizons are present at depths of approximately 9–19, 29–41, and 121–128 mbsf. Biostratigraphic and paleomagnetic data suggest that a coherent 15-m-thick raft of clay/nannofossil ooze of lower Pliocene age has been introduced into the otherwise early middle Pleistocene sediments at 55–70 mbsf. Unit II (130–155.5 mbsf; 2.5–3.0 Ma) is composed of nannofossil ooze interbedded with epiclastic vitric ash layers and volcanic silts.

Sedimentary bedding orientations were taken from the core, using temporary coordinates measured relative to the core liner, as described in the "Structural Geology" section of the "Explanatory Notes" chapter. Reorientation of the bedding to geographic coordinates (true north) was made using data from the multishot orientation tool, and verified with reference to magnetic declination data. Bedding of the calc-turbidite horizons typically dips at up to 10° toward the north (Figs. 18–19); much higher dips, however, of up to 65°, are recognized at intervals within Unit I.

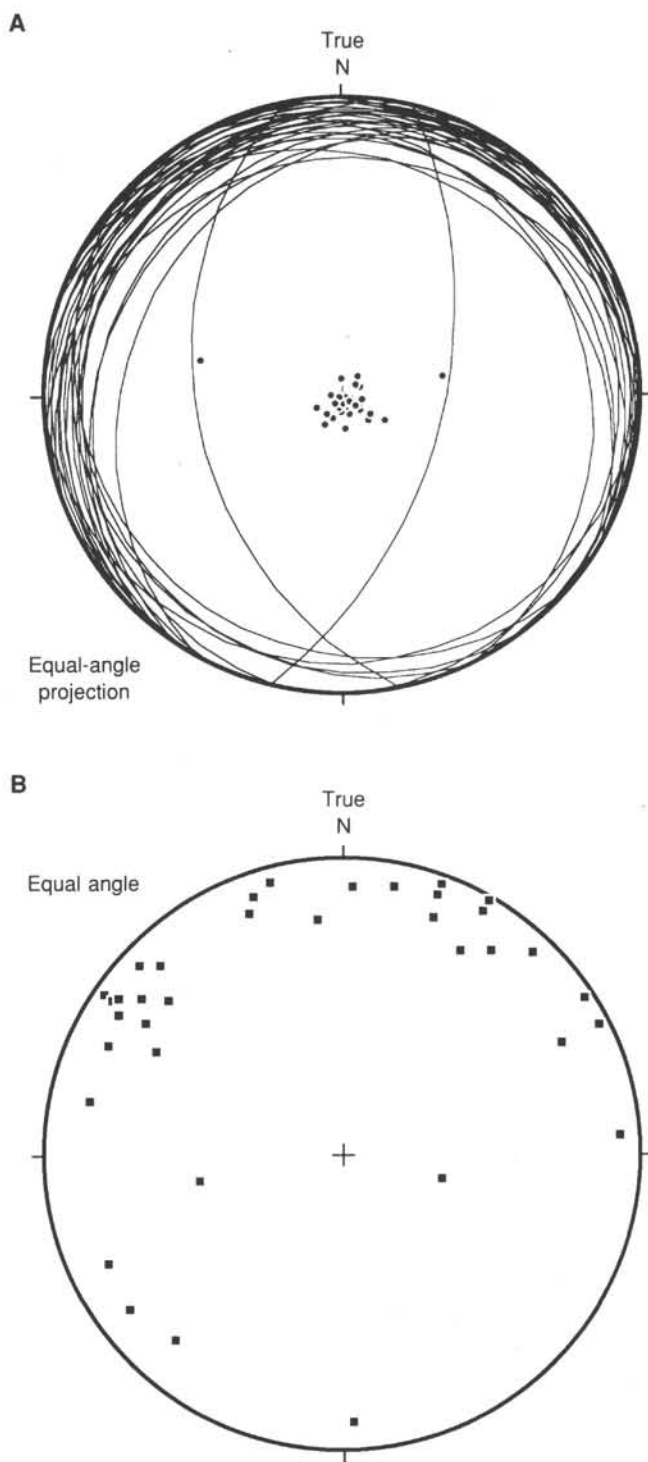


Figure 18. A. Lower hemisphere equal-angle stereographic projection of bedding planes and poles to bedding, Hole 835A. B. Dip direction of bedding. Note the general dip of bedding in the northerly quadrant. Filled squares = dip direction of sedimentary bedding.  $N = 37$ .

These dips correspond to the bases of the mud-clast conglomerate horizons, whose erosive bases appear to have cut at high angles into the nannofossil oozes beneath. A steeply dipping contact, of 38° toward the west, within the Pliocene nannofossil oozes at 69.4 mbsf (Fig. 19) appears to be coincident with the base of the

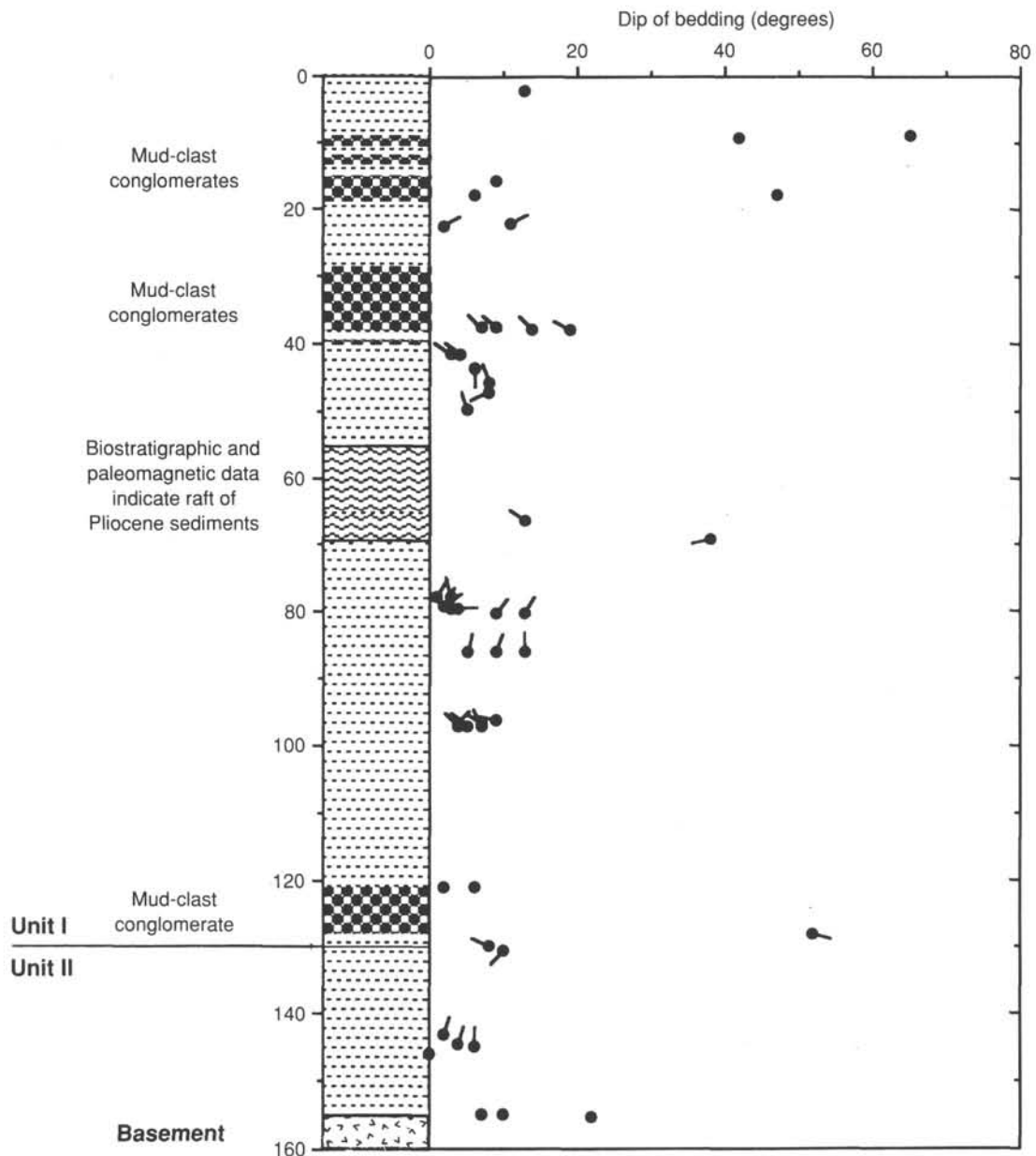


Figure 19. Dip magnitude and dip direction of sedimentary bedding from Hole 835A, with a summary lithologic log included for comparison. Steep dips coincide with the bases of redeposited sedimentary units; most other data are taken from foraminiferal or vitric ash turbidite horizons.

raft. This contact appears to be the only expression of this allochthonous horizon visible within the core, as the lithologies are identical. The westerly dip of the erosive contact may suggest that the raft had slid into the basin from the east; however, with the complex geometries commonly generated by submarine slump deposits, this interpretation should be treated with some caution. It is supported by seismic reflection data described in the “Background and Objectives” section that indicate a westerly tapering, apparently easterly derived seismic unit that we interpret as the slump (Fig. 6).

The dips recorded from the core show no systematic change with depth (Fig. 19). This observation is supported by interpretation of dipmeter plots derived from downhole FMS data (dis-

cussed and compared with the present core-derived data in the “Downhole Measurements” section, this chapter). There is no evidence, therefore, for significant tilting of the sequence during deposition, and thus for activity on the faults bounding the small basin within which Hole 835 is sited. If the  $\sim 5^\circ$  average dip toward the north or northwest displayed by the sediments had a tectonic origin, then block tilting has to have been recent. Instead, it is more likely that the dips recorded are essentially depositional, reflecting a predominant transport direction toward the northwest, north or northeast. The 4-km-wide basin within which the hole is situated is elongated north-south (see “Background and Objectives” section, this chapter), and is a minor bathymetric feature when compared with the more general deepening of the Lau Basin

toward the north. It is suggested that the repeated influx of turbidites and reworking of sediment within this small basin reflects regional rather than local tectonic activity.

### Igneous Basement

Hole 835B encountered basaltic igneous rocks that are presumed to be basement at 156.7 mbsf, and penetrated a further 26.5 m before the hole was abandoned. Only 6.73 m of igneous rock was recovered, and within this sample only seven planar fractures survived the drilling and recovery process. No evidence for displacement was observed on any of the features and, therefore, as for Hole 834B (see "Structural Geology" section, Site 834), we concluded that they represent joints. Two of the joint surfaces are partially coated with a yellow clay mineral, whereas the remaining five show minor iron-oxyhydroxide staining, locally as halos of iron oxidation up to 5 cm wide.

Six of the fractures were corrected back to geographic coordinates by referring their paleomagnetic declinations after 15-mT demagnetization back to magnetic north (or south, if of reversed polarity; see "Structural Geology" section, "Site 834" chapter, this volume). The reoriented data are shown in Figure 20. Few inferences, if any, can be drawn from such a small number of data, given the errors and uncertainties involved in the reorientation process (see "Structural Geology" section, "Explanatory Notes" chapter, this volume).

## BIOSTRATIGRAPHY

### Introduction

The sedimentary sequence at Site 835 is divided into two stratigraphic units (see "Lithostratigraphy" section, this chapter). Unit I extends from Core 135-835A-1H to the middle part of Core 135-835A-14H and is composed mainly of nannofossil ooze. Unit II, extending from the middle part of Core 135-835A-14H to Core 135-835A-17H, is characterized by volcanic sands and silts (Fig.

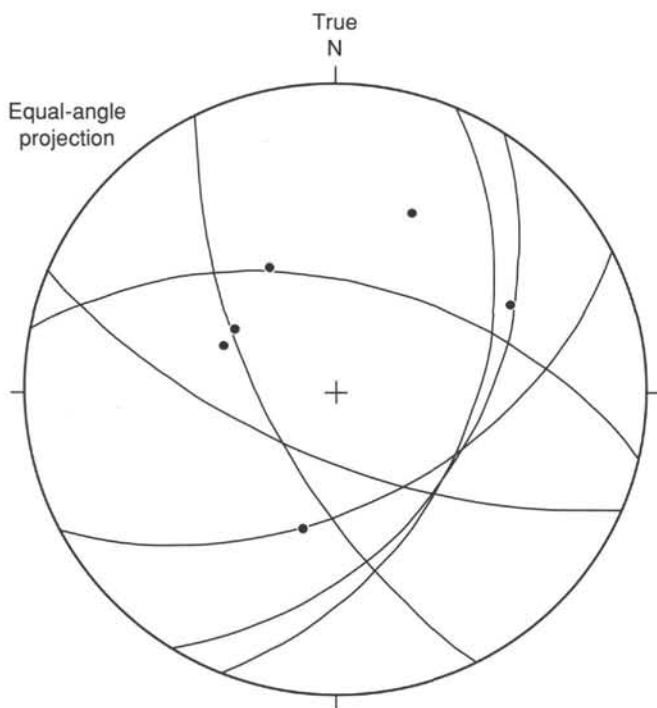


Figure 20. Equal-angle stereographic projection of joint planes in igneous basement, Hole 835B.  $N = 6$ .

21). Calcareous nannofossils are abundant and well preserved throughout all cores, but planktonic foraminifer assemblages are less diverse and poorly preserved in Unit I in Cores 135-835A-3H and -4H and in the lower part of Unit II.

The sediments at this site range from middle Pleistocene to late Pliocene in age. The middle Pleistocene fauna occurs in Cores 135-835A-1H to -2H. The middle/early Pleistocene boundary is thought to be at the base of Core 135-835A-2H. The Pleistocene/Pliocene boundary (base of nannofossil Subzone CN14a of Okada and Bukry, 1980) is within Core 135-835A-9H. However, slumped material that includes late Pliocene calcareous nannofossils ranging from Subzone CN12a to CN13b was found from the lower part of Core 135-835A-6H to the upper part of Core 135-835A-8H. Detailed interpretation of this interval is not made at this time, as more extensive, shore-based studies are needed.

The sediments just above the basaltic basement contain a late Pliocene flora and fauna that indicates the nannofossil Subzone CN12a of Okada and Bukry (1980) and the planktonic foraminifer Zone N21 of Blow (1969). The biostratigraphic results for Holes 835A and 835B are summarized in Figures 21 and 22.

### Calcareous Nannofossils

Calcareous nannofossils of Pleistocene and late Pliocene age are abundant and well preserved in the 160 m of sediment recovered at Site 835. Nannofossils in the core intervals 135-835A-1H-CC through -9H-3, 51–55 cm, indicate deposition during the Pleistocene (Subzone CN14a or later); whereas the interval of core between 135-835A-9H-4, 30–31 cm, and -18H-CC is assigned to the late Pliocene (Zone CN12). Characteristic Pleistocene forms are absent from this Pliocene interval. It should be noted, however, that taxa characteristic of these late Pliocene zones are reworked throughout the younger section. This reworking ranges from common to rare. Some of the section assigned to Zone CN12 (especially Subzone CN12a) may actually represent late Pliocene (Subzones CN12b–CN12d) deposition.

A large mass of reworked upper Pliocene sediment occurs within Pleistocene sediment of Zone CN14 and extends from the lower part of Core 135-835A-6H to the upper part of Core 135-835A-8H (Fig. 21). At the base of this reworked upper Pliocene unit is an interval that contains more than 50% late Pliocene flora mixed with Pleistocene floras. This mixture may represent disturbance of Pleistocene sediment by the mass of upper Pliocene sediment as it was redeposited.

### Pleistocene

Samples 135-835A-1H-CC through -6H-3, 100–101 cm, and Sample 135-835B-1R-CC are assigned to Subzone CN14a or younger. These samples contain well-preserved floras including *Gephyrocapsa oceanica*, *G. caribbeanica*, *Emiliana ovata*, and *Pseudoemiliana lacunosa*. Most of these samples also contain well-preserved, reworked Pliocene floras including *Discoaster brouweri*, *D. pentaradiatus*, *D. surculus*, *D. tamalis*, and *Calcidiscus macintyreii*.

Between Samples 135-835A-6H-6, 40–44 cm, and -8H-2, 98–102 cm, is an interval where late Pliocene nannofossils occur within the Pleistocene (Figs. 21 and 23). In some cases, they are not in a normal stratigraphic sequence. Two samples from the light brown matrix (Sample 135-835A-6H-6, 40–44 and 96 cm) contain *Pseudoemiliana lacunosa*, *Emiliana ovata*, *Calcidiscus macintyreii*, and many small *gephyrocapsids*, but lack discoasters, *Gephyrocapsa caribbeanica*, and *G. oceanica*. Those samples are assigned to Subzone CN13a. Another sample below, in slightly darker sediment (135-835A-6H-6, 110 cm), contains a similar flora but *G. caribbeanica* is also present (though very rare), indicating Subzone CN13b. Sample 135-835A-6H-6, 131–136 cm, which was also taken from the slightly darker sediment,

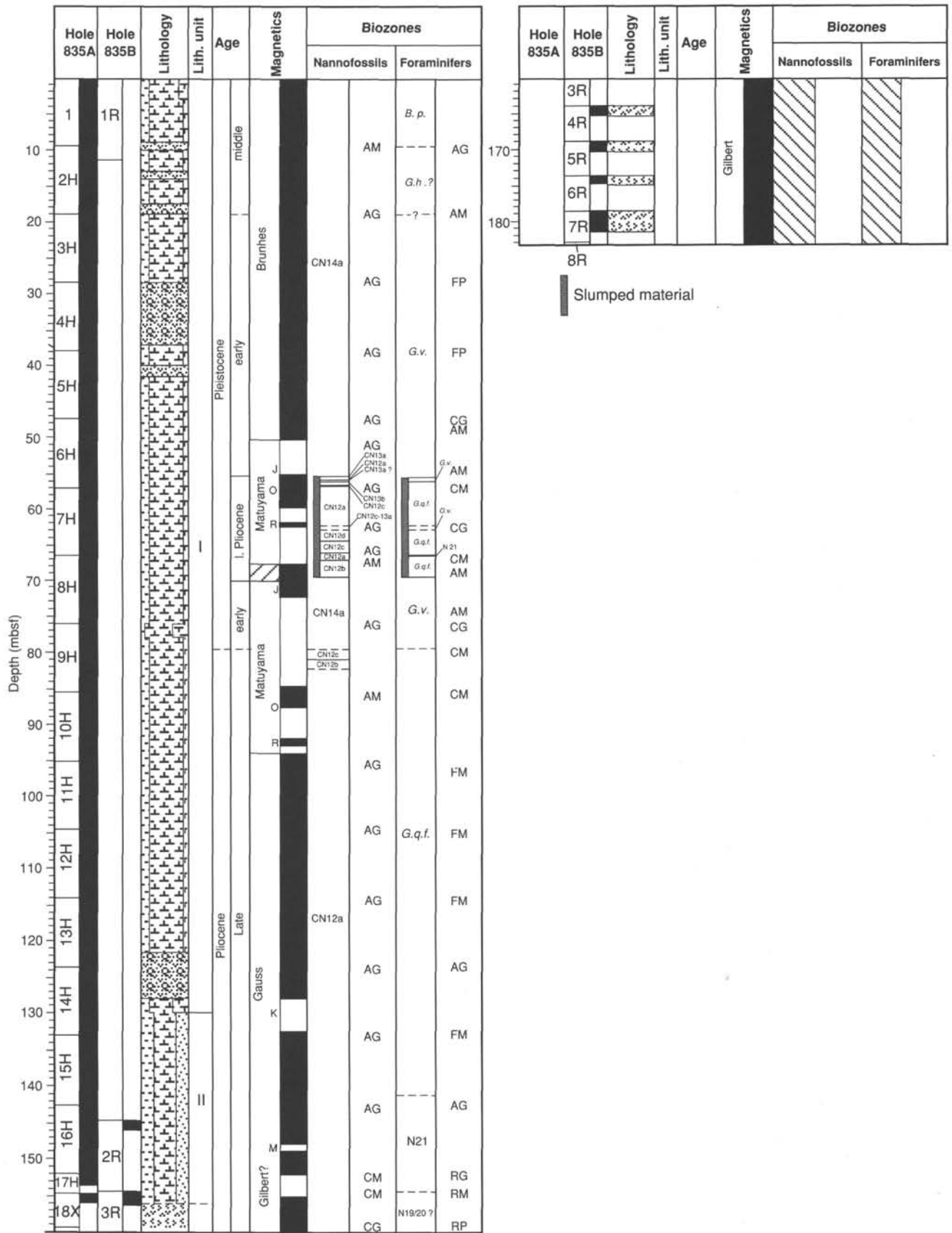


Figure 21. Paleontology summary chart, Site 835. See Figure 1 caption for an explanation of the symbols and abbreviations used.

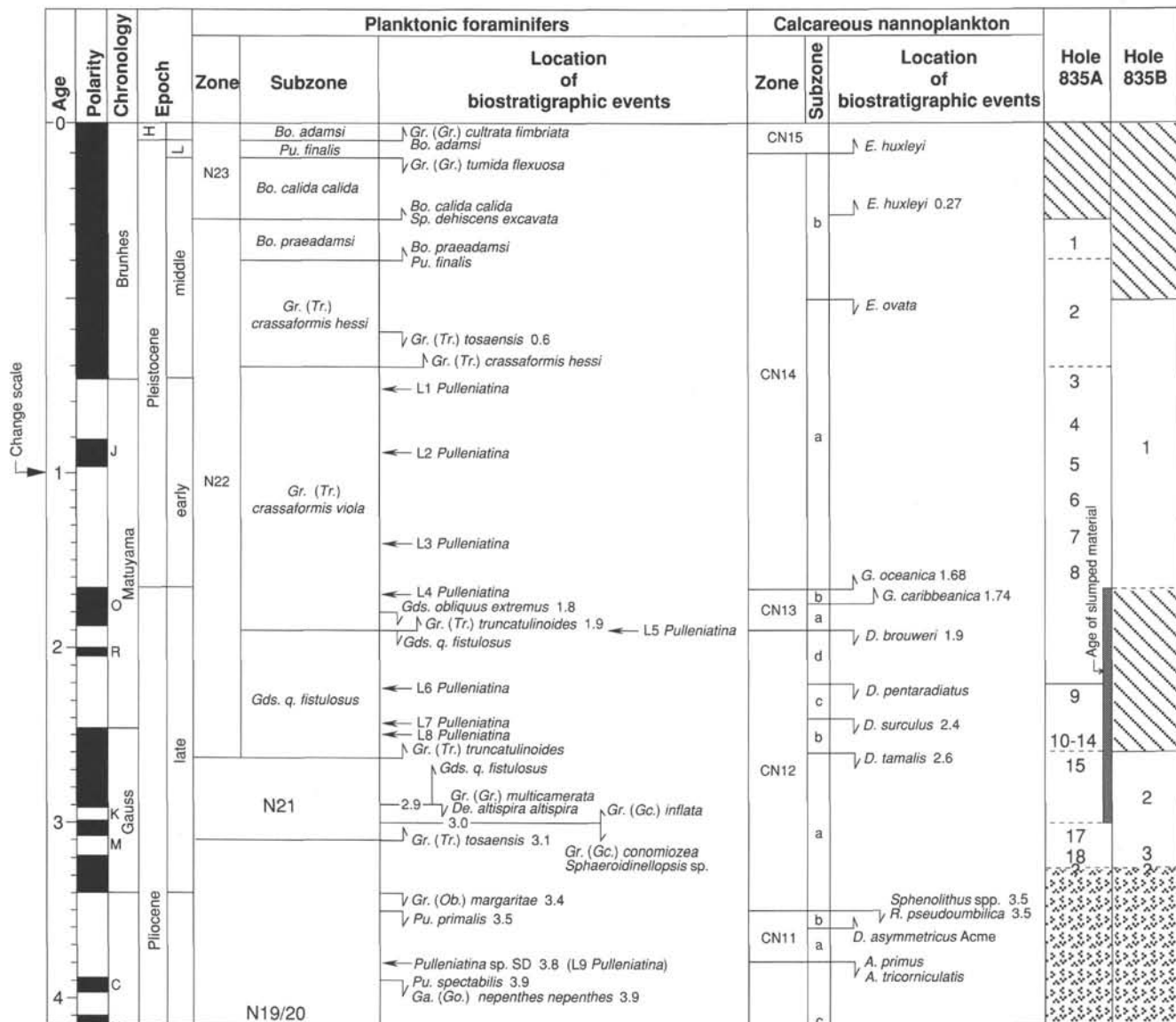


Figure 22. Biostratigraphic results, Site 835.

contains *Calcidiscus macintyreii*, *Discoaster triradiatus*, *D. brouweri*, *D. pentaradiatus*, and *H. sellii* and is assigned to Subzone CN12c. Darker brown sediment inclusions at Sample 135-835A-6H-6, 54–55 cm, are assigned to Subzone CN12a on the basis of the presence of *Discoaster asymmetricus*, *D. brouweri*, *D. pentaradiatus*, *D. surculus*, and *D. tamalis*. Sediment that appears to be of similar lithology to the dark brown inclusions in Sample 135-835A-6H-6, 54–55 cm, occurs at Sample 135-835A-6H-6, 140–144 cm, and also in Sample 135-835A-6H-6-CC. The flora is also similar and indicates Subzone CN12a. Sample 135-835A-7H-5, 80–81 cm, contains *Discoaster asymmetricus*, *D. brouweri*, *D. triradiatus*, *Calcidiscus macintyreii*, and *Amaurolithus* sp. and is assigned to Subzone CN12d.

Sample 135-835A-7H-6, 140–141 cm, includes *D. brouweri*, *D. pentaradiatus*, *C. macintyreii*, and *D. asymmetricus* and is assigned to Subzone CN12c. Sample 135-835A-7H-CC contains a similar flora but also includes *D. tamalis* and is, therefore, assigned to Subzone CN12a. The sample taken from the deepest part of the core (135-835-8H-2, 98–102 cm) lacks *D. tamalis* but includes *D. surculus* and so is assigned to Subzone CN12b.

Sample 135-835A-7H-4, 126–130 cm, contains a flora that cannot be assigned to a specific zone; therefore, it is given the range from Subzone CN12c to Subzone CN13a.

Pleistocene sediment is again present in Samples 135-835A-8H-4, 20–21 cm, through -9H-3, 50–51 cm. Reworked late Pliocene nannofossils characteristic of Subzone CN12a make up more than 50% of the floras in the two uppermost samples; reworking is minor in the Pleistocene samples below.

#### Pliocene

Sample 135-835A-9H-4, 30–31 cm, is assigned to Subzone CN12c. It yields a well-preserved abundant flora including *Discoaster brouweri*, *D. pentaradiatus*, *D. asymmetricus*, *D. triradiatus*, *Helicosphaera sellii*, and *Calcidiscus macintyreii*.

Sample 135-835A-9H-5, 70–71 cm, is placed in Subzone CN12b. It contains a similar flora to the above sample plus common *Discoaster surculus*.

Samples 135-835A-9H-CC to -18H-CC, as well as Samples 135-835B-2R-CC and -3R-CC are assigned to Subzone CN12a. They contain abundant, moderate- to well-preserved floras in-

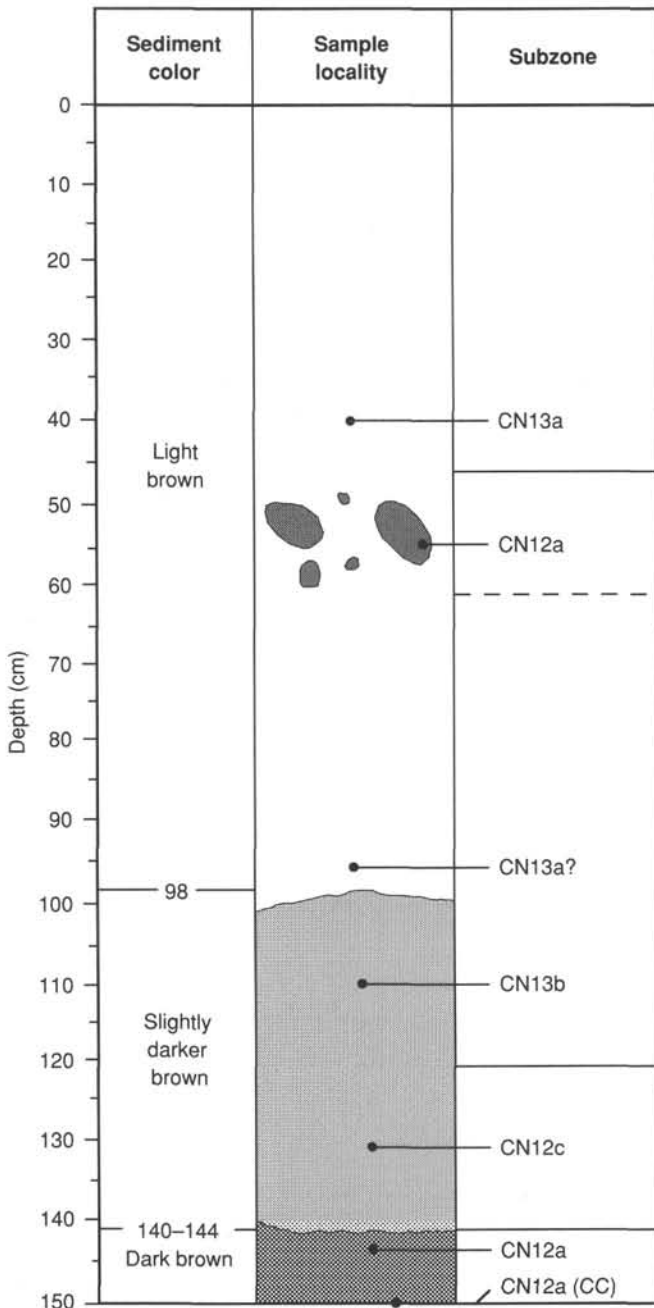


Figure 23. Occurrence of calcareous nannofossils in Section 135-835A-6H-6.

cluding *Discoaster brouweri*, *D. pentaradiatus*, *D. surculus*, and *D. tamalis*.

**Planktonic Foraminifers**

A total of 21 core-catcher samples and 7 additional samples from within the cores were examined for planktonic foraminifers at Site 835. Twenty-six of the samples from Hole 835A contain abundant to common and well- to moderately preserved planktonic foraminiferal faunas ranging in age from the Pleistocene to the late Pliocene. These assemblages, however, are less diverse and poorly preserved in Samples 135-835A-3H-CC, -4H-CC, and -16H-CC to -18H-CC.

Three samples from Hole 835B were analyzed. Sample 135-835B-1R-CC yielded a Pleistocene foraminiferal fauna with re-

worked upper Pliocene assemblages, but Samples 135-835B-2R-CC and -3R-CC were barren of planktonic foraminifers.

**Middle Pleistocene**

Samples between 135-835A-1H-CC and -2H-CC are assigned to the middle Pleistocene *Bolliella praeadamsi* Subzone and to the *Globorotalia (Truncorotalia) crassaformis hessi* Subzone, based on the occurrence of *Gr. (Tr.) truncatulinooides*, along with *Globorotalia (Globorotalia) tumida tumida*, *Pulleniatina obliquiloculata* (dextral coiling), *Globorotalia (Globorotalia) cultrata menardii*, *Globigerinoides conglobatus*, *Neogloboquadrina duertrei*, and *Gr. (Gr.) cultrata neoflexuosa*. The occurrence of *Bolliella praeadamsi* indicates that the assemblage of Sample 135-835A-1H-CC is comparable to the *B. praeadamsi* Subzone. Sample 120-835A-2H-CC contains *Globorotalia (Truncorotalia) crassaformis hessi* and is thought to be correlative with the *Gr. (Tr.) crassaformis hessi* Subzone. *Globorotalia (Truncorotalia) tosaensis* is present in Sample 135-835A-1H-CC, indicating reworking from either the basal part of Zone N22 or from Zone N21 of Blow (1969).

**Lower Pleistocene**

The interval between 19 and 79.5 mbsf (Samples 135-835A-3H-CC to -8H-CC) is early Pleistocene (*Globorotalia [Truncorotalia] crassaformis viola* Subzone) in age on the basis of the co-occurrence of *Gr. (Tr.) tosaensis* and *Gr. (Tr.) truncatulinooides*, along with *Gr. (Gr.) tumida tumida*, *Gr. (Globoconella) inflata*, *Globigerinoides conglobatus*, *Gds. ruber*, *Gds. elongatus*, *Sphaeroidinella dehiscentis*, *Pulleniatina obliquiloculata* (dextral coiling), *Hastigerina pelagica*, and *Globorotalia (Truncorotalia) crassaformis ronda*. Samples 135-835A-3H-CC and -4H-CC, however, contain volcanic glass shards, and most foraminiferal specimens are small (<250 µm). The planktonic foraminifer assemblages are less diverse and not well preserved. They consist mainly of *Gds. ruber*, *Globigerinita glutinata*, *Globorotalia (Truncorotalia) crassaformis crassaformis*, *Globorotalia (Obandiyella) bermudezi*, and pink- and white-colored *Globigerina (Globo-turborotalia) rubescens*.

**Upper Pliocene**

Samples 135-835A-9H-CC to -14H-CC yielded a moderately preserved assemblage of planktonic foraminifers assignable to the late Pliocene *Globigerinoides quadrilobatus fistulosus* Subzone of Chaproniere (in press) and to Zone N21 of Blow (1969). The age is based on the co-occurrence of *Gr. (Tr.) truncatulinooides*, *Gr. (Tr.) tosaensis*, and *Gds. quadrilobatus fistulosus*. Other representative species in this interval are *Gr. (Gr.) tumida tumida*, *Gr. (Gr.) multicamerata*, *Gr. (Tr.) crassaformis ronda*, *Gr. (Tr.) crassaformis crassaformis*, *S. dehiscentis*, *Gds. conglobatus*, *Gds. obliquus extremus*, *Gds. ruber*, and *Gds. elongatus*.

These late Pliocene faunal assemblages were found between Pleistocene assemblages in the slumped material that extends from the lower part of Core 135-835A-6H to the upper part of Core 135-835A-9H. Two samples (135-835A-6H-6, 131-136 cm, and -7H-7, 25-29 cm) taken from the slumped material are thought to be correlative with the lower part of the *Gds. quadrilobatus fistulosus* Subzone because sinistrally coiled populations of *Pulleniatina obliquiloculata* were found in these samples. Sample 135-835A-7H-CC is assigned to Zone N21 of Blow (1969) based on the lack of *Gr. (Tr.) truncatulinooides*. Sample 135-835A-7H-4, 126-130 cm, contains the early Pleistocene to latest Pliocene planktonic foraminifer fauna that is assigned to the *Gr. (Tr.) crassaformis viola* Subzone. A detailed analysis of the structure and biostratigraphy within the slumped material will be done at a later date.

Sample 135-835A-15H-CC is composed of foraminiferal sandstone and dark gray mudstone. The former contains an abundant and well-preserved late Pliocene assemblage, but small and few specimens were found in the mudstone. The late Pliocene fauna of this sample is referable to the lower part of Zone N21 of Blow (1969), based on the presence of *Gr. (Tr.) tosaensis* and the absence of *Gr. (Tr.) truncatulinoides*. Co-occurring species are *Globorotalia (Globorotalia) cultrata limbata*, *Gr. (Gr.) multicamerata*, *Gds. ruber*, *Gds. elongatus*, *Gds. obliquus extremus*, and *Sp. dehiscens*.

Samples 135-835A-16H-CC to -17H-CC contain few, small, poorly preserved and broken specimens of foraminifers from volcanic sandstone and silt beds. Better preserved calcareous nannofossils are present as at Site 834. The occurrence of *Sphaeroidinellopsis seminulina* in Sample 135-835A-17H-CC suggests a level within the upper part of Zone N19/20.

### SEDIMENT ACCUMULATION RATES

Pleistocene calcareous planktonic assemblages are generally abundant and well preserved, but throughout the late Pliocene the planktonic foraminifer faunas deteriorate, diversity is lower, and in some samples, only forms smaller than 250  $\mu\text{m}$  are present.

Figure 24 is a graphic presentation of depth and age data from Site 835. The ages are based on the bioevents presented in Table 5. In addition, paleomagnetic data have been superimposed on the biostratigraphic data. Both sources of data overlap for most of the plot, differing only where data from both sources are poor.

The curve may be divided into four sections. Section A, ranging through the lower part from the bottom of the hole to 86 mbsf, shows fairly rapid sedimentation rates of about 97 mm/k.y. From 86 to 77 mbsf (Section B) rates of accumulation slowed markedly to approximately 4 mm/k.y. The interval between 77 and 38 mbsf (Section C) represents a disturbed interval where a 39-m slump block was emplaced during a 70,000-yr interval (based on paleomagnetic data), probably as a single raft. Thereafter, from 38 mbsf to the seafloor (Section D) the rate of sedimentation returned to

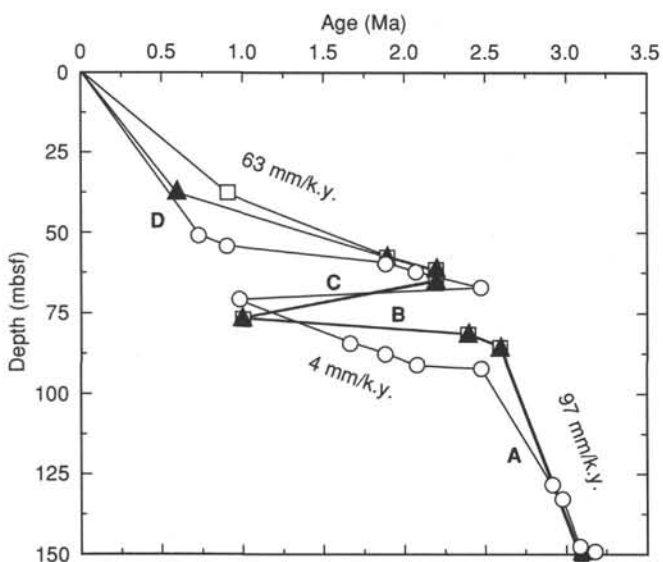


Figure 24. Graphic representation of age vs. depth data illustrating sedimentation rates at Site 835 by means of the bioevents and depths given in Table 5. A plot of the paleomagnetic data is also included for comparison. Sections A to D are discussed in the text. Open squares = biostratigraphic data, filled triangles = biostratigraphic data with modified ages for *Globorotalia (Truncorotalia) tosaensis*, and open circles = paleomagnetic data.

Table 5. Depths and ages of bioevents used to plot sediment accumulation rates for Site 835.

Depth (mbsf)	Age (Ma)	Events
38.0	0.6	LAD <i>G. tosaensis</i>
58.0	1.9	LAD <i>G. q. fistulosus</i>
62.0	2.2	LAD * <i>G. (G.) multicamerata</i>
63.0	1.0	*Interpreted
65.0	2.2	LAD * <i>G. (G.) multicamerata</i>
77.0	1.0	*Interpreted
82.0	2.4	LAD <i>D. surculus</i>
86.0	2.6	LAD <i>D. tamalis</i>
150.0	3.1	FAD <i>G. (T.) tosaensis</i>

\*Estimate based on paleomagnetic data.

values approaching that of the lower part of the core, with rates of about 63 mm/k.y. It should be noted that the rate of sedimentation within the slump block is very close to that of Section B, immediately before the slumping. No obvious changes are present in the fossil assemblages that would explain the slowing in sedimentation rates over the interval from the latest Pliocene to earliest Pleistocene. Although some dissolution effects in the planktonic foraminifer assemblages are obvious, they are less than those observed lower in the Pliocene at this site.

### PALEOMAGNETISM

#### Remanent Magnetism

Most remanent magnetization measurements were made with the pass-through cryogenic magnetometer on archive halves of cores. All of these measurements were made at a spacing of 5 cm. After measuring the natural remanent magnetization (NRM), most sediment cores were subjected to stepwise alternating-field (AF) magnetic cleaning at 5, 10, and 15 mT. In some cases, the AF demagnetizations were abbreviated to 0 and 15 mT to speed the core flow through the laboratory. For most basalt cores, AF steps of 2, 5, 10, and 15 mT were used. A few discrete sediment samples and one basalt sample were also analyzed using the Molspin Minispin spinner magnetometer, the Schonstedt GSD-1 AF demagnetizer, and the Molspin pulse magnetizer to investigate the magnetic properties in greater detail.

Sediments in Cores 135-835A-1H through -17H were measured mainly to determine magnetic polarity stratigraphy. Oriented segments of RCB basalt cores from Hole 835B were also measured with the pass-through magnetometer to determine magnetic polarity. In addition, four samples from sedimentary rocks overlying basement were analyzed with the spinner to investigate an important polarity interval.

#### Magnetic Properties

The un lithified sediments at Site 835 are very similar to those of Site 834, although ash layers are less abundant. The equivalent of Unit I in Hole 834A extends down to 130 mbsf, whereas Unit II of Hole 834A is equivalent to the lower part of Hole 835A (see "Lithostratigraphy" section, this chapter).

The sediment color is often dark reddish brown as a result of abundant iron, mainly contained in ferric oxyhydroxides (see "Lithostratigraphy" section, this chapter). Isothermal remanent magnetization (IRM) acquisition curves (Fig. 25) show a rapid saturation with increasing field strength, indicating that the magnetic grains within these sediments behave like magnetite; this IRM is easily removed from discrete samples by AF demagnetization typically between 20 and 30 mT. As the sediments have abundant amorphous iron oxyhydroxides and as darker samples have greater amounts of these materials and generally have low

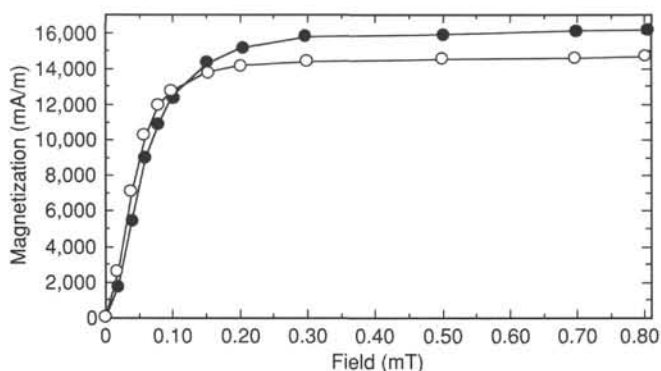


Figure 25. Isothermal remanent magnetization (IRM) curves for two sediment samples, Hole 835A. Both display saturation in low applied fields, indicating magnetite-type behavior. Filled circles = Sample 135-835B-5H-4, 30–32 cm, and open circles = Sample 135-835B-15H-4, 30–32 cm.

median destructive fields (see below), it is inferred that in these samples ferric oxyhydroxides seem to have low coercivity values and easily acquire an IRM.

The natural remanent magnetization (NRM) intensity of the sediments is remarkably constant downhole, typically averaging 200 mA/m, with a range between 1 and 1500 mA/m. These strong magnetizations probably result from volcanic material contained in the sediments as well as from the propensity of the sediment to acquire a large drill-string-induced IRM. This pervasive upward overprint, which gives the sediments (and often also the basalts) NRM inclinations near  $-90^\circ$ , completely masks their intrinsic polarities. The sediments acquire a strong drill-string IRM because many of their magnetic grains have low coercivity values, as shown by the low median destructive field (MDF) values of typically 2–4 mT (Fig. 26). However, as it resides in low coercivity grains, this overprint is easily removed with AF demagnetization (Fig. 25), leaving a more stable, characteristic remanence that holds geologic information.

Some sediment samples, usually lighter brown muds, have much higher coercivity values; orthogonal (Zijderveld) plots show these to be directionally stable (Fig. 27), as is also evidenced by the slow decay of remanent intensity by AF demagnetization (Fig. 26, Sample 135-835-5H-4, 30–32 cm).

Typical basalt NRM magnetization intensities range from about 1 to 10 A/m. These rocks also displayed a drill-string IRM to a lesser extent than the sediments from Hole 835A, as was found at Hole 834B, but the amount of overprint is variable. Some samples had low MDFs (8 mT or less) and low coercivity magnetization components, so they acquired a greater drill-string IRM (Fig. 28). Other samples had MDFs greater than 10 or 15 mT, so they were less affected (Fig. 28).

As with the Hole 835A sediments, AF demagnetization above 30–40 mT easily removed any drill-string overprint to reveal a stable characteristic remanent magnetization. However, because AF demagnetization of the archive core halves during Leg 135 was limited to 15 mT, characteristic magnetizations may not always have been isolated and so the measurements made with the pass-through magnetometer must be regarded as reconnaissance results only.

### Magnetic Polarity Stratigraphy

The sediments of Hole 835A showed a strong drill-string-induced IRM masking the true NRM polarities as did the sediments in Hole 834A, although 15-mT AF demagnetization usually revealed an interpretable polarity record. That the 15-mT level is not the optimum choice for these sediments is evidenced by the

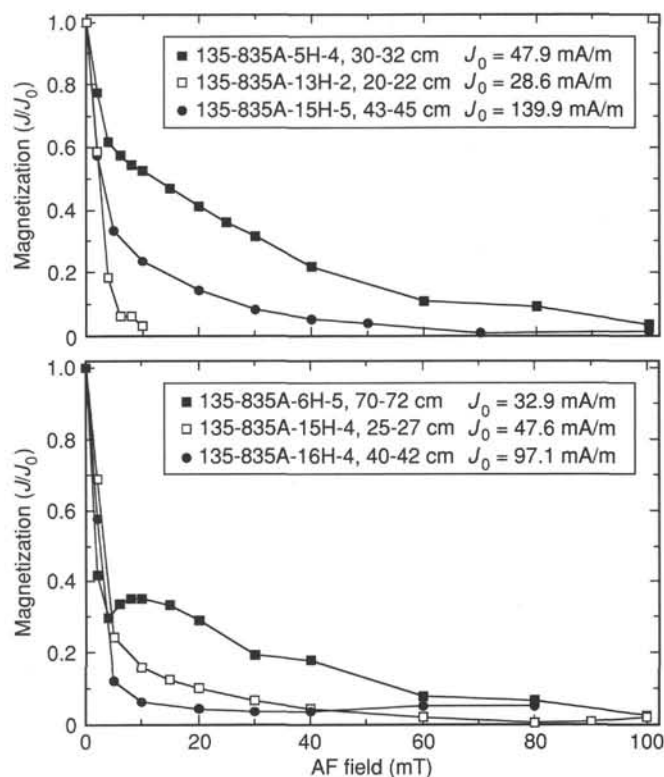


Figure 26. Behavior of sediment samples, Hole 835A, during alternating field (AF) demagnetization. The sediments display a wide range of mean destructive fields (MDF) from 2 to 12 mT. Much of the natural remanent magnetization (NRM) is thought to be IRM induced by the drill string.  $J_0$  = NRM intensity for each sample.

remaining asymmetries notable in the normal and reversed inclinations (Fig. 29).

Figure 29 shows both “observed” and “interpreted” polarity for Hole 835A, as the polarity interpretation was not as straightforward as that of Hole 834A. Reversed polarity is sometimes noted by a change from steep inclinations to values near zero. Declination switches usually show reversals, although in a few places there are changes in inclination without changes in declination. Such cases are assumed not to be reversals; they may be portions of the core for which drill-string-induced IRM was not removed as completely.

In contrast with Hole 834A, the sediments in Hole 835A are generally much more disturbed. In some cores, slump textures were noted that contained basalt pebbles, cobbles, or reworked mud clasts. This is particularly the case with Cores 135-835A-4H and -14H (see “Lithostratigraphy” section, this chapter). In addition, a large Pliocene slump block, recognized on an interrupted biostratigraphic record (see “Biostratigraphy” section, this chapter), was noted from Sections 135-835A-6H-4 to -8H-2 (i.e., ~52–70 mbsf). Also, numerous cores that have a high water content and/or clasts were evidently disturbed by drilling and cutting processes. As a result of these disturbances, there are many intervals where magnetic polarity is uncertain.

Nevertheless, a relatively clear polarity stratigraphy of Hole 835A was produced, as shown in Figure 29 and Table 6. At the bottom and top of the hole are long intervals of normal polarity, corresponding to the Gauss and Brunhes epochs, respectively. Within the Gauss Chron, we recognized the Kaena and Mammoth reversed subchrons. At the bottom of the Brunhes Chron, we recognized the reversed upper part of the Matuyama Chron between the Jaramillo Subchron and the base of the Brunhes Chron.

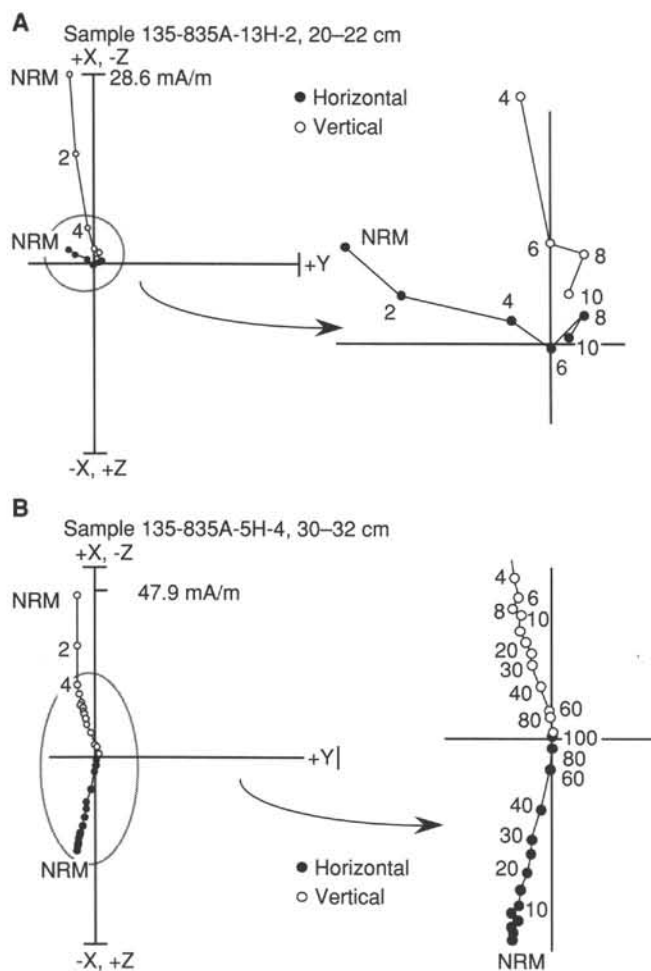


Figure 27. Orthogonal vector plots showing the directional behavior of two sediment samples from Hole 835A during AF demagnetization. **A.** Sample with low coercivity and large drill-string-induced IRM. **B.** Sample with higher coercivity and smaller drill-string overprint.

Between these two normal chrons is an interval of dominantly reversed polarity that appears to be the Matuyama Chron. However, normal polarity subchrons present in the core showed neither the "expected" spacing, nor the "expected" length or number. This part of the core is also the interval containing the allochthonous block of Pliocene material, as inferred from the biostratigraphy. The biostratigraphy suggests breaks between Samples 135-835A-6H-3, 100–102 cm, and -6H-1, 40–42 cm (51.1–55.5 mbsf) and between 135-835A-8H-2, 98–100 cm, and -8H-3, 70–72 cm (69.0–70.7 mbsf). Both breaks occur within normal polarity intervals.

Given this constraint, we suggest that the break at 51.5–55.5 mbsf places the upper Jaramillo against the lower Olduvai, both normal polarity subchrons. This interpretation explains the inordinate length of the normal interval in the usual position of the Jaramillo Subchron. We furthermore interpret the short normal polarity zone beneath this to be the Réunion Event (at 62.7 mbsf). We also think that the normal interval at 84.4–87.9 mbsf and the short normal subchron beneath it (at 92.4–92.7 mbsf) are the Olduvai and Réunion subchrons repeated. The normal polarity interval from 67.7 to 71.3 mbsf appears to be the Gauss/Matuyama boundary at its top and the bottom of the Jaramillo at its bottom, which is supported by a biostratigraphic break in this layer. Furthermore, we noted a small reversal of normal polarity beneath

the Jaramillo, which is probably the Cobb Mountain Event, similar to that observed in Hole 834A.

Thus, the magnetic polarity stratigraphy is consistent with the emplacement of a slump block of Pliocene sediments at Site 835 during the Jaramillo Subchron (0.93–0.98 Ma). This block consisted of a section extending from the top of the Gauss Chron to the middle of the Matuyama Chron, including the Réunion and Olduvai subchrons, thus causing a repetition of part of the magnetostratigraphic column. The allochthon remained magnetically coherent, as it did not lose its original magnetic signature during the movement.

Using the magnetic stratigraphy (Fig. 29), the geomagnetic polarity reversal time scale of Berggren et al. (1985), and adding to this an age for the middle of the Réunion Subchrons (2.08 Ma, mean of ages for Réunion 1 and Réunion 2, as given in Harland et al., 1982), an age vs. depth curve was constructed for the upper 153 mbsf of Hole 835A (Fig. 30 and Table 6). This curve implies an age of 3.2 Ma for a depth of 149.1 mbsf at the base of the Mammoth Subchron.

Sedimentation rates deduced for different intervals of Hole 835A (Fig. 30) differ considerably. During the Brunhes and Gauss chrons, the sedimentation rate was high (about 62 and 78 mm/k.y., respectively). Much lower rates are inferred for the Matuyama sections (approximately 18 mm/k.y. for the autochthonous and 20 mm/k.y. for the allochthonous Matuyama sections, respectively). Furthermore, the short depth interval between the top of the Gauss Chron and the Réunion Event, where the bottom part of the sedimentation curve bends sharply (Fig. 30), suggests that there may be a hiatus in sedimentation between those two events (2.08–2.47 Ma).

Magnetic polarity was also determined for Hole 835B using oriented pieces of basalt and sediment, 7–8 cm in length or longer, from the archive core halves. A predominantly normal polarity was found in Sections 135-835B-3R-2 through -7R-3 (156–183 mbsf; Fig. 31 and Table 7). The polarities of the sporadic reversed polarity samples within the normally magnetized basement may result from two possible causes. They may be overturned pillows or, as in the case of Sample 135-835B-7R-2, 22–24 cm, they may have a reversed polarity overprint.

The reversed polarity samples above 155 mbsf are a different matter. Section 135-835B-3R-1 contains about 0.7 m of sedimentary rocks overlying basement. One piece of this rock was measured with the pass-through cryogenic magnetometer and found to have a reversed polarity. As this is the same polarity recorded by the deepest sediments in Hole 835A, four oriented minicores were obtained from these sediments to verify the reversal. All four samples had stable remanent magnetizations with little overprint and MDFs ranging from 29 to 41 mT. Furthermore, they yielded orthogonal vector plots (Fig. 32), clearly showing that clean, stable, characteristic remanence directions were isolated, with inclinations ranging from 28° to 44°. The positive inclinations indicate a reversed polarity in the Southern Hemisphere, and the samples' behavior during demagnetization confirms that the reversed polarity is reliably measured.

The reversed polarities of the sediment samples suggest that the sediment must be of polarity Subchron 2Ar age or older. Therefore, the underlying normal polarity basalts must be older than Subchron 2Ar (i.e., 3.88 Ma, the end of the normal polarity Cochiti Subchron of the Gilbert Chron). This is somewhat older than expected for basement at this site.

### Magnetic Susceptibility

Volume magnetic susceptibility was measured on a routine basis on whole (i.e., unsplit) core segments of sediments and basalts from Holes 835A and 835B, whenever the core sections appeared to be relatively full. The measurements were made every

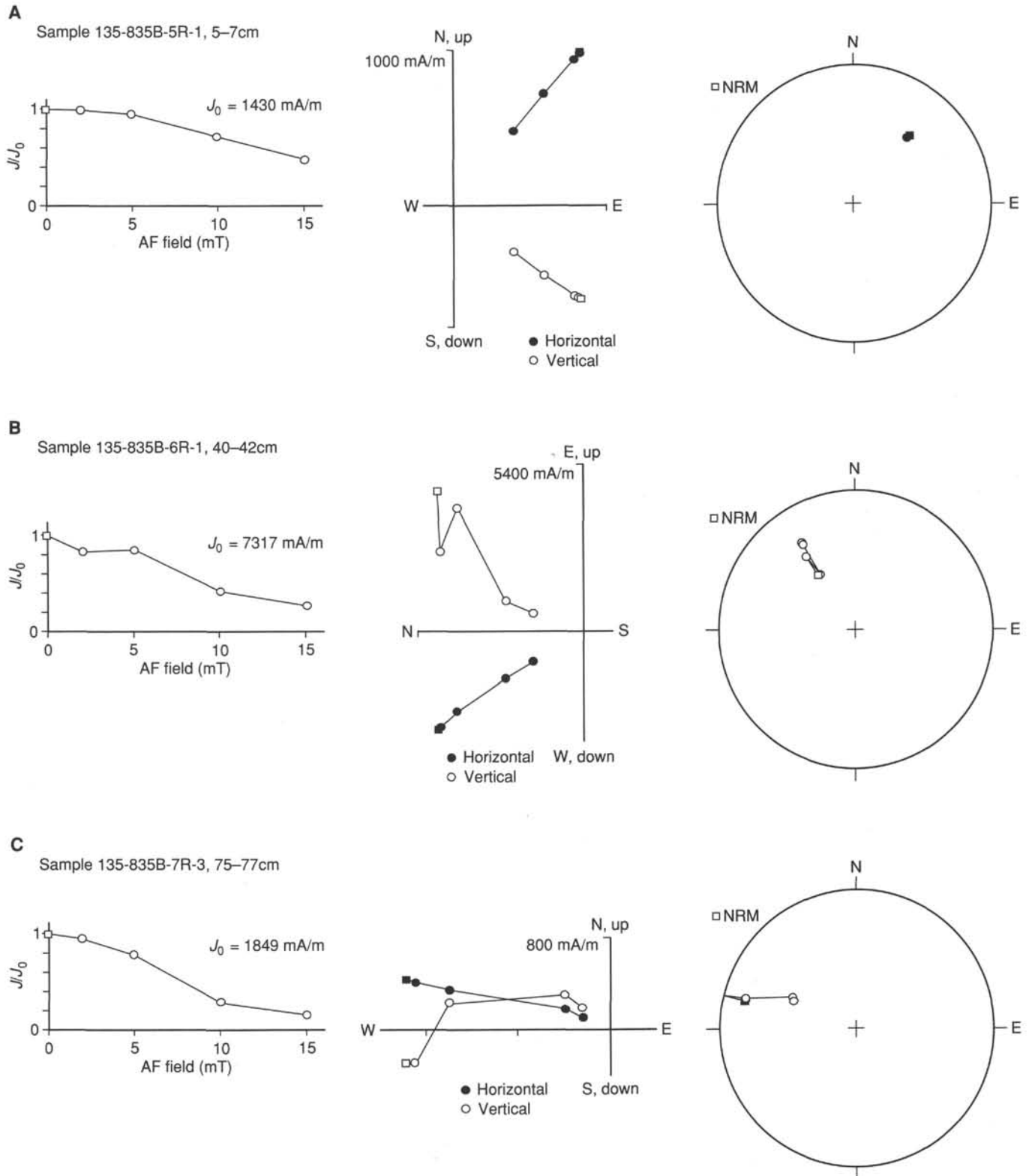


Figure 28. Behavior of basalt samples, Hole 835B, during AF demagnetization. **A.** Sample with MDF of 15 mT and a negligible drill-string overprint. **B.** Sample with MDF of 10 mT and a drill-string overprint of moderate coercivity, which is removed between 5 and 10 mT. **C.** Sample 135-835B-7R-3, 75–77 cm, with MDF around 7 mT and a dominant drill-string overprint, which reveals an artificial reverse polarity (NRM inclination is positive) that can be removed by AF cleaning above 5 mT.

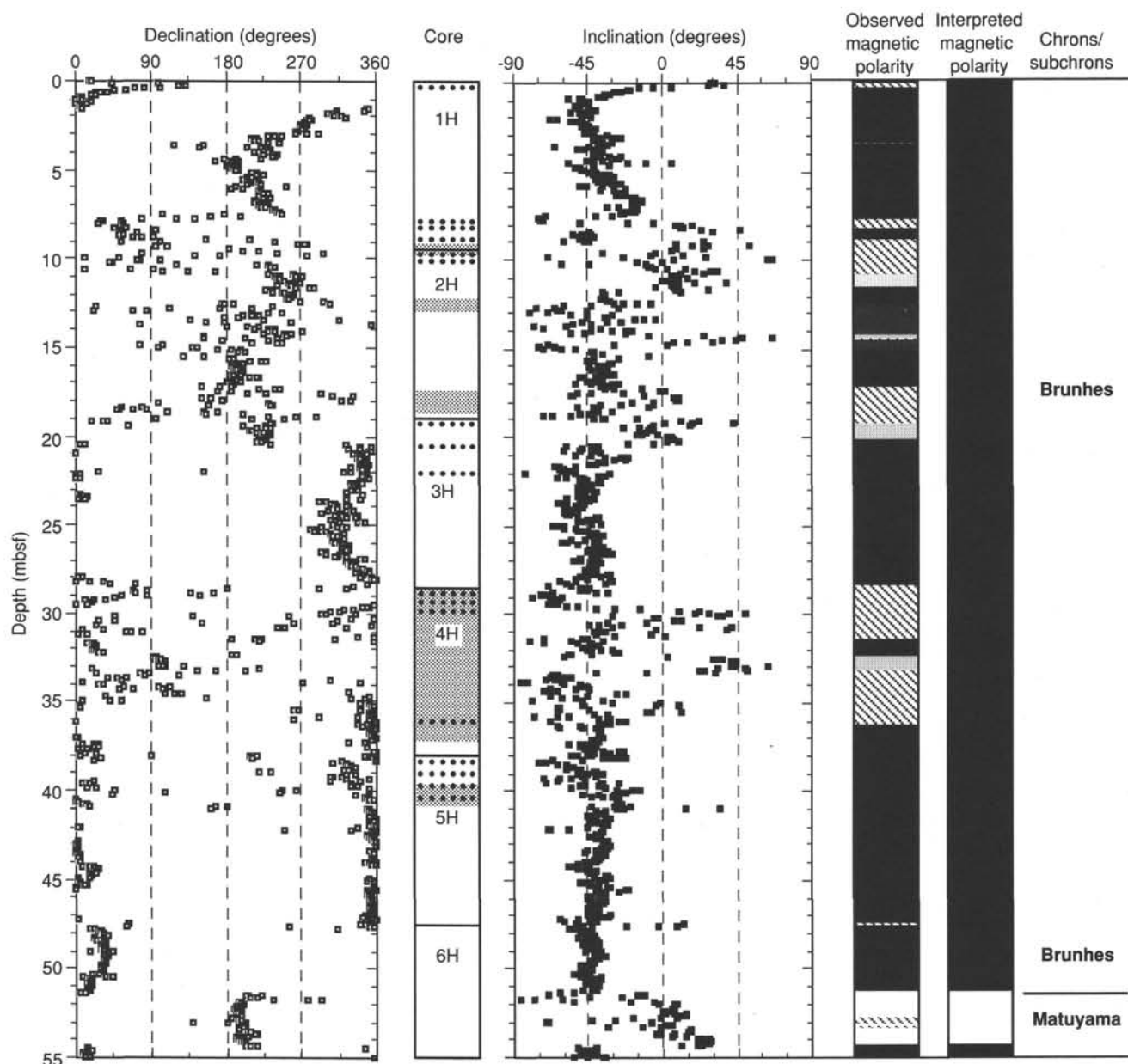


Figure 29. Magnetic polarity stratigraphy of Hole 835A. Wide columns at left and middle show the magnetization declination and inclination, respectively, measured with the pass-through cryogenic magnetometer after AF demagnetization to 15 mT. Column between declination and inclination plots indicates core boundaries, sections of core disturbed by drilling (dots), mud-clast conglomerates recognized by lithostratigraphy (gray), and allochthonous blocks recognized by biostratigraphy (wavy lines). Column at right indicates magnetic polarities, observed and interpreted (black = normal, dark gray = probably normal, hachured = indeterminate, light gray = probably reversed, and white = reversed); see Table 6. At far right, interpreted magnetic polarity chrons and subchrons are indicated. Bold type denotes polarity chron names and lines show polarity chron boundaries. Plain type indicates subchron names. Dashed lines show breaks in biostratigraphy, delineating the allochthonous sediment section.

3 cm with a Bartington MS-2 susceptibility meter with a sensor loop of 10 cm.

#### Sediment

Volume magnetic susceptibility values in Hole 835A sediments (Fig. 33) range from about  $20 \times 10^{-6}$  to  $2000 \times 10^{-6}$  cgs, with typical values between 50 and  $100 \times 10^{-6}$  cgs (geometrical mean about  $60 \times 10^{-6}$  cgs). They display both long and short wavelength variations, although not in the same fashion as was seen in the Hole 834A sediments.

Three major cycles in Unit I (0–130 mbsf) are seen, with generally high (and somewhat scattered) values at 1–2, 41–53, 76–86, and 122–127 mbsf. The susceptibility level throughout Unit I is generally more uniform than observed in Hole 834A. This uniformity suggests that the “magnetic lithology” (i.e., the content of ferromagnetic minerals) does not vary much at Hole 835A. The few spikes present in this unit are likely to be caused by the relatively few ash layers. Unit II (130–156 mbsf) shows a somewhat higher geometrical mean value (around  $10^{-4}$  cgs) as well as more scattered susceptibilities, as was also the case with Unit 2

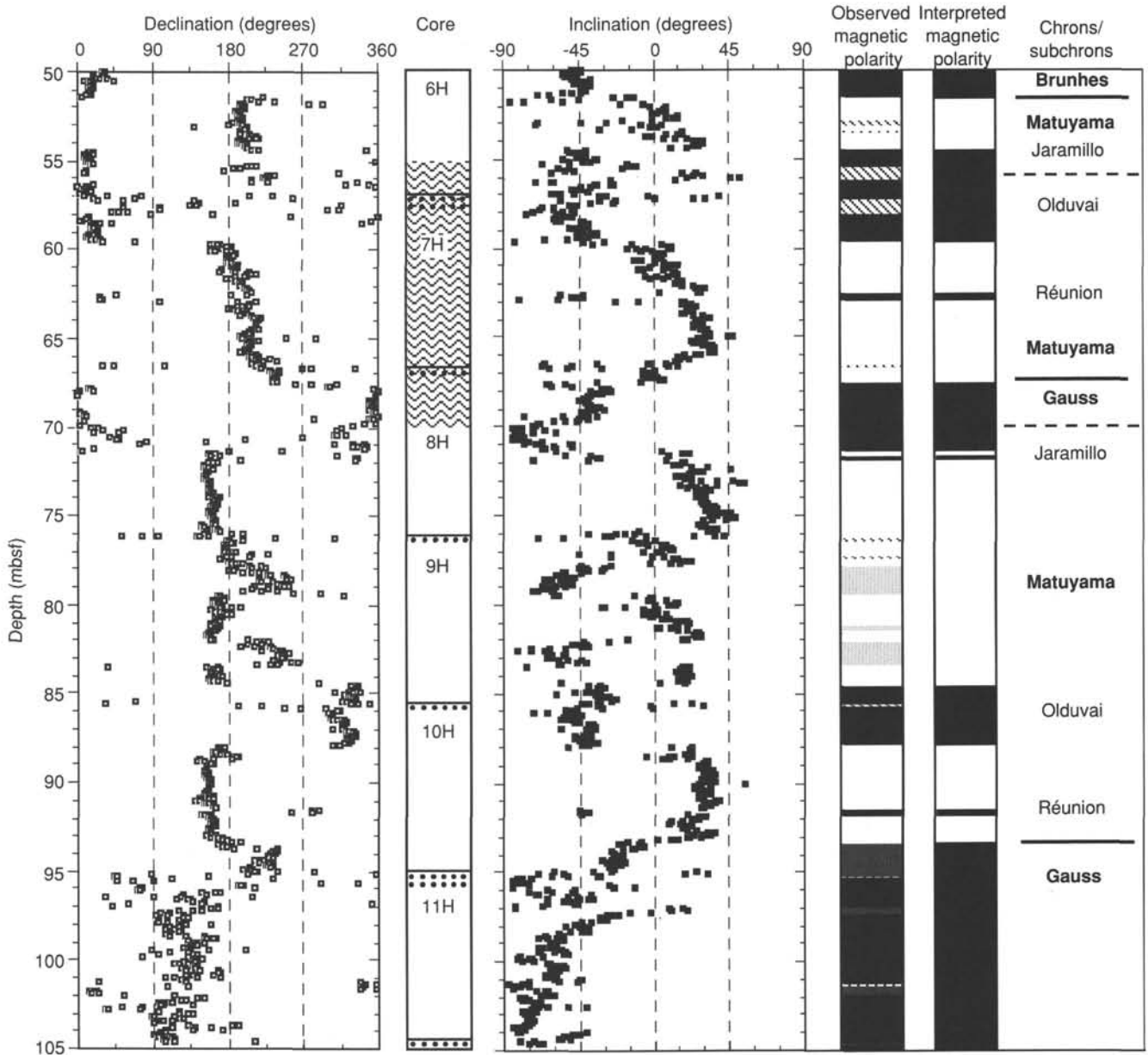


Figure 29 (continued).

of Hole 834A. This is likely to be the result of a generally higher concentration of ash in Unit 2.

A sharp offset in the susceptibility record at 69.5 mbsf (Fig. 33) may indicate the lower slump boundary at this level; a similar offset at the upper slump boundary at about 56 mbsf is not noticeable.

**Basalt**

As Hole 835B was relatively short and the recovery was poor, only a few susceptibility values were obtained (Fig. 34). As was discussed for Hole 834B, the whole-core susceptibility measurements, especially for the fragmented basalt samples, must be taken as minimum values and used for reconnaissance only. The volume magnetic susceptibility of Hole 835B ranges from  $9 \times 10^{-6}$  to  $2500 \times 10^{-6}$  cgs and a general increase of a factor of about 5 downhole is noticed, which might indicate a slight increase in the bulk content of the ferromagnetic/mafic minerals.

Modal analysis of basement rocks shows that the same general trend is indeed found in the percentages of opaque minerals and the sum of mafic silicates (olivine and pyroxenes); in detail the susceptibility at each analyzed interval mirrors these values (see "Igneous Petrology" section, this chapter, table 11). Thus, the volume susceptibility may be used as a kind of bulk indicator of the general content of ferromagnetic (in this case, titanomagnetite) and paramagnetic (olivine and pyroxene) minerals to be expected in a section of volcanics.

**Magnetic Core Orientation**

Cores 135-835A-3H through -17H were oriented using the multishot camera (see "Explanatory Notes" chapter, this volume). Usable orientation photographs were obtained for only 13 cores, as a malfunction left the film unexposed for Cores 135-835A-13H and -14H (Table 8). After orientation, Cores 135-835A-11H and

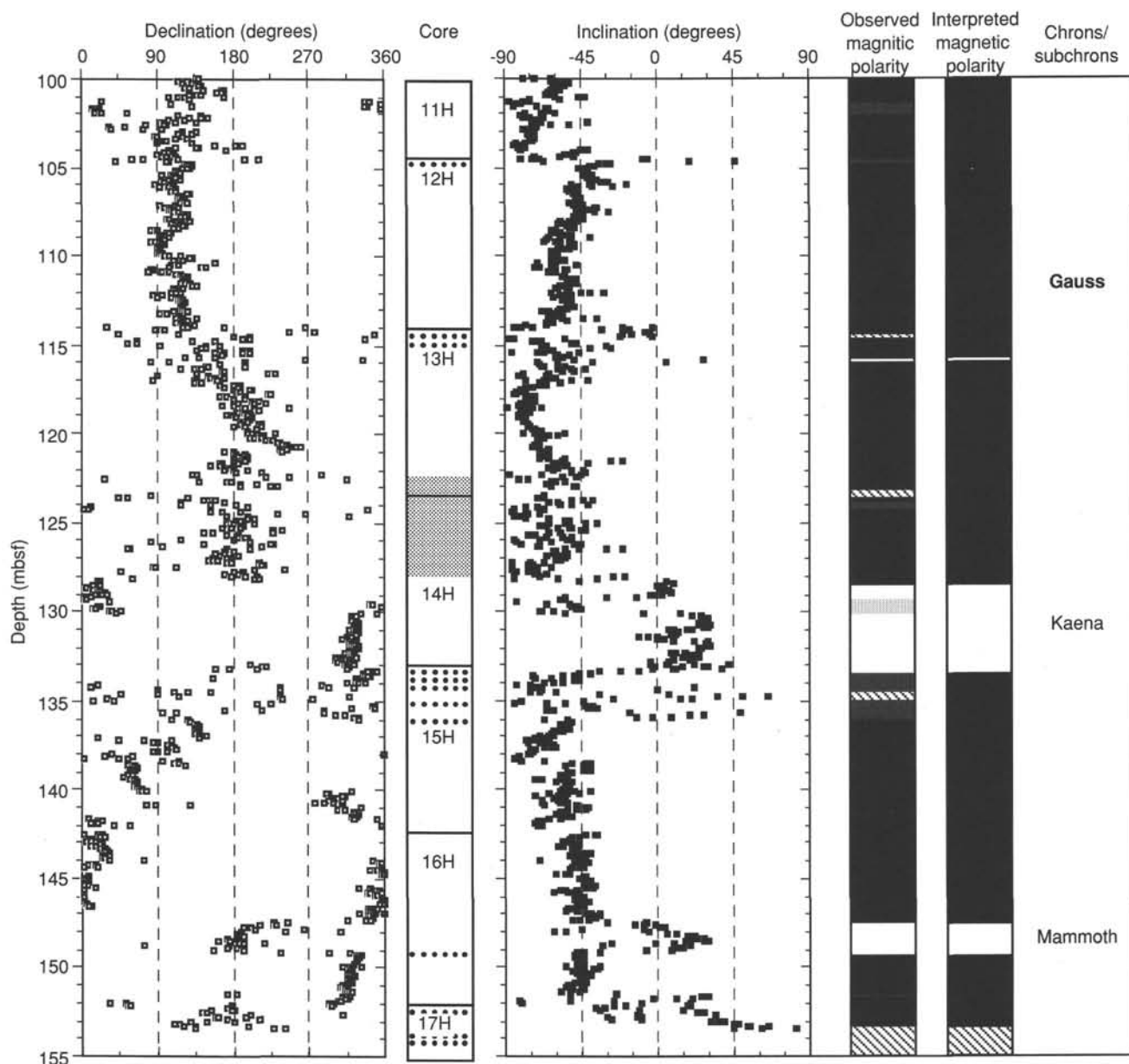


Figure 29 (continued).

-12H were found to have normal polarity inclinations but declinations between  $90^\circ$  and  $180^\circ$ , which would indicate reversed polarity. Several discrete samples were analyzed with the spinner magnetometer to ascertain whether these directions were reliable or an overprint. This test indicated that the directions are indeed reliable, and it implies that the multishot tool was placed on the sinker bar assembly backward (i.e., the orientation data are incorrect by  $180^\circ$ ).

## INORGANIC GEOCHEMISTRY

### Introduction

A total of 10 interstitial water samples were collected at Site 835. They were retrieved from every core in the uppermost 35 mbsf, by means of standard ODP squeezing techniques (see "Ex-

planatory Notes" section.). Below this depth, samples were taken every second core.

The results are summarized in Table 9, and the depth distribution is shown in Figure 35. Total alkaline earths were determined by EDTA titration; Mg is then deduced from subtraction of the calcium and strontium values (subscript [1] in Table 9). Direct Mg determination was also performed by means of flame AA spectrophotometry (subscript [2] in Table 9). Magnesium was analyzed on 1:2,000 dilution solutions of the samples. Lanthanum trichloride (10,000 ppm) was used as a releasing agent in the samples and standards. Reproducibility is about  $\pm 0.5\%$ . Differences in the Mg concentrations obtained by these two methods never exceeded 5% and were  $< 1\%$  in the most samples. Subsequent charge-balance calculations yielded sodium concentrations (1) and (2) in Table 9.

Table 6. Magnetic polarity zones, Hole 835A.

Depth (mbsf)	Polarity (N, I, R)	Age (k.y.)	Chron/subchron
0.0		0.0	BRUNHES
0.4	I		
3.6	N		
3.7	I		
7.8	N		
8.4	I		
8.8	N		
10.9	I		
11.7	R?		
12.5	N		
14.3	N?		
14.7	R?		
15.2	N?		
17.2	N		
19.4	I		
20.4	R?		
28.4	N		
31.6	I		
32.4	N		
33.4	R?		
36.3	I		
47.5	N		
47.7	I		
51.4	N	0.73	BRUNHES
52.8	R		MATUYAMA
53.1	I		
53.3	R		
53.4	I		
54.4	R	0.91	Jaramillo
55.3	N		
56.3	I		51.5–55.5 m
57.1	N		Olduvai
58.2	I		
59.6	N	1.88	Olduvai
62.6	R		
62.9	N	2.08	Réunion
66.5	R		
66.7	I		
67.7	R	2.48	MATUYAMA
	N		GAUSS

Table 6 (continued)

Depth (mbsf)	Polarity (N, I, R)	Age (k.y.)	Chron/subchron
			approx. 69.8 m (break occurs within normal period)
71.3			Jaramillo
71.6	R	0.98	
71.9	N		
76.2	R		
76.4	I		
77.2	R		
77.3	I		
77.8	R		
79.6	R?		
81.1	R		
81.3	R?		
82.0	R		
83.5	R?		
84.4	R	1.66	
85.5	N		
85.7	I		Olduvai
87.9	N	1.88	
91.3	R		
92.4	N	2.08	Réunion
92.7	R		MATUYAMA
95.1	N?	2.48	GAUSS (793.3–95.2 m)
95.2	I		
96.9	N		
97.3	N?		
101.2	N		
102.0	N?		
104.5	N		
104.7	N?		
114.2	N		
114.5	I		
115.7	N		
115.9	R		
123.0	N		
123.5	I		
123.7	N		
124.1	N?		
128.3	N	2.92	
129.2	R		Kaena
	R?		

Table 6 (continued)

Depth (mbsf)	Polarity (N, I, R)	Age (k.y.)	Chron/subchron
130.1	R		Kaena
133.3	N?	2.99	
134.3	I		Mammoth
134.9	N?		
136.0	N		
147.4	R	3.08	
149.1	N	3.18	
151.6	N?		
151.8	N		
152.1	I		GAUSS
153.4			

Notes: Magnetic polarity reversal time scale of Berggren et al. (1985), with Réunion Subchron from Harland et al. (1982) and Cobb Mountain Event from Clement and Robinson (1987). Chron names in capital letters, and subchron names in lowercase letters. Polarity code: N = normal, N? = probably normal, I = indeterminate, R? = probably reversed, and R = reversed. Divisions: heavy line = polarity chron boundary, thin line = subchron boundary, and wavy line = disconformity and age jump.

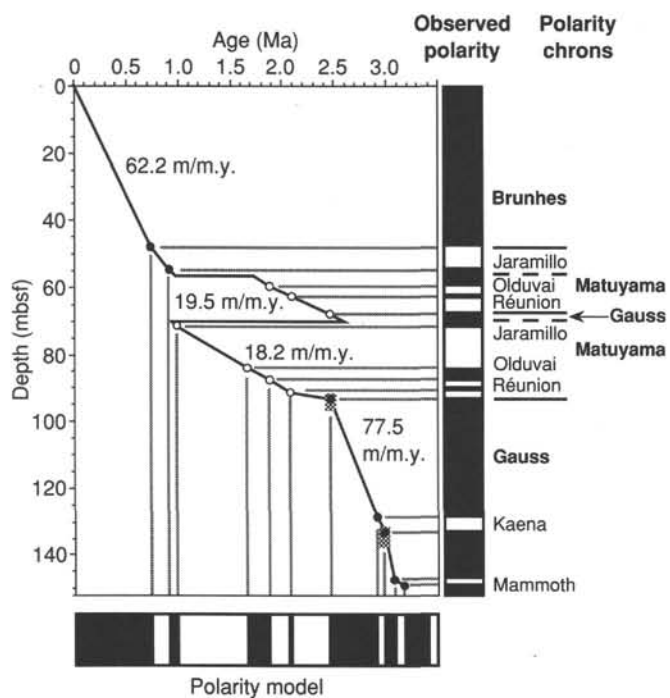


Figure 30. Age vs. depth in Hole 835A, constructed from magnetic polarity stratigraphy and geomagnetic polarity reversal time scale. Filled circles indicate points thought to be most reliable; open circles show less reliable points. Gray bars below solid circles show uncertainty in depths of certain polarity transitions. Observed polarity is shown at right, with chron and subchron names indicated in bold and plain type, respectively. Chron boundaries shown in polarity chron column by solid lines; stratigraphic breaks, by dashed lines. Polarity model of Berggren et al. (1985), with Réunion Subchron added from Harland et al. (1982), is shown at bottom.

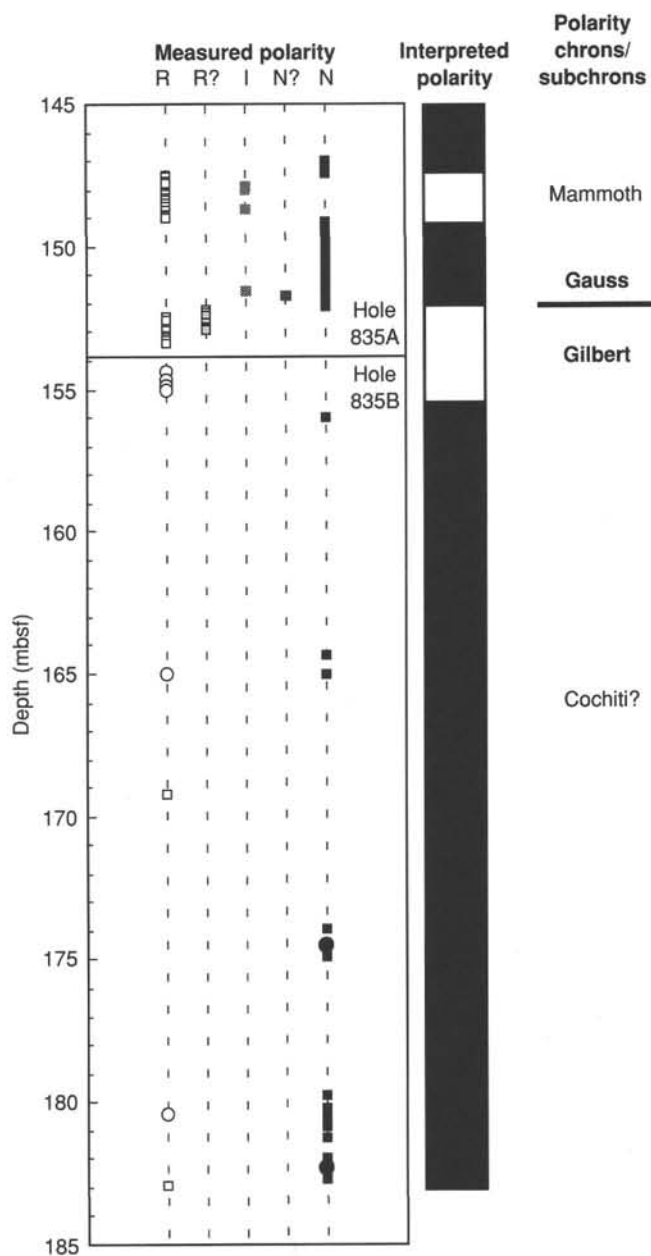


Figure 31. Magnetic polarities of Hole 835B, including data from the bottom of Hole 835A. Black bars indicate normal polarity, whereas white areas show reversed polarity; shades of gray indicate R? (probably reversed), I (indeterminate), and N? (probably normal) polarity, respectively; circles are minicores individually investigated on spinner magnetometer up to 70–100 mT AF, whereas squares and bars are pass-through cryogenic magnetometer results demagnetized to 15-mT AF. Uppermost measurements from Hole 835B (the reversed group between 154 and 155 mbsf) are sedimentary rock samples, the rest below are from basalts. Reversed basalt samples below 165 mbsf are probably from overturned pillows rather than being a result of magnetic field reversals.

**Table 7. Magnetic polarity of Hole 835B basalts.**

Core, section interval (cm)	Depth (mbsf)	N/R
135-835B-		
3R-1, 62-74	154.92	R
3R-3, 21-31	156.01	N
4R-1, 32-36	164.31	N
4R-1, 97-108	164.97	N
5R-1, 19-24	169.19	R
6R-1, 21-30	173.91	N
6R-1, 80-91	174.50	N
6R-1, 119-131	174.84	N
7R-1, 103-127	179.73	N
7R-2, 2-27	180.22	N
7R-2, 33-53	180.53	N
7R-2, 57-67	180.77	N
7R-2, 69-88	180.89	N
7R-2, 107-129	181.27	N
7R-3, 26-34	181.96	N
7R-3, 52-68	182.22	N
7R-3, 90-100	182.60	N
7R-3, 103-118	182.73	N
7R-3, 125-133	182.95	N

Notes: N = normal polarity and R = reversed polarity.

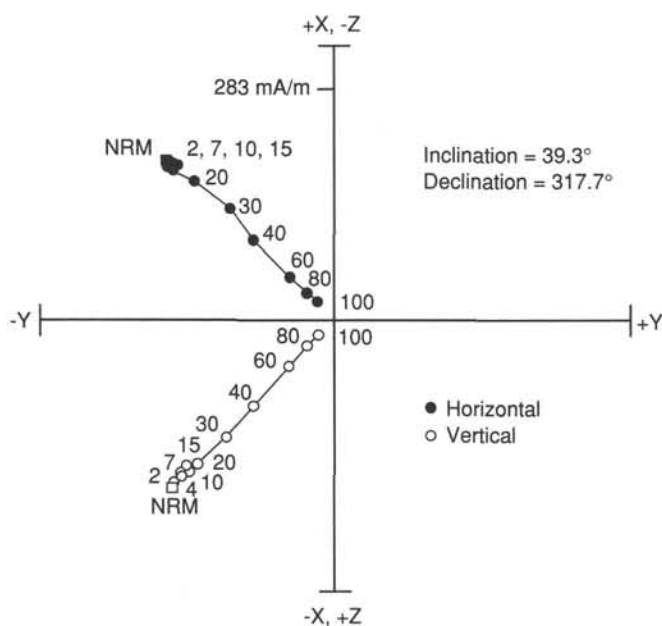


Figure 32. Orthogonal vector plot of a sediment sample from Hole 835B (Sample 135-835B-3R-1, 68-70 cm). The sample clearly shows a reverse polarity, opposite that of the basalts immediately below.

In Hole 835A, ammonia and phosphate determinations were also conducted using colorimetric methods.

### Major Components

In Hole 835A, the concentration-depth profiles of the dissolved major constituents (chloride, sodium, calcium, magnesium, potassium, and sulfate) are characterized by fairly uniform values from the mud line to the bottom of the sedimentary column (Fig. 35). This result is completely comparable with that obtained in Hole 834A and is consistent with the constant high porosity values and the low downhole temperature gradients (see "Physical

Properties" section, this chapter). As mentioned for Hole 834A (see "Site 834" chapter, this volume), Hole 835A was probably drilled in the vicinity of a downwelling flow of bottom seawater recharging a basement aquifer.

### Ammonia and Phosphate

Phosphate and ammonia are metabolic products of the decomposition of organic matter. Their downhole distribution is shown in Figure 35.

The concentration gradients observed above and below the  $\text{NH}_4$  maximum (e.g., 62  $\mu\text{M}$ , at 53.5 mbsf) and  $\text{PO}_4$  minimum (e.g., 1.5  $\mu\text{M}$ , at 34 mbsf) should be understood in terms of both diffusive exchange and reaction rates. However, the diagenetic uptake of phosphate into the sedimentary mineral phases must have been previously associated with the release of phosphate in the uppermost part of Hole 835A. Under this condition, the concentration-depth profile of the dissolved  $\text{PO}_4$  could approximate the dashed line drawn in Figure 35. Indeed, the release of phosphate by the degradation of organic matter results in an accumulation of this ion in the pore water in excess of the seawater values (approximately 2  $\mu\text{M}$ ). Because it is preferentially released during organic matter degradation, the phosphate maximum must occur at a shallower depth than the  $\text{NH}_4$  maximum (Gieskes, 1983). Nevertheless, it is apparent that the values of the dissolved ammonia and phosphate concentrations are very low and are consistent with the almost straight sulfate concentration gradient in Hole 835A. Under this condition, the low production of ammonia could derive from processes involving anaerobic respiration (carbonate reduction) or from fermentation (Claypool and Kaplan, 1974). These processes could be consistent with the high  $\text{CO}_2$  gas level observed in Section 135-835A-6R-5. However, alkalinity does not increase and so, simultaneously, carbonate precipitation must be involved. Finally, the decrease in  $\text{NH}_4$  below 53.5 mbsf could be related to ion exchange reactions in clays (Rosenfeld, 1981; Von Breyman and Suess, 1988).

### Silica, Strontium, and Manganese

The values of the dissolved silica and strontium concentrations at Site 835 are comparable with those obtained at Site 834 (Fig. 35). The slight increase in silica and strontium with depth at Site 835 are causally related to the same chemical processes as described for Site 834 involving ash layer leaching and carbonate recrystallization, respectively.

The manganese concentration-depth profile at Site 835 (Fig. 35) shows an almost linear increase with depth, from the mud line to 110.5 mbsf, below which a linear decrease is observed. The Mn maximum reaches a value of about 134.2  $\mu\text{M}$  at 110.5 mbsf, and implies a release of Mn from solid phases. The linear gradients observed above and below this level suggest that the molecular diffusion processes reached a steady state in Hole 835A.

### Conclusion

The features of the interstitial water chemistry data obtained from sediments at Hole 835A are similar to those from Hole 834A, with little or no concentration gradients. These data suggest an open system for seawater circulation.

### ORGANIC GEOCHEMISTRY

Shipboard organic geochemical analysis of samples from Hole 835A consisted of 14 determinations of volatile hydrocarbons in sediments using the Carle gas chromatograph; 28 determinations of total nitrogen, carbon, and sulfur using the Carlo Erba NCS Analyzer; and 71 determinations of total inorganic carbon using the Coulometrics 5011 coulometer equipped with a System 140 carbonate/carbon analyzer. Details of the analytical procedures used are outlined in the "Organic Geochemistry" section of the

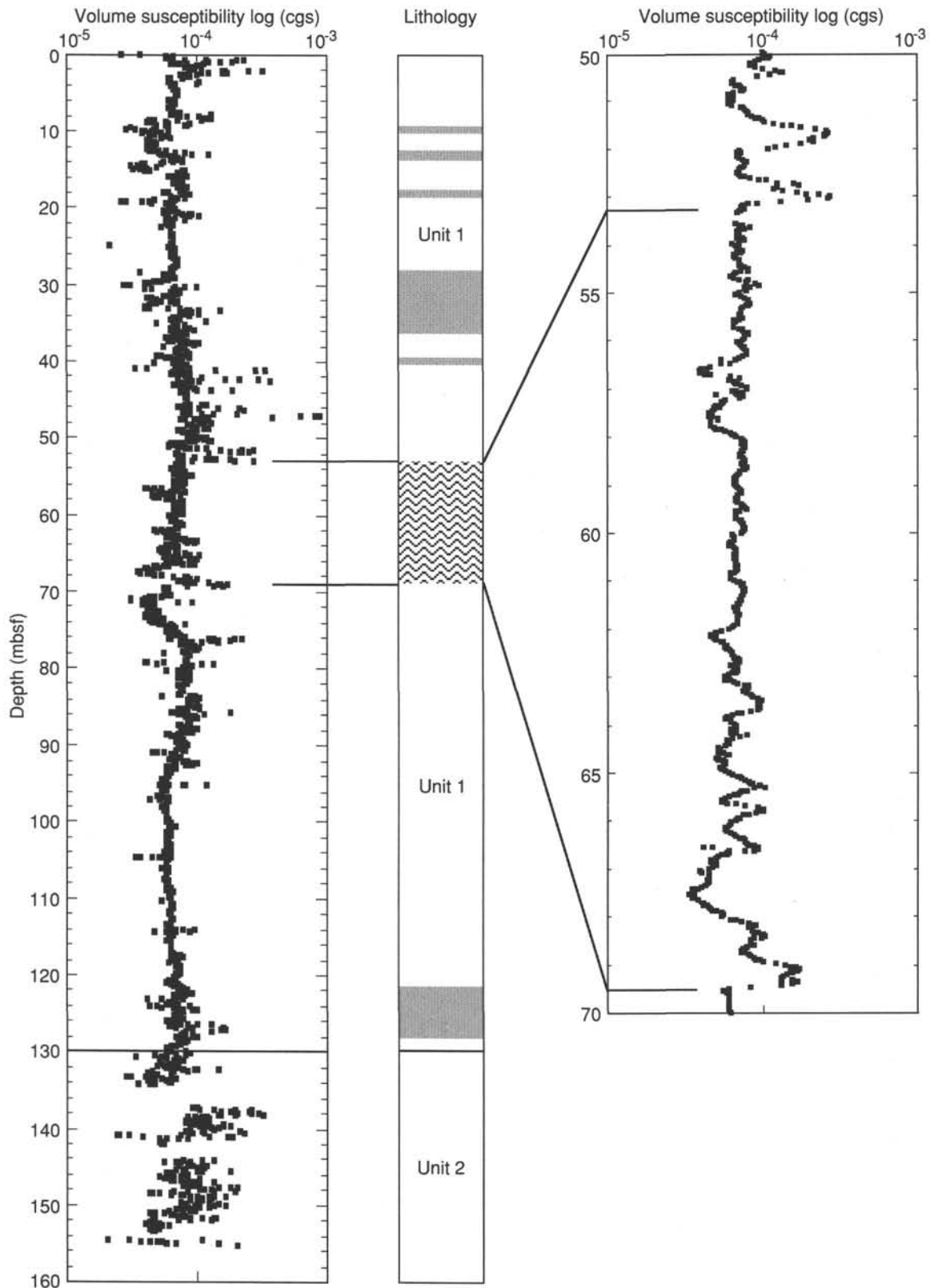


Figure 33. Volume magnetic susceptibility, Hole 835A. Columns at left and right show susceptibility values, plotted on a logarithmic scale. Middle column denotes lithostratigraphy of Hole 835A. Gray areas indicate sections of core thought to contain slumped (mud-clast conglomerates) material according to lithostratigraphy, whereas wavy lines denote core from an allochthonous sediment block, suggested by biostratigraphy. Column at right is an enlargement of the susceptibility plot for the interval from 50 to 70 mbsf that shows possible correlations between susceptibility spikes and the top and bottom of the allochthonous section.

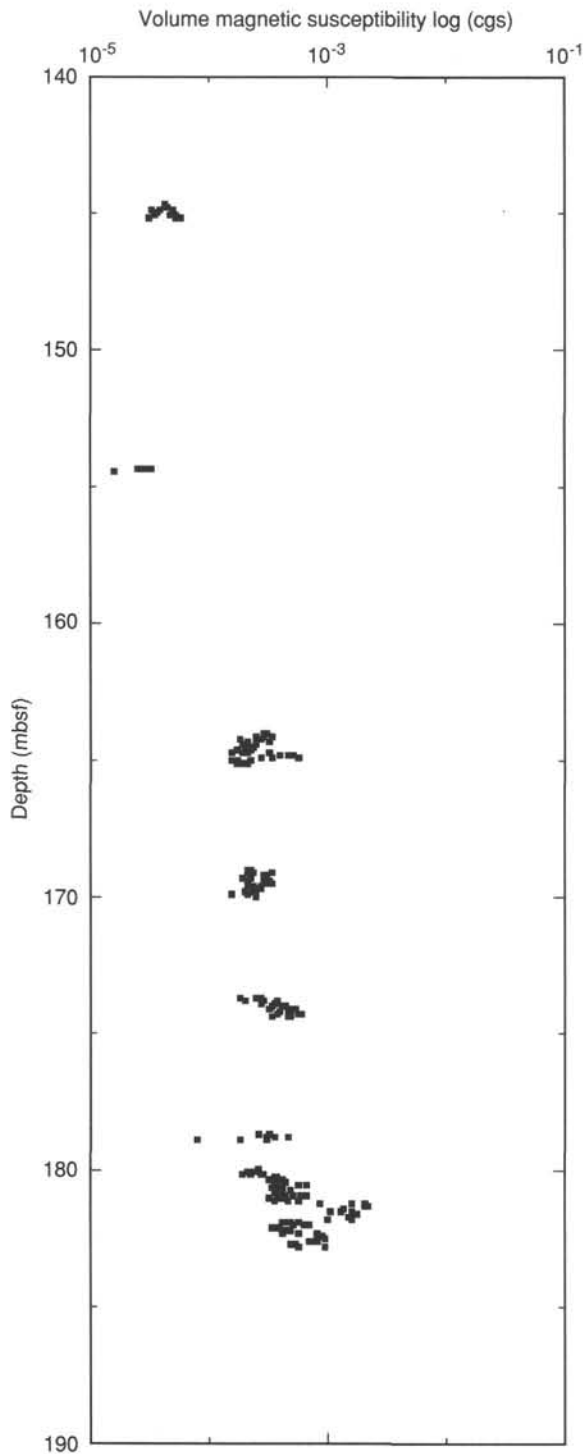


Figure 34. Volume magnetic susceptibility, Hole 835B. All values are from cores containing basalts (logarithmic scale).

“Explanatory Notes” chapter (this volume) and are described in detail by Emeis and Kvenvolden (1986).

The volatile hydrocarbon gases were obtained from the bulk sediment using the head-space sampling technique and were routinely monitored for methane, ethane, and propane. One sample was taken from each of the first 16 cores with the exception of Cores 5 and 15. Methane concentrations in all the samples were between 2 and 3 ppm, which is very low and at the laboratory

Table 8. APC core orientations, Hole 835A.

Core no.	Camera no.	Compass	Inclination		
			Direction	Drift	Declination
135-835A-					
3H	3209	B	N60°E	1°	320°
4H	3209	B	45°	1°	295°
5H	3250	A	8°	1°	156°
6H	3250	A	11°	1°	148°
7H	3209	A	5°	1°	237°
8H	3209	A	10°	1°	156°
9H	3250	B	20°	1°	107°
10H	3250	B	34°	1°	20°
11H	3209	A	0°	1°	255°
12H	3209	A	10°	1°	285°
13H	3250	B	← No data →		
14H	3250	B	← No data →		
15H	3209	A	30°	1°	144°
16H	3209	A	20°	1°	110°
17H	3209	A	350°	1.7°	355°

Notes: Inclination is the off-vertical angle of the core. Drift and direction are the dip and dip direction measured clockwise from north of a plane perpendicular to the core axis. Declination is the angle between the double line on the core liner and magnetic north (measured clockwise).

background level. Ethane and propane were not detected. A positive gas pressure was observed in Sections 135-835A-9H-5 and -9H-6 when brought to the surface. Analysis of this gas by the Carle gas chromatograph indicated that it was not composed of hydrocarbons. Unfortunately, the NGA instrument was not working at the time and therefore the identity of the gas is unknown. It is suspected that the gas was either air or carbon dioxide. The extremely low concentration of methane indicates that methanogenesis is not occurring in these sediments. As was the case at Site 834, sulfate levels remain at the same level as that of seawater throughout this hole (see “Inorganic Geochemistry” section, this chapter), and, consequently, at no time were conditions favorable for methanogenesis. Another contributing factor could be that the very low levels of organic carbon (see below) in these sediments were not enough to sustain microbial activity.

Determinations of inorganic carbon (IC) contents were performed on the samples used for physical properties and on additional samples selected by the sedimentologists. Percentages of CaCO<sub>3</sub> were calculated according to the equation:

$$\text{CaCO}_3 = \text{IC} \cdot 8.334.$$

This equation assumes that all the carbonate is present as calcite. The data from these analyses are presented in Table 10. Carbonate values range from <8.5% to 84.3%. There is less variation in the carbonate values than at Site 834. The very low value at a depth of 47.05 mbsf corresponds to an ash layer. The low values below 137 m are associated with the increased contribution of volcanoclastic material to these sediments. This is discussed in more detail and related to the lithologic units in the “Lithostratigraphy” section (this chapter).

Also shown in Table 10 are the percentages of total carbon and sulfur for the 28 samples measured. The nitrogen content was also measured, but nitrogen was not detected in any of the samples analyzed. Total organic carbon (TOC) is defined here as the difference between the total carbon and the inorganic carbon values. The sediments from Site 835 have organic carbon contents between 0.4% and 0.35% and hence were considered too low for analysis by the Rock-Eval instrument. The TOC content shows no correlation with depth or with percentage of carbonate. Sulfur was only detected in the lowermost four samples analyzed. As these

Table 9. Interstitial water chemistry data, Hole 835A.

Core, section, interval (cm)	Depth (mbsf)	pH	Alkalinity (mM)	Salinity	Ca <sup>2+</sup> (mM)	Mg <sup>2+</sup> (1) (mM)	Mg <sup>2+</sup> (2) (mM)	K <sup>+</sup> (mM)	Cl <sup>-</sup> (mM)	SO <sub>4</sub> <sup>2-</sup> (mM)	NH <sub>4</sub> <sup>+</sup> (μM)	Si <sup>4+</sup> (μM)	Sr <sup>2+</sup> (μM)	Mn (μM)	PO <sub>4</sub> <sup>3-</sup> (μM)	Na <sup>+</sup> (1) (μM)	Na <sup>+</sup> (2) (mM)
135-835A-																	
1H-4, 140-150	6.0	7.61	3.107	35.4	10.5	51.6	49.2	11.2	550	27.9	9	317	96.8	24.5	2.86	471	476
2H-4, 140-150	15.5	7.51	2.56	35.4	10.9	51.7	50.8	11.2	554	28.1	11	354	102.8	40.7	2.71	474	475
3H-4, 140-150	25.0	7.62	2.241	35.6	10.8	52.5	52.4	11.6	553	28.4	19	312	101.8	49.1	2.4	471	471
4H-4, 140-150	34.0	7.68	2.274	35.8	11.1	52	51.2	11.1	554	27.7	26	317	98.7	56.7	1.49	472	474
6H-4, 140-150	53.5	7.59	2.271	35.9	11.3	51.1	50.6	11.3	552	27.1	62	342	104.2	84.2	1.95	470	471
8H-4, 140-150	72.5	7.5	2.654	35.6	11.7	52.1	49.8	10.7	553	26.8	39	342	110.7	102.2	2.25	468	473
10H-4, 140-150	91.5	7.5	2.7	35.6	12.3	50.5	50.8	10.8	551	27.1	34	354	122.1	108.7	3.02	469	468
12H-4, 140-150	110.5	7.13	2.757	35.6	12.9	51.7	51.6	10.3	551	26.4	24	371	123.9	134.2	3.4	464	465
14H-4, 140-150	129.5	7.52	2.553	35.3	12.7	51.7	50.4	10.5	551	26.7	19	388	121.8	100.2	3.47	465	468
16H-6, 140-150	148.5	7.58	2.4	35.5	11.3	49.3	49.2	11.4	548	26.7	19	438	118.4	33.1	3.47	469	469

samples have high volcanoclastic contents, it is reasonable to assume that, as for Hole 834, the sulfur is inorganic and probably associated with minerals (sulfides) of igneous origin. Sulfur was not detected in the ash layer at 47.05 mbsf depth.

## IGNEOUS PETROLOGY

### Introduction

Site 835 is situated in a basin that was expected to be intermediate in age between the oldest sampled basement in the Lau Basin (Site 834) and the neovolcanic zone of the CLSC. The intent was to determine accurately the age of the igneous basement in this region and to compare magma chemistry at Site 835 with the older and younger crustal rocks. The site is on crust that Hawkins and Melchior (1985) had proposed to be intermediate in composition between arc and N-MORB.

Two holes were drilled at Site 835; basement was intersected at 155.1 mbsf in Hole 835A and 155.5 mbsf in Hole 835B. Hole 835A was ended upon recovering igneous rock and Hole 835B was drilled to a depth of 183.0 mbsf. We recovered 8.7 m of basaltic rock from the 27.5 m of basement drilled at Hole 835B (32% recovery; Fig. 36). Paleontological dating of the overlying sediments indicates a range in ages extending as far back as 3.5 Ma (see "Biostratigraphy" section, this chapter).

A single lithologic unit of sparsely to highly phyrlic olivine-clinopyroxene-plagioclase basalt was recovered at Site 835. Despite considerable textural variability in this unit, the mineralogical and geochemical characteristics show only minor variation, so the designation of a single unit is valid. Plagioclase and clinopyroxene are present in approximately a 2:1 ratio and are accompanied by subordinate olivine. The textures range from slightly to highly phyrlic to nearly diabasic, with a general increase in degree of crystallinity downcore. Vesicle content ranges from 8% to 35%, with no systematic variation throughout the unit. In many of the larger vesicles, there are total to partial infillings of dark, frothy, highly vesicular basalt, similar to those in many of the Site 834 basalts. The dark color in these segregation vesicles results from both the very fine-grained or glassy nature of the material and the abundance of fine-grained opaque minerals.

The thicknesses of individual cooling units have been inferred by counting glassy and microlitic zones for every meter of core and calculating a core average (see "Igneous Petrology" section, "Site 834" chapter, this volume). These results indicate that cooling unit thicknesses increase downward in this unit (Fig. 37). As might be expected, core recovery appears to be linked with cooling unit thickness; both increase with depth to a maximum in Core 135-835B-7R (76% recovery).

The finer grained to cryptocrystalline basalts are generally very fresh. Glass margins are partially palagonitized, and alteration halos are common adjacent to fractures and margins. The more diabasic rocks are somewhat more altered than the finer grained rocks. Well-defined alteration fronts in the diabasic rocks

of Core 135-835B-7R separate more altered, yellow-brown to tan-colored rocks from less altered, blue-gray rocks. In the latter, vesicles are lined with blue-white zeolites and manganese oxides, whereas in the more altered regions, the vesicle infills are greenish. The yellow hue of the more altered rocks results from oxidation and replacement of zeolites and mesostasis to clays, iron oxyhydroxides, and manganese oxides. Primary magmatic sulfides occur as linings in vesicles of Core 135-835B-5R.

### Petrography

The range of textures in this unit grades through several types, and classification has proved difficult. End-member textures are porphyritic and diabasic (Figs. 38 and 39, respectively). All of the rocks have highly seriate porphyritic textures. The phyrlic samples contain 10%–25% euhedral phenocrysts set in a fine-grained to cryptocrystalline groundmass. The near-diabasic samples comprise >60% interlocking crystals, and there is no clear distinction between groundmass and phenocrysts. The textural gradation between the two end members is related to increasing extent of crystal development in the matrix. Many samples contain plagioclase-clinopyroxene glomerocrysts set between larger, isolated phenocrysts. As the crystal size in these glomeroporphyritic clusters increases, the distinction between groundmass and phenocrysts becomes less pronounced. The glomeroporphyritic clusters consist of several euhedral plagioclase grains radiating away from an anhedral, equant clinopyroxene core (Fig. 40A). As the glomeroporphyritic clusters become increasingly intergrown, a network of interlocking glomerocrysts surrounded by a cryptocrystalline groundmass develops (Fig. 40B). Ultimately, the distinction between phenocrysts and interlocking glomerocrysts cannot be made and the intergranular to intersertal diabasic texture predominates.

In the following discussion, phenocrysts and groundmass phases will be discussed collectively as there is a continuous size gradation in the phases and the distinction is arbitrary in many samples. Table 11 summarizes the modal analyses of the samples.

Euhedral plagioclase grains (<2 mm) occur as both isolated grains and in glomeroporphyritic clusters of varying grain size. Oscillatory zoning is common in plagioclase grains of all sizes and some have distinct, narrow sodic rims. Optical properties suggest relatively calcic core compositions of >An<sub>65</sub>. Melt inclusions occur in some of the larger plagioclase grains. Small, interstitial elongate microlites are randomly oriented and often show swallow-tail terminations (Fig. 41).

Clinopyroxene ranges in grain sizes, from acicular, plumose sheaves, to small (<0.6 mm), equant, interstitial grains, to large (generally <1.2 mm but up to 4 mm), euhedral, tabular, often subophitic crystals. Several interesting textures are exhibited by the clinopyroxenes. The smallest grains are feathery and form fine intergrowths with microlitic plagioclase. Many of the clinopyroxene grains exhibit wavy and undulose extinction and curved crystal outlines suggestive of rapid growth during quenching.

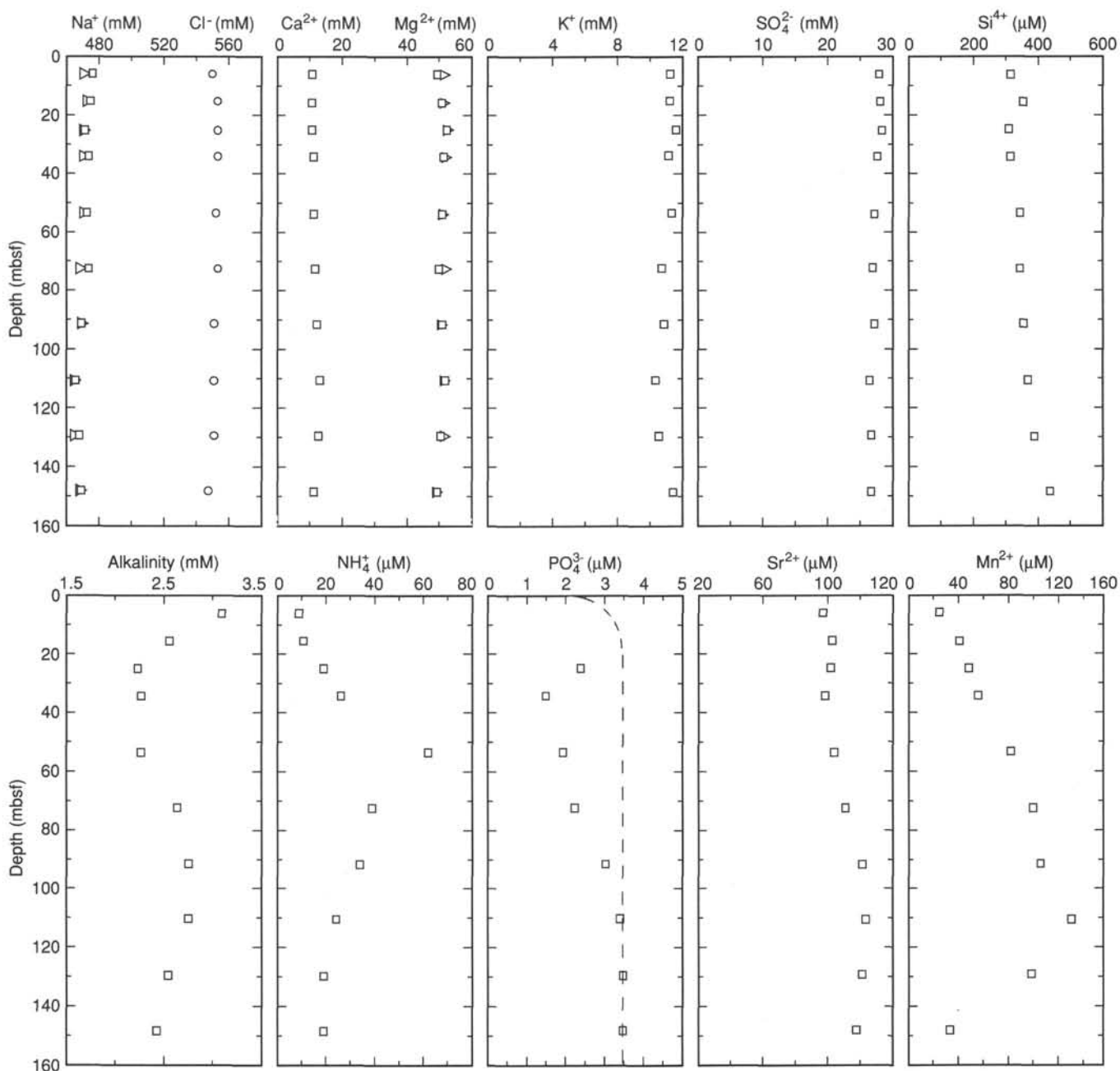


Figure 35. Concentration vs. depth profiles for chloride and sodium, calcium and magnesium, potassium, sulfate, alkalinity, ammonia, phosphate, silica, strontium, and manganese, Hole 835A.

Sector zoning was observed in some of the larger clinopyroxene grains. Similar features were observed in the basalts collected at Site 834 (see "Site 834" site chapter, this volume) and are illustrated in that section.

Olivine is a relatively minor phase (<2.5%) and occurs as isolated, subhedral to anhedral, equant grains. Iddingsite has developed along the rims and within the fractures of most grains, suggesting minor degrees of alteration.

Magnetite is the only oxide in the Site 835 basalts. In one sample (135-835B-6R-1, 111–114 cm, Piece 15), large (up to 0.2 mm), equant, cruciform, and skeletal magnetite grains constitute nearly 5% of the rock. Elsewhere, extremely fine-grained (<0.005 mm) magnetite grains are scattered throughout the cryptocrystalline groundmass material. A bimodal size distribution of

magnetite grains characterizes some sections; both equant, isolated grains, and a fine-grained groundmass "dust" are present.

A large part (25–75%) of most samples is cryptocrystalline mesostasis. Samples with porphyritic texture have more mesostasis than the diabases, which have relatively little interstitial space. This cryptocrystalline material has been variously replaced by very fine-grained, greenish brownish clays. Two thin sections (Samples 135-835B-7R-3, 137–140 cm, Piece 14, and -6R-1, 32–37 cm, Piece 7) have rims of pale brown glass. The texture becomes increasingly variolitic toward the interior. Near the glassy rims, fine glassy selvages have been preserved in some of the vesicles.

These rocks are highly vesicular, and vesicle content varies considerably (8%–35%). There is a rough increase in vesicularity

**Table 10. Concentrations of inorganic and organic carbon and total sulfur, Hole 835A.**

Core, section, interval (cm)	Depth (mbsf)	Total carbon (%)	Inorganic carbon (%)	Organic carbon (%)	CaCO <sub>3</sub> (%)	S (%)	OrgC/S
135-835A-							
1H-5, 30-31	6.30	7.32	7.07	0.25	58.9		
2H-2, 69-70	11.69	8.38	8.23	0.15	68.6		
2H-4, 50-51	14.50	7.83	7.63	0.20	63.6		
2H-4, 97-98	14.97	8.48	8.32	0.16	69.3		
2H-6, 72-73	17.72		7.80		65.0		
3H-2, 78-80	21.28	7.24	7.20	0.04	60.0		
3H-4, 62-63	24.12		7.39		61.6		
3H-6, 72-73	27.22		7.49		62.4		
4H-1, 91-92	29.41		8.74		72.8		
4H-2, 73-74	30.73	8.99	8.94	0.05	74.5		
4H-4, 72-73	33.72		6.99		58.2		
4H-4, 79-80	33.79		8.02		66.8		
4H-5, 68-69	35.18		8.01		66.7		
4H-7, 60-61	38.10		7.20		60.0		
5H-1, 105-106	39.05		7.15		59.6		
5H-2, 104-105	40.54	7.72	7.54	0.18	62.8		
5H-4, 77-78	43.27		7.28		60.6		
5H-5, 130-132	45.30		7.35		61.2		
5H-6, 97-98	46.47		8.06		67.1		
5H-7, 5-6	47.05	1.13	1.02	0.11	8.5		
6H-1, 135-136	48.85		6.24		52.0		
6H-2, 71-72	49.71	6.67	6.33	0.34	52.7		
6H-4, 44-45	52.44		6.84		57.0		
6H-4, 84-84	52.84		4.97		41.4		
6H-6, 74-75	55.74		8.41		70.1		
6H-7, 19-20	56.69	7.56	7.41	0.15	61.7		
7H-1, 128-129	58.28		8.52		71.0		
7H-2, 93-94	59.43	8.43	8.16	0.27	68.0		
7H-4, 77-78	62.27		8.64		72.0		
7H-5, 43-44	63.43		7.42		61.8		
7H-6, 74-75	65.24		7.85		65.4		
7H-6, 77-78	65.27		7.14		59.5		
7H-7, 54-55	66.54	7.49	7.32	0.17	61.0		
8H-2, 47-48	68.47		6.94		57.8		
8H-2, 72-73	68.72	7.67	7.38	0.29	61.5		
8H-4, 25-26	71.25		10.12		84.3		
8H-4, 78-79	71.78		8.78		73.1		
8H-6, 99-100	74.99		7.39		61.6		
8H-7, 30-31	75.80		7.82		65.1		
9H-2, 78-79	78.28	7.87	7.60	0.27	63.3		
9H-3, 128-129	80.28		9.56		79.6		
9H-3, 142-143	80.42		8.04		67.0		
9H-4, 70-71	81.20		7.66		63.8		
9H-5, 31-32	82.31		8.00		66.6		
9H-7, 14-15	85.14		7.58		63.1		
10H-2, 66-67	87.66	8.15	7.80	0.35	65.0		
10H-4, 67-68	90.67	8.13	7.94	0.19	66.1		
10H-6, 68-69	93.68		7.48		62.3		
11H-2, 70-71	97.20		7.49		62.4		
11H-4, 81-82	100.31		7.37		61.4		
11H-6, 70-71	103.20	7.50	7.33	0.17	61.1		
12H-2, 69-70	106.69	7.51	7.27	0.24	60.6		
12H-4, 69-70	109.69	7.54	7.32	0.22	61.0		
12H-6, 69-70	112.69	7.53	7.31	0.22	60.9		
13H-2, 69-70	116.19		7.36		61.3		
13H-4, 68-69	119.18		8.85		73.7		
13H-6, 91-92	122.41	6.71	6.52	0.19	54.3		
14H-3, 55-56	127.05		6.76		56.3		
14H-6, 47-48	131.47	4.67	4.50	0.17	37.5		
15H-1, 47-48	133.47		6.97		58.1		
15H-2, 79-80	135.09		4.97		41.4		
15H-3, 61-62	136.23	6.53	6.31	0.22	52.6		
15H-4, 68-69	137.80		4.12		34.3		
15H-6, 106-107	141.18	5.79	5.61	0.18	46.7		
16H-1, 43-45	142.93		6.41		53.4		
16H-2, 69-71	144.69	5.09	4.94	0.15	41.2	0.41	0.36
16H-4, 76-78	147.76	3.36	3.23	0.13	26.9	1.00	0.13
17H-1, 74-75	152.74	3.93	3.79	0.14	31.6	1.23	0.11
18X-1, 24-25	154.74	1.33	1.16	0.17	9.7	1.72	0.10

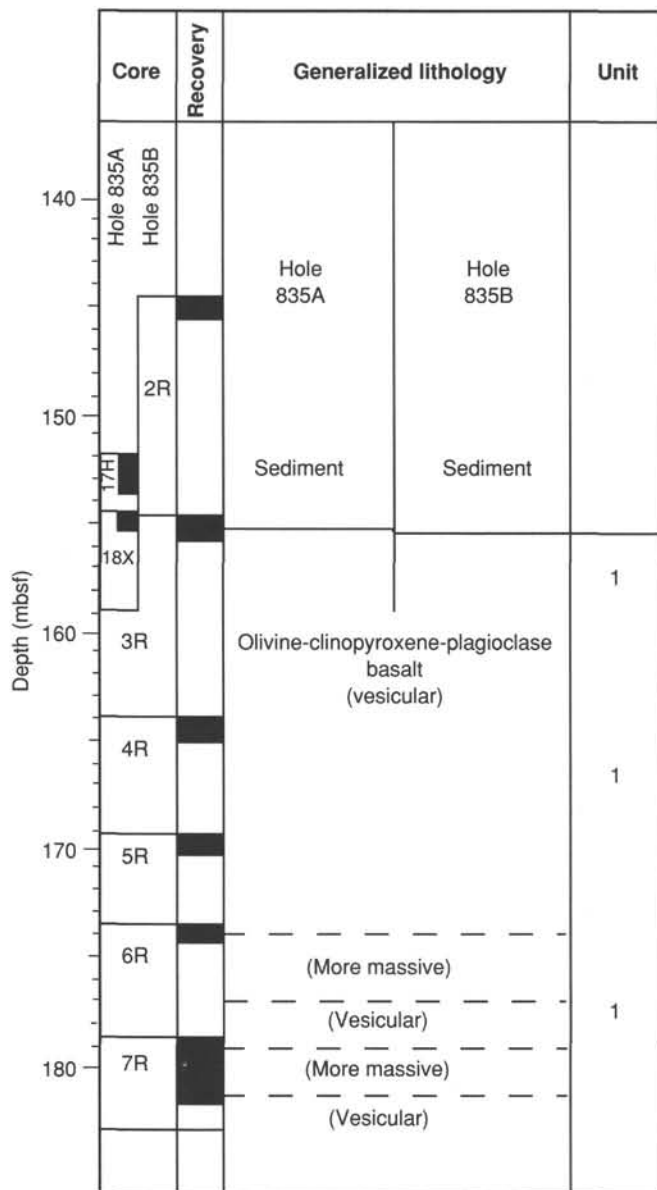


Figure 36. Lithologic variations with depth, Holes 835A and 835B. Black bars indicate core recovery.

with increasing percentage of mesostasis in the rock, with the exception of one part of Core 135-835B-7R. Vesicle distribution tends to occur in two distinct size populations: one <0.1 mm in diameter and the other >0.5 mm. The largest vesicles are irregularly shaped voids that appear to have formed by the coalescence of several smaller vesicles. The fine-scale vesicles are abundant and impart a high porosity to the rock.

Vesicles show various degrees of infilling, averaging about 20% of the vesicle volume. The infilling material is typically a dark greenish brown cryptocrystalline clay, very similar in appearance to the clay replacement product resulting from alteration of the mesostasis. The more crystalline samples show more extensive infilling of vesicles.

As in some of the vesicular units in the Site 834 basalts, the largest vesicles (up to 4 mm across) are often filled with a very highly vesicular (up to 80%), dark brown-black, quench-textured, sometimes glassy basalt. Acicular crystallites of plagioclase and

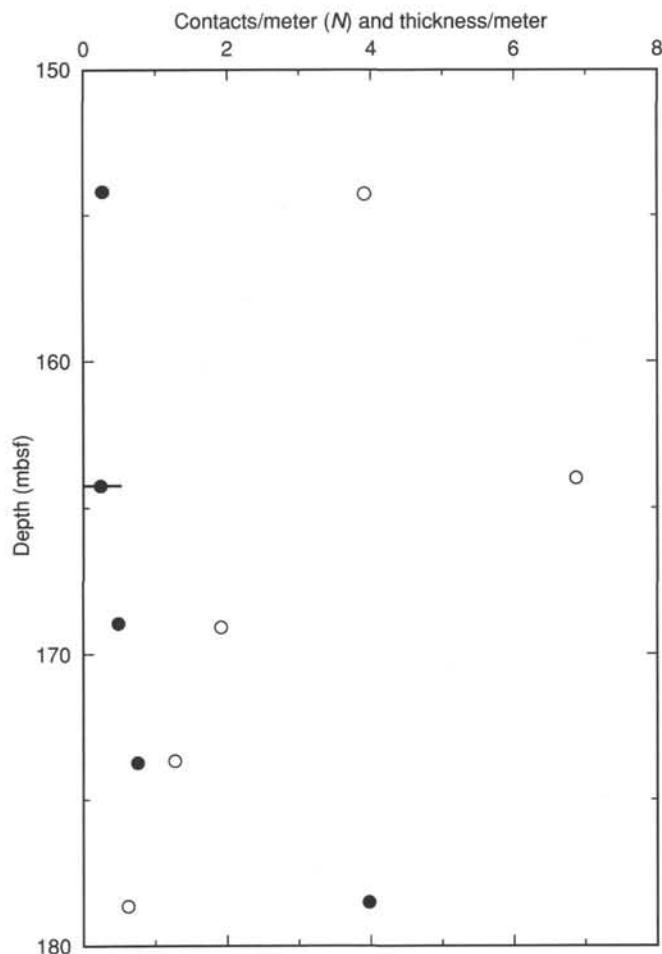


Figure 37. Contacts per meter of core recovered and average thickness (m) between cooling units in recovered core, Hole 835B. Filled circles = average thickness (m) and open circles = contacts/m recovered.

clinopyroxene are sometimes present, and small magnetite grains are largely responsible for the dark color. These segregation vesicles (Sato, 1978) grade sharply into the host rock, and in some instances plagioclase microlites of the host are aligned along the edge of the vesicle.

### Alteration

Macroscopic evidence of alteration effects is seen in several prominent alteration fronts crossing the rock and producing a change in color from blue-gray to greenish brown. One of the rare fractures is filled by a thin (<1 mm in width), dark green vein in Core 135-835B-7R-2, 115–120 cm, Piece 8. In contrast to the basalts at Site 834, where interbedded sediment layers provided a source of calcium, no calcite veins were observed in the Site 835 basalts.

Microscopically, the alteration of this unit is manifested by replacement of the fine-grained mesostasis with cryptocrystalline, green brown clays. The degree of alteration varies with the amount of interstitial mesostasis present in the rock and is nearly complete in the coarser grained samples. The more fine-grained rocks show only minor replacement of the mesostasis (Fig. 42).

The mineral phases are typically very fresh, with the exception of rare olivine grains with iddingsite development along fractures and rims. In Cores 135-835B-7R-2, 89–93 cm, Piece 5, and -7R-3, 55–58 cm, Piece 7B, an acicular, green, highly pleochroic mineral with an extinction angle of about 10° replaces olivine and is

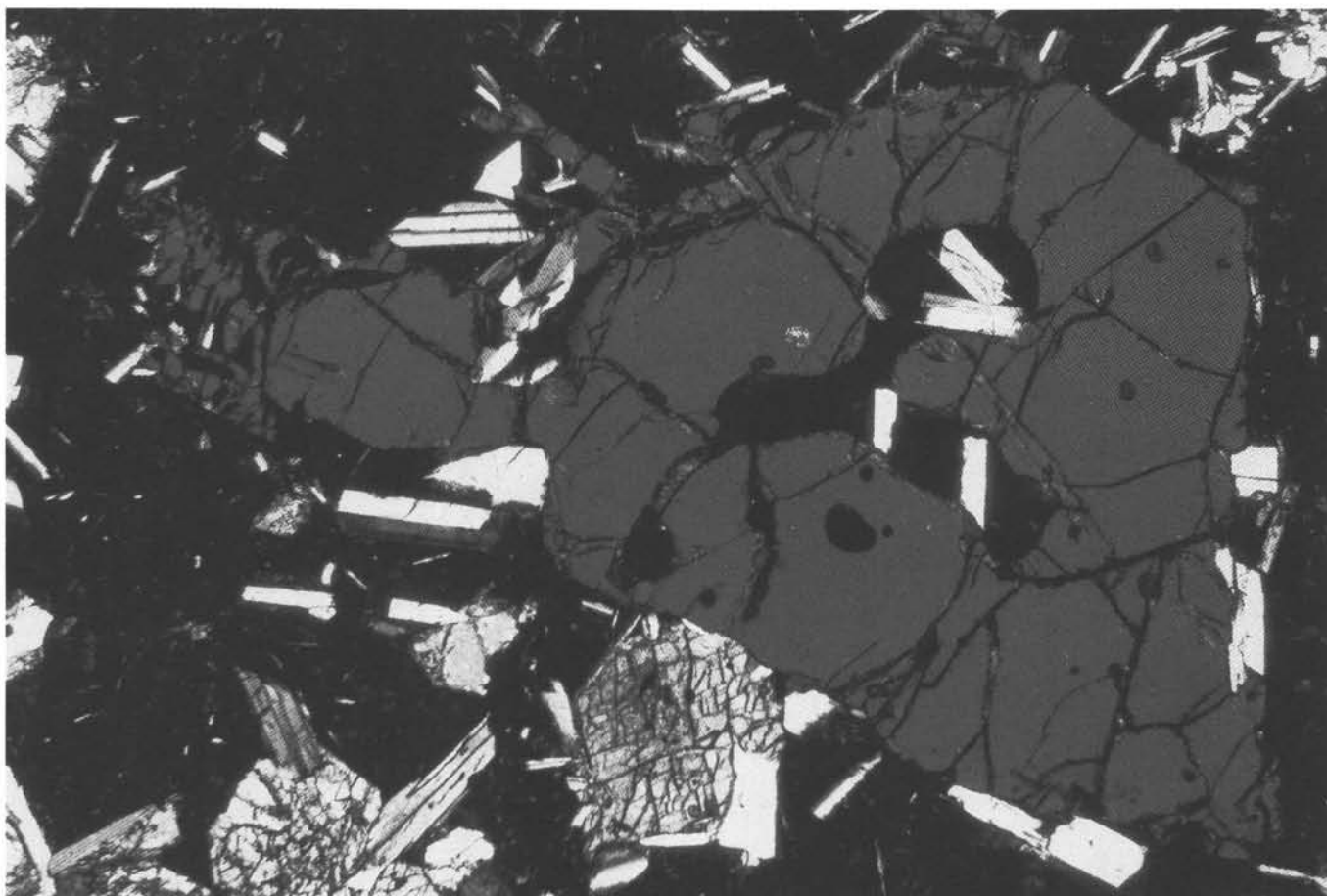


Figure 38. Photomicrograph of skeletal olivine phenocryst with associated clinopyroxene and plagioclase phenocrysts and microphenocrysts, in very fine-grained groundmass; Sample 135-835-7R-3, 137–140 cm, Piece 14; field of view = 3 mm, crossed polarized light.

probably actinolite. The larger plagioclase grains in a few samples show incipient alteration along fractures and margins. Where glassy linings of vesicles are inferred to have existed, palagonite occurs and is covered by a very thin layer of zeolites (Fig. 43).

Both the macroscopic and the microscopic features of this unit suggest that the dominant alteration processes have been at relatively low temperatures. The presence of actinolite may be the result of hydrous near-solidus autometamorphism.

### Igneous Geochemistry

The geochemical signature of the basalts from Site 835 is important because this site lies between Site 834 in the western Lau Basin and the present-day CLSC. If there has been a progressive change in the geochemical signature of the basalts from “arclike” to “MORB-like” as the Lau Basin has evolved, the Site 835 basalts should be intermediate to the Site 834 basalts and those erupted along the present-day spreading center.

Six representative samples from the igneous section at Site 835 were analyzed by X-ray fluorescence (XRF) spectrometry. Table 12 shows the major and trace element data and the average of the six analyses.

The similarity in composition of all six samples supports the assignment of all of the Site 835 basalts to a single lithologic unit. The geochemical homogeneity of these texturally variable rocks suggests that the differences in crystal size and vesicle content result from different cooling rates and degrees of degassing of a single magma. Although it is a quartz-normative tholeiitic basalt,

the material recovered at Site 835 is relatively unfractionated with a Mg number of 60 ( $Mg\# = [Mg/(Mg + Fe)] \cdot 100$ ).  $Fe^{3+}/Fe^{2+}$  was set at 0.2 for all calculations. Relatively low values for loss on ignition (LOI),  $K_2O$ , and  $Na_2O$  confirm petrographic evidence that this unit has experienced only minor alteration.

The major element compositions of the Site 835 basalts are broadly similar to those of basalts produced at mid-ocean-ridge spreading centers. Subtle differences do exist;  $TiO_2$ ,  $FeO_{total}$ , and  $Na_2O$  are somewhat lower than is observed in typical MORB, whereas  $CaO$  and  $Al_2O_3$  are higher. Similar signatures have been observed in many other backarc basalts (e.g., Hawkins and Melchior, 1985). In contrast, arc tholeiites from the nearby Tongan volcanos show significantly greater depletions in relatively incompatible constituents such as  $TiO_2$  and  $Na_2O$  (Ewart and Hawkesworth, 1987).

If the source of Lau Basin basalts has changed with time and basin evolution, that change is more likely to be manifested in the incompatible trace elements than in the major elements. Figure 44 presents the incompatible trace element data normalized to N-MORB. Trace elements are arranged in order of decreasing incompatibility during melting of a typical four-phase lherzolite. Figure 44A compares the data from Site 835 to average values for the Tonga Arc (Ewart and Hawkesworth, 1987) and range of values for the modern Lau Basin. Although the incompatible element signature of both the Site 835 and the more enriched Lau Basin basalts lie between typical MORB (a horizontal line at 1) and Tonga-Kermadec arc values, the two patterns are distinct. Site 835 basalts are enriched in the highly incompatible elements (Rb



Figure 39. Photomicrograph of complex intergrown plagioclase and clinopyroxene with very little interstitial mesostasis; Sample 135-835-7R-2, 89-93 cm, Piece 5; field of view = 3 mm, crossed polarized light.

and Ba) relative to N-MORB and to many Lau Basin basalts (in the case of Ba, the CLSC), but these enrichments are not as pronounced as in the modern Tofua Arc. The mobility of these elements during alteration processes can make the relative enrichments difficult to interpret, but the high Ba/Rb suggests a geochemical signature for the Site 835 basalts more like the arc signature than that of the Lau Basin spreading centers.

The Site 835 basalts are not as depleted in high-field-strength elements (HFSE) as the average Tonga-Kermadec arc lavas, but a striking similarity in pattern shape between the Site 835 basalts and the Tonga-Kermadec average is present. This pattern is characterized by a significant depletion in Zr relative to neighboring elements. The Zr depletion produces Zr/Ti and Zr/Y values that are considerably lower in the Site 835 basalts than either N-MORB or CLSC basalts. The similarity in Zr/Y and Zr/Ti to the average Tonga Arc value suggests derivation of the Site 835 basalts from a mantle relatively more depleted in HFSE, particularly Zr, than that feeding the present-day spreading system.

Figure 44B shows the incompatible element signature of the Site 835 basalt compared with the range of values observed for the basalts and basaltic andesites collected at Site 834. The Site 835 basalts are within the range defined by the Site 834 basalts for the highly incompatible elements, and similar to the most depleted of the Site 834 basalt for the remaining elements measured.

Although there are some subtle differences in trace element signatures, the Site 835 basalts are similar to backarc basin basalts

from Site 834. The HFSE depletions in general, and the Zr depletion in particular, suggest derivation from a mantle more like an arc-tholeiite source than a typical N-MORB source.

## PHYSICAL PROPERTIES

### Introduction

A full suite of standard ODP physical properties measurements were made at Site 835. Index properties on sediments and sedimentary rocks from Holes 835A and 835B were determined by using a pycnometer and balance, and include bulk density, grain density, porosity, water content, and void ratio. Bulk density was also measured using the continuous gamma-ray attenuation porosity evaluator (GRAPE) on full APC cores from Hole 835A. Four representative samples selected from the 38.5 m of basalt recovered from Hole 835B were run through the 2-min GRAPE process to determine bulk densities; these samples were also powdered and the weight and volume of the dried powder determined to give grain density.

Compressional wave velocities were measured on whole cores using the continuous *P*-wave logger and on discrete samples using the Hamilton Frame apparatus. Velocities of unconsolidated sediments that could not be removed from the core liner were measured in only one direction. Velocities were measured in both horizontal and vertical directions when possible in unconsolidated sediments and on most of the consolidated sedimentary rocks and basalts.

**A****B**

Figure 40. **A.** Small clinopyroxene-plagioclase glomerocrysts; typically intermediate in size between groundmass and phenocrysts; field of view = 1.5 mm, crossed polarized light. **B.** Similar to Figure 40A but aggregate is somewhat larger; field of view = 1.5 mm, crossed polarized light (both examples are from Sample 135-835-3R-1, 137–140 cm, Piece 4).

**Table 11. Modal analyses (>1000 point counts) of representative samples from Hole 835B.**

Hole	835B	835B	835B	835B	835B	835B	835B	835B
Core	3R-1	4R-1	6R-1	6R-1	7R-1	7R-2	7R-3	7R-3
Piece	4	18	15	9	11	5	4B	14
Interval (cm)	137-140	112-115	111-114	32-37	44-48	89-93	55-58	137-140
Type	Basaltic	Basaltic	*Diabasic	*Diabasic transitional	Basaltic	*Diabasic	*Diabasic	Basaltic
Depth (mbsf)	155.58	164.95	174.40	173.91	179.06	180.42	181.31	181.96
Phenocrysts:								
Plagioclase	7.0	1.7	0.9	1.5	9.2	16.3	15.0	3.6
Clinopyroxene	5.0	0.9	0.8	0.6	5.0	6.3	6.4	4.4
Olivine	0.8	1.2	0.0	1.2	0.5	0.1	0.1	2.5
Total phenocrysts	12.8	3.8	1.7	3.3	14.7	22.7	21.5	10.5
Vesicles:								
Open vesicles	17.3	18.2	9.0	14.0	16.3	7.0	6.6	6.5
Filled vesicles	1.0	0.0	5.7	0.8	0.7	0.3	3.0	0.0
Total vesicles	18.3	18.2	14.7	14.8	17.0	7.3	9.6	6.5
Groundmass:								
Plagioclase	9.0	20.2	30.8	24.5	8.4	23.3	23.1	7.0
Clinopyroxene	9.9	13.9	23.4	17.5	9.5	17.3	15.9	1.8
Olivine	0.3	0.3	0.6	1.9	0.3	0.0	0.1	0.1
Opagues	1.3	0.9	3.9	1.0	2.2	3.1	3.2	
Mesostasis	48.5	42.7	25.0	37.0	47.8	26.1	26.6	74.1
Total groundmass	69.0	78.0	83.6	81.9	68.2	69.8	68.9	83.0
N	1050	1119	1092	1189	1110	1016	1064	1102
Plag/cpx (phenocrysts)	1.4	1.9	1.1	2.5	1.8	2.6	2.3	0.8
Plag/ol (phenocrysts)	8.8	1.0	>10.0	1.3	>10.0	>10.0	>10.0	1.4

Notes: Modal analyses are based on >1000 point counts. For the diabasic samples indicated with an asterisk (\*), the designation of phenocrysts was set arbitrarily at greater than 200  $\mu\text{m}$ . The distinction is not significant as the samples are seriate textured. These are inequigranular, crystalline (>60%) basalts, and a complete gradation exists between coarser and finer grain sizes. The upper limit of grain size is similar to that of the larger crystals in the "basaltic" samples.

Vane shear strength was measured on selected undisturbed intervals of the core samples from Hole 835A until the sediment became too stiff (when cracking of the sediment indicated that the assumption of uniform shear by the vane was no longer valid) or degrees of rotation exceeded 90°.

Thermal conductivity was measured on undisturbed sediment cores from Hole 835A and on cut cores of lithified sedimentary rocks and basalts from Hole 835B.

The lithologic units referenced in this section are those described in the "Lithostratigraphy" section (this chapter). Results from laboratory measurements are listed in Table 13 and plotted on Figures 45 through 54.

## Index Properties

### Hole 835A

Grain density, wet-bulk density, water content, porosity, and void ratio for sediments and sedimentary rocks from Hole 835A are plotted vs. depth in Figure 45, and values for the gravimetrically determined index properties are listed in Tables 13 and 14.

The index properties are of little help in discriminating between sedimentary units at this site, as the measured values show little change with depth throughout the section. At 135 mbsf, a change in sediment character is suggested by an increase in the water content, porosity, and void ratio and a slight decrease in bulk density. The grain density (Fig. 45) averages 2.73 g/cm<sup>3</sup>. A linear increase of about 0.1 g/cm<sup>3</sup> occurs between the top and the bottom of the sedimentary sequence. The bulk density for cores throughout Hole 835A (Fig. 45) averages 1.48 g/cm<sup>3</sup>. An increase

from about 1.45 to 1.5 g/cm<sup>3</sup> occurs within the first 20 mbsf; below that the density values increase only slightly from the top to the bottom of the hole. Small increases from the average between 50 and 60 mbsf and between 125 and 150 mbsf may correlate with the increase in volcanic glass (see "Lithostratigraphy" section, this chapter). Below 150 mbsf, the few bulk density measurements suggest a trend of decreasing density. Together with the corresponding increases in water content, porosity, and void ratio at the same point, this suggests that there is a less competent layer at the base of the sedimentary section.

Of these index properties, water content values (weight of water/weight of sediment; Fig. 45) fall mainly between 100% and 140%, averaging 123%. Porosity values (volume of voids/total volume; Fig. 45) lie mainly between 75% and 85%, averaging 79%. Void ratio (volume of voids/volume of sediment; Fig. 45) ranges between 3 and 5.

Lithified sedimentary rocks were recovered from Cores 135-835A-17X and -18X; two samples from these cores have index properties that are similar to those in the overlying unlithified section.

The GRAPE bulk density measurements have been processed and averaged at 5-cm intervals to remove spurious data points caused by core-section ends and void spaces within the core. The GRAPE density data (Fig. 46) average 1.51 g/cm<sup>3</sup> and also show little increase with depth. The low-density excursions on the GRAPE record mainly reflect voids or end effects not removed by the routine data processing. The GRAPE values show more variation around the mean below 120 mbsf than in the upper parts of the section, possibly reflecting the presence of ash layers and an increased volume of volcanic glass.

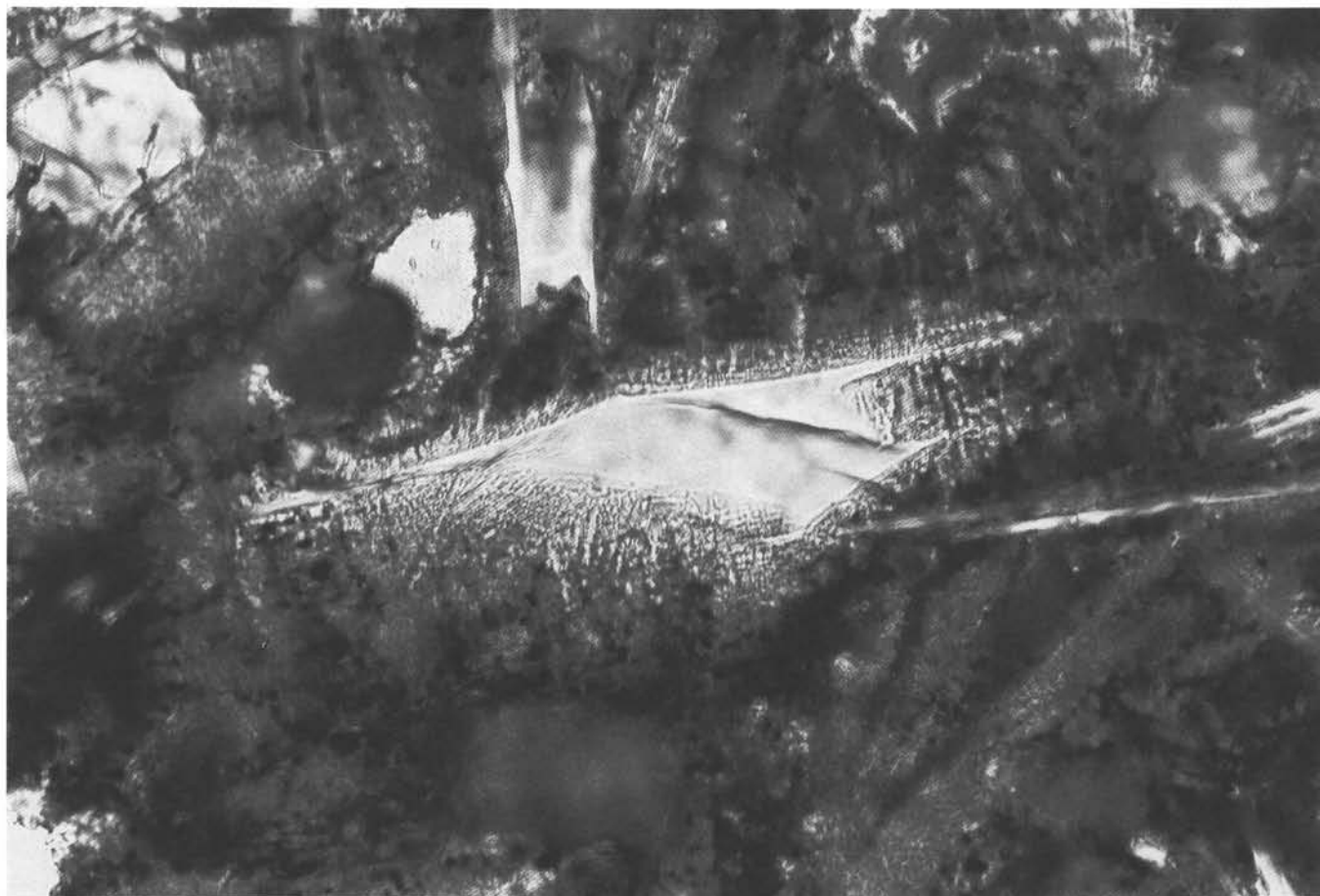


Figure 41. Quench "swallow-tail" plagioclase microlite in microcrystalline mesostasis; Sample 135-835B-7R-3, 137–140 cm, Piece 14; mesostasis also shows fine skeletal intergrowth textures; field of view = 0.3 mm, plane polarized light.

### Hole 835B

Lithified sedimentary rocks and basalts were recovered from Hole 835B. For sedimentary rocks, the index properties were determined by the standard gravimetric techniques. For basalts, the bulk density was determined using 2-min GRAPE procedures. The grain density was measured by powdering samples of basalt, drying these samples for 24 hr at 110°C, and determining weight and volume with a balance and pycnometer (see "Explanatory Notes" chapter, this volume). These data are presented in Table 14.

For the lithified sedimentary rocks from Cores 135-835B-2R and -3R, the bulk densities of four measured samples average 1.58 g/cm<sup>3</sup> and ranged from 1.55 to 1.6 g/cm<sup>3</sup>, substantially higher than in the overlying unlithified sediments. The grain density averages 2.69 g/cm<sup>3</sup>, and the porosity, water content, and void ratio for these four samples are all lower than in the overlying section, as expected from the greater degree of lithification.

The bulk density for four basalt samples averages 2.56 g/cm<sup>3</sup> and ranges from 2.37 to 2.82 g/cm<sup>3</sup>, whereas grain densities average 3.04 g/cm<sup>3</sup> and range from 2.98 to 3.14 g/cm<sup>3</sup>. For comparison, average results for basalts are a bulk density of 2.74 g/cm<sup>3</sup> and a grain density of 3.01 g/cm<sup>3</sup> (Johnson and Olhoeft, 1984), and for the basalts at Site 834, the averages were 2.67 and 2.94 g/cm<sup>3</sup> for bulk and grain density, respectively.

The limited number of samples from Hole 835B shows the expected increase in bulk and grain density and decrease in the

other index properties within the lithified sedimentary rocks and basalts. Samples are too few to distinguish trends within the basement rocks.

### Compressional Wave Velocity

Compressional wave velocity data measured with a Hamilton Frame device and the *P*-wave logger are shown in Figures 47 and 48 and listed in Tables 13 and 14.

In the sediments of Hole 835A, the compressional wave velocity is relatively constant with depth and averages 1495 m/s on both discrete samples and on the *P*-wave logger data (Fig. 48). The *P*-wave logger average excludes values below 1450 m/s, as these values are mainly caused by voids in the measured cores. However, the expanded scale and much greater number of measurements made with the *P*-wave logger allow definition of high and low values of compressional wave velocity. Higher than average values are found at about 10 and 30 mbsf, and a strong excursion is present at about 120 mbsf. These intervals either have more competent sediments or a higher carbonate content than the remaining portions of the sediment column. A significant low velocity interval between 50 and 60 mbsf may be the result of drilling or other disturbance, such as slumping. Between 10 and 95 mbsf, considerable variation around the mean is present. High values may reflect the presence of volcanic glass, small areas of indurated sediment, or clasts embedded with the matrix sediment. Low values may reflect the presence of a finer grain size than normal within the matrix sediment. Between 115 and 125 mbsf,



Figure 42. Altered cryptocrystalline mesostasis (interstitial) in Sample 135-835B-7R-2, 89–93 cm, Piece 5, that still shows fresh skeletal and swallowtail-quenched plagioclase microlites (with radiating acicular growths extending from the termination of the microlites), plus euhedral to anhedral grains of magnetite; field of view = 1.5 mm, plane polarized light.

the high velocity may result from the presence of volcanic silts and sands present in the nannofossil, clayey, mixed sediment within that interval (see “Lithostratigraphy” section, this chapter).

Basalt velocities (Table 14) on four samples average 4620 m/s and range from 4300 to 5085 m/s, values similar to the velocities measured in basalts at Site 834. Velocity measurements of the basalts were made in both horizontal and vertical directions to test for velocity anisotropy, but no significant differences were found.

#### Undrained Vane Shear Strength

Values of undrained shear strength were obtained using the standard on-board miniature vane shear apparatus on unconsolidated sediments in Hole 835A; the results are plotted in Figure 49 and reported in Table 13.

Several distinct geotechnical units defined by undrained shear strength can be distinguished in Hole 835A. The upper section from 0 to 45 mbsf is characterized by low (generally <35 kPa) shear strengths. Between 45 and about 90 mbsf, shear strengths are about 45 kPa and display considerable scatter. These values indicate a more consolidated section of the sediment column. Below 95 mbsf, shear strengths increase from about 45 to roughly 100 kPa, indicating a rapid increase in sediment strength. The upper section may correlate with the upper Pleistocene sediments identified by the micropaleontologists (see “Biostratigraphy” section, this chapter). The middle section corresponds to that portion of the sediment column disrupted by slumping and superposition of older sediment upon younger. The scatter in the data may be

caused by disruption during the high-energy slump depositional history. The lower section, defined by sharply increasing shear strengths, is Pliocene in age and much more consolidated and competent than overlying sections. Shear strength measurements were not made below this depth, because indurated sediments were encountered and the capacity of the vane shear instrument was exceeded. The index properties indicate a region of higher water content, porosity, and void ratio immediately below this high-shear-strength region, which suggests that the shear strength probably decreases near the base of the sedimentary section.

The undrained shear strength in Hole 835A varies with the total carbonate content (Fig. 50A). As the carbonate content decreases, especially within the middle and lower sections, shear strength increases (Fig. 50B). This is especially evident in the lower section, in which carbonate content decreases from 62% to 10% and shear strength increases from 37 to 126 kPa. The decrease in foraminifers and larger nannofossils (discoasters) found in the Pliocene section has allowed the clays in this section to consolidate. Foraminifers and discoasters in a grain-supported sediment prevent significant consolidation and associated changes in physical properties, until grain crushing or dissolution occurs (Rezak and Lavoie, 1990).

#### Thermal Conductivity

In soft sediment cores, all values were obtained using needle probes inserted through core liners into full core sections. For lithified sedimentary rocks and basalts, the thermal conductivity

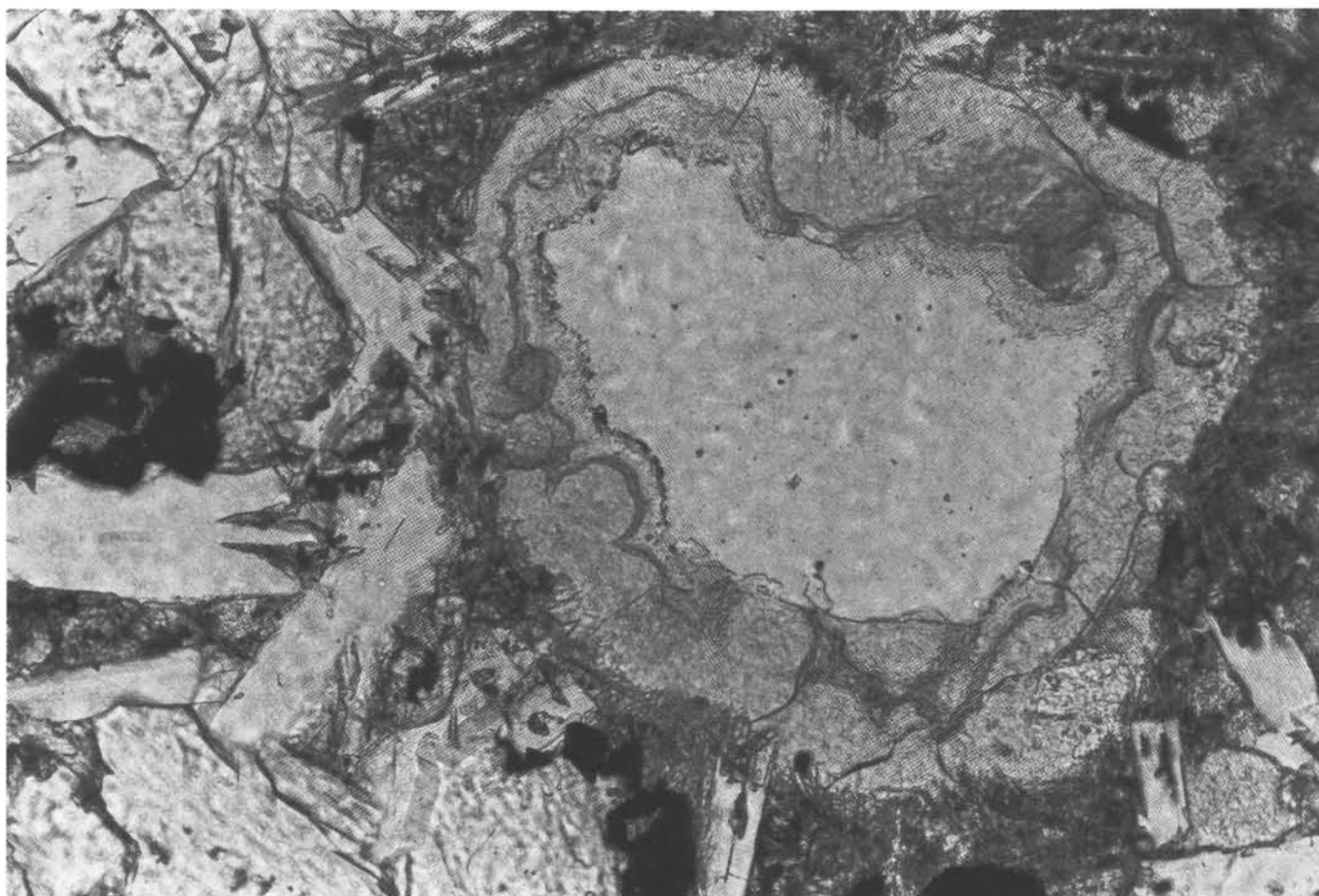


Figure 43. Vesicle infilling of smectite and zeolites in Sample 135-835B-6R-1, 111–114 cm, Piece 15; field of view = 0.6 mm, plane polarized light.

was measured on the split core face. The thermal conductivity results for both full and split cores from Holes 835A and 835B are illustrated in Figure 51 and listed in Tables 13 and 14.

Thermal conductivity in the sedimentary section of Hole 835A is fairly uniform, averaging  $0.95 \text{ W}/(\text{m} \cdot ^\circ\text{K})$ . The rather uniform conductivity through most of the hole mimics the similarly uniform index property and velocity measurements. However, a decrease in thermal conductivity occurs at the base of the hole with values as low as  $0.82 \text{ W}/(\text{m} \cdot ^\circ\text{K})$  in the lithified sedimentary rocks immediately above the basalt. This corresponds to the increased porosity and void ratio also measured in this section.

Thermal conductivity in the basalts averages  $1.47 \text{ W}/(\text{m} \cdot ^\circ\text{K})$ . Too few measurements were made to define trends within the basalts.

### Temperature Measurements

The downhole water sampler temperature probe (WSTP) was used to make temperature measurements at six points in Hole 835A. The deepest measurement was discarded because the irregular decay curve indicated that the probe was unstable in the formation. The results are shown in Figure 52. The temperature history in the sedimentary section should be such that after 5 min in the sediment, the decay curve is approximated by

$$T(t) = A/t + T_{eq},$$

where  $A$  is a constant determined experimentally,  $t$  is time, and  $T_{eq}$  is the equilibrium formation temperature (Hyndman et al.,

1987). The temperature gradient defined by these measurements is about  $1.53^\circ\text{C}/100 \text{ m}$  (Fig. 53). Thermal conductivity measurements (Fig. 51) were used to calculate thermal resistivity, and the results were integrated over depth. When the resulting thermal resistance is plotted with the temperature measurements from the WSTP (Fig. 54), the slope of the regression line indicates that the heat flow in the region is  $14.5 \text{ mW}/\text{m}^2$ . For comparison, heat flow at Site 834 was  $50 \text{ mW}/\text{m}^2$  and heat flow predicted by theoretical heat flow curves approaches  $200 \text{ mW}/\text{m}^2$  for young crust (Anderson et al., 1977).

### Discussion

The index properties show only small changes with lithology or with variations in disturbance of the lithology throughout much of Hole 835A. The lithology and biostratigraphy show that the section has been affected by slumping, with Pliocene sediments encased in Pleistocene sediments, and with disturbed zones at the base of the slump mass. The  $P$ -wave logger velocity data measurements seem to be sensitive to these disturbances in sedimentary section. For example, at 3.5 mbsf and between 30 and 40 mbsf, measured high velocities correspond with mud clasts and conglomerates (see Fig. 48 and "Lithostratigraphy" section, this chapter). These were not identified in the measurements made on discrete samples because velocity was measured on "representative" samples (e.g., the matrix sediment around the clasts and conglomerates). The prominent low velocity region between 50 and 60 mbsf corresponds to the region where both the paleomagnetic interpretation and the biostratigraphical evidence (see

**Table 12. Major and trace element analyses of representative samples from Site 835.**

Hole	835B	835B	835B	835B	835B	835B	835B
Core, section	3R-1	4R-1	6R-1	6R-1	7R-1	7R-2	Average
Interval (cm)	140-143	16-20	32-37	114-117	40-44	84-89	
Depth (mbsf)	155.70	164.16	174.02	174.84	179.10	180.85	
Major elements (wt%):							
SiO <sub>2</sub>	50.27	50.14	50.35	49.80	50.53	50.39	50.25
TiO <sub>2</sub>	1.14	1.15	1.09	1.23	1.11	1.14	1.14
Al <sub>2</sub> O <sub>3</sub>	16.63	16.43	16.47	16.17	16.59	16.22	16.42
Fe <sub>2</sub> O <sub>3</sub>	9.92	10.25	9.40	10.74	9.68	9.43	9.90
MnO	0.17	0.17	0.16	0.19	0.17	0.12	0.16
MgO	7.52	7.65	7.67	6.70	7.67	7.98	7.53
CaO	12.76	12.58	12.90	12.33	12.83	12.16	12.59
Na <sub>2</sub> O	1.95	1.79	1.82	2.19	1.81	2.11	1.94
K <sub>2</sub> O	0.24	0.24	0.28	0.21	0.23	0.12	0.22
P <sub>2</sub> O <sub>5</sub>	0.13	0.12	0.11	0.12	0.10	0.11	0.11
Total	100.71	100.50	100.23	99.66	100.70	99.77	100.26
LOI	0.67	0.75	0.60	0.35	0.51	0.83	0.62
Mg#	60.0	59.6	61.8	55.3	61.1	62.6	60.0
Trace elements (ppm):							
Nb	0	1	1	1	1	1	1
Zr	46	45	44	49	45	45	46
Y	23	23	22	25	22	22	23
Sr	135	135	130	135	131	131	133
Rb	4	4	5	4	3	1	4
Zn	66	63	60	62	63	63	63
Cu	87	80	81	90	85	81	84
Ni	67	69	78	60	89	73	73
Cr	161	170	179	127	179	155	162
V	276	274	268	287	276	269	275
Ce	6	9	7	6	9	7	7
Ba	40	41	42	64	29	36	42

Note: Mg# represents  $100 \cdot (\text{Mg}/[\text{Mg} + \text{Fe}^{2+}])$  where  $\text{Fe}^{3+}/\text{Fe}^{2+}$  is assumed to be 0.2. LOI = loss on ignition.

“Biostratigraphy” and “Paleomagnetism” sections, this chapter) suggest that a large raft of slump material has been cored. In addition to disturbances, velocity is related to grain size and sediment type. The high velocity measured on the *P*-wave logger between 115 and 125 mbsf corresponds roughly to a region of nanofossil, clayey, mixed sediment with volcanic sand and silt. Beds of sand- and silt-size particles have a higher velocity than the clay matrix that comprises much of the sediment.

The relatively stable water content, porosity, void ratio, and density, coupled with the very low thermal gradient measured at Site 835, suggest that fluid circulation within the sediment is high, with heat dissipated by the passage of fluid through the section. The absence of the expected negative gradient in these index properties within the deep portions of the sediment column suggests that the fluid is carrying a significant portion of the overburden load, preventing consolidation of the sediment. Below 150 mbsf, the water content, porosity, and void ratio increase and the density decreases. This means that the sediments below 150 mbsf are more saturated than above 150 mbsf. This sedimentary section below 150 mbsf may act as a lateral conduit for fluid passage.

The measured thermal gradient and the calculated heat flow at Site 835 are lower than measured at Site 834. Site 835 is closer to the active ridge than Site 834, and the thermally driven fluid circulation may be correspondingly higher. The cool temperatures and the similarity of pore-water chemistry throughout the hole (see “Inorganic Chemistry” section, this chapter) support the premise that active exchange between the sediments and seawater is occurring and that Site 835 resides in an active convection region.

## DOWNHOLE MEASUREMENTS

### Operations

Logging operations at Hole 835B began at 0200 hr UTC on 3 January 1991 and ended at 1600 hr UTC. The driller's mud line was at 2916.5 mbrf, and the driller's total depth was 183.0 mbsf. After conditioning the hole with a short wiper trip, the bit was released and the end of the drill pipe was pulled up to 82.6 mbsf. Because this hole was much shallower than Hole 834B, the decision was made to break the quad-tool combination down to two tool strings: the seismic stratigraphic tool string and the lithoporosity combination string, both carrying the Lamont-Doherty Geological Observatory (L-DGO) temperature logging tool. Well-logging operations at Hole 835B consisted of three logging runs using the FMS logging string, the seismic stratigraphic string, and the lithoporosity string.

The first logging run with the FMS string was stalled by a natural gamma-ray tool failure on the surface. The tool was replaced and the tool string was then lowered to a total depth of 172.6 mbsf. Pass 1 was recorded up to 74.7 mbsf. The driller raised the pipe one stand (30 m) near the end of the logging pass. The tool string was lowered to the bottom of the hole and Pass 2 was also recorded openhole from 172.6 to 74.7 mbsf. The logging speed for both passes was 488 m/hr (1600 ft/hr).

The second logging run used the seismic stratigraphic tool string which includes the long-spaced sonic, the phasor induction, and the natural gamma ray tools, plus a three-arm caliper to center the tool string in the hole. This tool string measures: (1) compressional sound wave velocity through rocks and sediments sur-

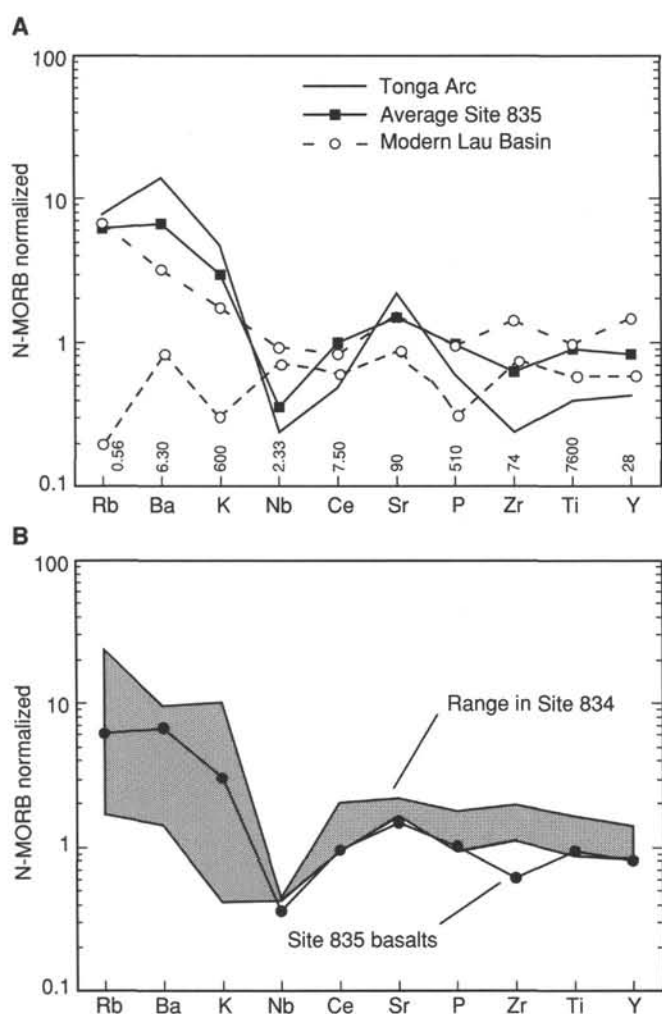


Figure 44. N-MORB normalized trace element diagrams illustrating (A) a comparison between the trace element signatures of Site 835 basalts, modern Lau Basin spreading center basalts, and average Tonga Arc rocks (excluding Ata), and (B) the trace element characteristics of Site 835 basalts compared with the range observed in rocks from Site 834. Normalizing values are from Sun and McDonough (1989) and are given in Figure 44A. The average Tonga Arc values (excluding Ata) are from Ewart and Hawkesworth (1987). The upper range for average modern Lau Basin spreading center (the CLSC) composition is from Ernewein et al. (in press) and the lower limit (from the CLSC) is for Samples STO-64-1 and STO-64-3 from Hawkins and Melchior (1985).

rounding the borehole, (2) resistivity, which is sensitive to the porosity and the conductivity of the pore fluids, and (3) the natural gamma ray response, which is sensitive to the natural radiation emitted by the rocks surrounding the borehole. The logging run with the seismic stratigraphic tool string recorded a down log from 90.4 to 170.0 mbsf, followed by a main up log from 172 to 73 mbsf, then another up log from 172 to 52 mbsf. The up logs were recorded at 457 m/hr (1500 ft/hr).

The third tool string, the litho-porosity combination, consists of a high-temperature lithodensity tool, a compensated neutron porosity tool, and a natural gamma ray tool. This combination measures density, porosity, and gamma-ray response, and carries a caliper (maximum hole diameter of 48 cm or 19 inches). The litho-porosity tool run consisted of two passes, both run up hole from 171 to 74.7 mbsf. The logging speed for both passes was 396

to 457 m/hr (1300 to 1500 ft/hr). On this run, the batteries in the L-DGO temperature tool shorted out and no temperature data were collected.

The geochemical tool string and borehole televiewer were not run in this hole because the primary target for these tools was igneous basement, and the shallow basement penetration (28 m) precluded their use.

### Onboard Processing and Data Quality

Depths were converted from feet below rig floor to meters below seafloor, and the sonic data were converted to velocity in km/s. The logging speeds were too high (greater than 274 m/hr or 900 ft/hr) on all three runs to get reliable values from the gamma ray tool for computing individual thorium, uranium, and potassium curves.

FMS data were processed onboard the JOIDES *Resolution* using a VAXstation 3200 and proprietary Schlumberger software. The data were converted from feet to meters and shifted to meters below seafloor, inclinometry and speed corrections were applied and then the data were equalized and normalized. FMS images were successfully produced for the hole from 168 to 75 mbsf. Data from 172.6 to 168 mbsf at the bottom of the hole are unusable because the diameter of the hole was greater than about 40 cm (15.5 in), and the FMS pads did not make sufficient contact with the borehole walls.

### Results and Interpretation

A selection of the results of the logging of Hole 835B is shown in Figure 55. The sediment section at the site consists of two units: lithologic Unit I (0–130 mbsf) is clayey nannofossil ooze, and lithologic Unit II (130–154.5 mbsf) consists of volcanic sand and silt (see “Lithostratigraphy” section, this chapter). These units overlie basalt, which was reached at a depth of 154.5 mbsf. The logs do not record data from all of Unit I (see depths above), but do give data for all of Unit II. Most logs measured data in only the uppermost part of the igneous basement section. The boundaries between Units I and II, and between Unit II and the igneous basement are marked by changes in measured values recorded on several of the logs.

#### Caliper Log

The caliper log records the diameter of the hole and is useful in evaluating whether information from some of the logs is valid. At Hole 835B, the caliper log (Fig. 55) shows that the hole diameter is well under 39.4 cm (15.5 in.), and that the roughness of the hole is low with few washouts (widening of the hole). The FMS caliper further shows that the hole is elliptical from 72 to 150 mbsf, circular from 150 to 155 mbsf, and slightly elliptical again from about 155 to 160 mbsf. Below 160 mbsf, the FMS calipers were at their maximum extension and the actual hole size cannot be determined. Thus, few valid FMS, lithodensity, and porosity logging data were acquired in the igneous basement.

#### Gamma-ray Log

The gamma-ray log (SGR; Fig. 55) is the only log that obtained results through the drill pipe above 52 mbsf. Because the gamma-ray tool is at the top of the tool string, the first reading for the gamma ray was 5 m above basement (at 150 mbsf) on the seismic stratigraphic run.

The resulting data can be subdivided and discussed in three depth segments: from 0 to 52 mbsf, from 52 to about 123 mbsf, and below 123 mbsf. From 0 to 52 mbsf, the gamma-ray log displays little variability. At 52 mbsf, an increase in the gamma-ray log value reflects an increase in the background value as the logging tool exited from the pipe into the open hole.

Table 13. Physical properties data, Hole 835A.

Core, section, interval (cm)	Depth (mbsf)	Su (kPa)	TC (W/[m °K])	Bulk density (g/cm <sup>3</sup> )	Grain density (g/cm <sup>3</sup> )	Porosity (%)	Water content (%)	Void ratio	V <sub>p</sub> (m/s)	V <sub>p</sub> dir.
135-835A-										
1H-2, 60	2.10		0.9245							
1H-2, 67-70	2.17			1.46	2.96	77.5	120.0	3.5	1510	C
1H-2, 85-86	2.35	2.8								
1H-3, 60	3.60		0.9657							
1H-4, 60	5.10		0.8919							
1H-4, 70-73	5.20			1.40	2.65	82.2	151.7	4.6	1504	C
1H-4, 75-76	5.25	6.1								
1H-5, 69-72	6.69			1.42	3.32	82.4	146.1	4.7	1503	C
1H-5, 75-76	6.75	6.3								
1H-6, 45-48	7.95			1.45	2.67	78.4	124.1	3.6	1589	C
1H-6, 60	8.15		0.9297							
1H-6, 116-119	8.66			1.50	2.78	81.5	125.6	4.4	1564	C
1H-6, 122-123	8.72	36.0								
2H-2, 60	11.60		0.9430							
2H-2, 68-70	11.68			1.46	2.71	78.6	123.2	3.7	1494	C
2H-2, 73-74	11.73	21.8								
2H-3, 60	13.10		0.9116							
2H-4, 49-51	14.49			1.44	2.54	80.0	132.5	4.0		
2H-4, 50-53	14.50								1514	C
2H-4, 60	14.70		0.8746							
2H-4, 95-98	14.95								1513	C
2H-4, 96-98	14.96			1.56	2.98	78.1	105.5	3.6		
2H-4, 118-119	15.18	16.2								
2H-4, 120-123	15.20								1525	C
2H-6, 60	17.70		0.9819							
2H-6, 70-73	17.70			1.49	2.68	77.7	114.8	3.5	1534	C
2H-6, 74-75	17.74	11.8							1534	C
3H-1, 75-77	19.75								1498	C
3H-2, 60	21.10		1.0167							
3H-2, 70-73	21.20			1.45	2.68	78.3	123.7	3.6		
3H-2, 75-77	21.25								1516	C
3H-2, 75-77	21.25								1312	A
3H-2, 80-81	21.30	14.0								
3H-3, 60	22.60		0.8928							
3H-4, 60	24.10		0.9059							
3H-4, 65-67	24.15			1.42	2.76	80.9	139.4	4.2	1516	C
3H-4, 72-73	24.22	15.3								
3H-6, 68-70	27.18			1.45	2.72	79.4	126.8	3.9	1497	C
3H-6, 73-74	27.23	21.8								
3H-6, 60	27.40		0.9599							
4H-2, 60	30.60		0.9276							
4H-2, 70-72	30.70								1505	A
4H-2, 70-72	30.70			1.45	2.69	80.2	130.6	4.1	1500	C
4H-2, 76-78	30.76	21.8								
4H-3, 60	32.10		0.9170							
4H-4, 60	33.60		0.9270							
4H-4, 70-72	33.70			1.46	2.68	74.5	109.3	2.9	1456	A
4H-4, 75-76	33.75	20.5								
4H-6, 60	36.60		0.9625							
4H-6, 75-76	36.75	16.2								
4H-6, 77-79	36.77			1.49	2.66	77.6	113.8	3.5	1465	A
5H-2, 60	40.10		1.0234							
5H-2, 100-101	40.50	15.3								
5H-2, 102-104	40.52			1.45	2.68	80.7	132.2	4.2	1470	A
5H-3, 60	41.60		0.9426							
5H-4, 60	43.10		0.8861							
5H-4, 70-72	43.20			1.48	2.75	79.0	121.6	3.8	1482	A
5H-4, 72-73	43.22	11.8								
5H-6, 60	46.10		0.9491							
5H-6, 90-91	46.40	14.8								
5H-6, 96-98	46.46			1.51	2.71	76.8	109.3	3.3	1453	A
6H-2, 60	49.60		0.9628							
6H-2, 70-72	49.70			1.48	2.68	81.9	131.6	4.5	1511	A
6H-2, 75-76	49.75	24.9								
6H-3, 60	51.10		0.9238							
6H-4, 60	52.60		0.9441							
6H-4, 80-81	52.80	36.7								
6H-4, 82-83	52.82	38.2								
6H-4, 84-86	52.84			1.54	2.68	76.5	103.6	3.3	1435	A
6H-4, 90-92	52.90								1509	C
6H-6, 60	54.10		0.9404							
6H-6, 74-75	55.74	41.7		1.54	2.72	77.0	104.9	3.4		
6H-6, 77-78	55.77								1510	C
7H-2, 60	59.10		1.0191							
7H-2, 91-93	59.41	12.0								

Table 13 (continued).

Core, section, interval (cm)	Depth (mbsf)	Su (kPa)	TC (W/[m · °K])	Bulk density (g/cm <sup>3</sup> )	Grain density (g/cm <sup>3</sup> )	Porosity (%)	Water content (%)	Void ratio	V <sub>p</sub> (m/s)	V <sub>p</sub> dir.
135-835A- (cont.)										
7H-2, 96-98	59.46								1508	C
7H-2, 97-99	59.47			1.44	2.70	80.1	132.3	4.0		
7H-3, 60	60.60		0.9736							
7H-4, 60	62.10		0.9004							
7H-4, 76-78	62.26	41.0		1.52	2.66	76.3	105.5	3.2	1472	A
7H-6, 60	65.10		0.9378							
7H-6, 72-74	65.22			1.45	2.67	83.0	142.1	4.9		
7H-6, 75-76	65.25	59.3							1505	C
7H-6, 82-84	65.32									
8H-2, 60	68.60		0.9964							
8H-2, 70-72	68.70			1.45	2.80	80.3	131.4	4.1	1481	A
8H-2, 75-76	68.75	29.7								
8H-3, 60	70.10		0.9449							
8H-4, 60	71.60		0.9560							
8H-4, 75-76	71.75	19.8								
8H-4, 78-80	71.78			1.47	2.71	78.8	121.3	3.7	1479	A
8H-6, 60	74.60		0.9545							
8H-6, 72-74	74.72			1.46	2.77	81.5	134.7	4.4	1477	A
8H-6, 75-76	74.75	53.0								
9H-2, 60	78.10		1.0257							
9H-2, 75-76	78.25	31.1								
9H-2, 77-79	78.27			1.50	2.78	80.3	121.9	4.1	1469	A
9H-3, 60	79.60		0.9631							
9H-4, 60	81.10		0.9375							
9H-4, 65-67	81.15								1516	C
9H-4, 68-70	81.18			1.53	2.75	81.0	117.9	4.3		
9H-4, 73-74	81.23	38.9								
9H-6, 60	84.10		0.9404							
9H-6, 73-75	84.23								1519	C
9H-6, 76-77	84.26	36.7								
9H-6, 76-78	84.26			1.50	2.71	77.5	112.0	3.5		
10H-2, 60	87.60		1.0138							
10H-2, 73-75	87.73								1514	C
10H-2, 73-75	87.73			1.50	2.70	77.2	111.5	3.4	1480	A
10H-2, 75-76	87.75	46.6								
10H-3, 60	89.10		1.0030							
10H-4, 60-61	90.60	55.1	1.0088							
10H-4, 65-68	90.65								1501	C
10H-4, 65-68	90.65			1.51	2.77	77.9	112.2	3.5	1466	A
10H-6, 60	93.60		0.9756							
10H-6, 68-70	93.68			1.48	2.82	80.0	124.6	4.0	1491	A
10H-6, 75-76	93.75	43.1								
11H-2, 60	97.10		0.9727							
11H-2, 68-71	97.18								1501	C
11H-2, 68-70	97.18			1.46	2.75	80.5	130.3	4.1	1483	A
11H-2, 75-76	97.25	36.7								
11H-3, 60	98.60		0.9097							
11H-4, 60	100.10		0.9195							
11H-4, 75-76	100.25	41.0								
11H-4, 80-83	100.30								1500	C
11H-4, 80-83	100.30			1.46	2.78	80.1	127.8	4.0	1490	A
11H-6, 60	103.10		0.9287							
11H-6, 70-73	103.20								1496	C
11H-6, 70-73	103.20			1.46	2.70	80.2	128.2	4.1	1470	A
11H-6, 80-81	103.30	41.7								
12H-2, 60	106.60		0.9341							
12H-2, 67-70	106.67								1502	C
12H-2, 67-70	106.67								1480	A
12H-2, 67-70	106.70			1.45	2.70	80.4	132.1	4.1		
12H-2, 75-76	106.75	30.4								
12H-3, 60	108.10		0.9352							
12H-4, 67-70	109.67				1484	C				
12H-4, 67-70	109.67								1460	A
12H-4, 67-70	109.70			1.48	2.80	80.9	126.7	4.2		
12H-4, 75-76	109.75	44.5								
12H-4, 60	112.60		0.9590							
12H-6, 67-70	112.67								1494	C
12H-6, 67-70	112.67								1492	A
12H-6, 67-70	112.70			1.45	2.69	79.3	128.2	3.8		
12H-6, 75-76	112.75	47.3								
13H-2, 67-70	116.17								1512	C
13H-2, 67-70	116.20			1.46	2.68	79.4	126.6	3.9		
13H-2, 75-76	116.25	31.8								
13H-2, 150	117.00		0.9989							
13H-3, 16	117.60		0.9623							

Table 13 (continued).

Core, section, interval (cm)	Depth (mbsf)	Su (kPa)	TC (W/[m °K])	Bulk density (g/cm <sup>3</sup> )	Grain density (g/cm <sup>3</sup> )	Porosity (%)	Water content (%)	Void ratio	V <sub>p</sub> (m/s)	V <sub>p</sub> dir.
135-835A- (cont.)										
13H-4, 3	118.53		1.0152							
13H-4, 67-70	119.20			1.50	2.69	75.7	106.5	3.1	1569	C
13H-4, 75-76	119.25	10.6								
13H-6, 17	121.67		0.9734							
13H-6, 87-90	122.37								1495	A
13H-6, 87-90	122.40			1.48	2.76	79.7	123.6	3.9	1513	C
13H-6, 95-96	122.45	69.9								
14H-2, 62-65	125.62								1507	C
14H-2, 67-70	125.70			1.53	2.73	78.2	110.6	3.6		
14H-2, 74-75	125.74	59.3								
14H-2, 1.5	126.50		1.0240							
14H-3, 16	126.66		0.9735							
14H-4, 3	128.17		0.9999							
14H-4, 67-70	128.67								1482	A
14H-4, 67-70	128.70			1.51	2.75	77.7	110.7	3.5	1507	C
14H-4, 75-76	128.75	83.9								
14H-6, 17	131.17		0.9177							
14H-6, 95-96	131.95	51.9								
14H-6, 99-102	132.00			1.52	2.82	77.4	109.7	3.4	1508	C
15H-2, 41-42	134.71	36.4								
15H-2, 46-48	134.76								1512	C
15H-2, 62-62	134.92		0.9766							
15H-2, 82-83	135.10			1.41	2.65	84.4	159.6	5.4		
15H-2, 103-100	135.53								1509	C
15H-2, 126-129	135.56								1490	C
15H-3, 60	136.60		0.9322							
15H-4, 69-71	137.80			1.52	2.81	80.4	117.6	4.1	1514	C
15H-4, 75-76	137.87	81.7								
15H-4, 3	138.10		0.8635							
15H-6, 76-77	140.90			1.5	2.41	71.2	94.3	2.5		
15H-6, 60	141.10		0.9475							
15H-6, 106-108	141.20			1.46	2.71	80.7	129.9	4.2		
15H-6, 115-116	141.27	58.5								
16H-2, 66-67	144.66	104.8								
16H-2, 70-73	144.70			1.47	2.83	79.6	124.1	3.9	1505	C
16H-3, 58-60	146.10			1.53	2.58	74.7	99.9	3.0		
16H-4, 70-73	147.70			1.50	2.80	80.6	122.7	4.2	1521	C
16H-4, 75-76	147.75	94.9								
16H-6, 70-73	150.70			1.42	2.77	82.8	149.1	4.8	1519	C
16H-6, 75-76	150.75	126.9								
17H-1, 10-11	152.10								1892	A
17H-1, 60	152.60		0.8200							
17H-1, 75-76	152.75								1619	C
17H-1, 75-76	152.80			1.46	2.84	85.0	146.8	5.7		
17H-1, 90	152.90		0.8405							
18H-1, 17-19	154.67								3206	A
18H-1, 20-21	154.70								1605	A
18H-1, 49-50	154.99			1.45	2.83	84.4	147.3	5.4		
18H-1, 65-68	155.15								3757	A

Notes: Su = undrained vane shear strength, TC = thermal conductivity; V<sub>p</sub> = compressional (P-wave) velocity, and V<sub>p</sub> dir. = velocity direction, where A is the vertical velocity along the core and C is the horizontal velocity perpendicular to the core face.

From 52 to 123 mbsf, some small gamma-ray variations appear to reflect sediment properties. An increase in gamma-ray values at about 56 mbsf correlates with the top of the Pliocene slump horizon discussed in the "Paleomagnetism" and "Biostratigraphy" sections (this chapter). The high values decrease downsection to the base of the slump at about 70 mbsf, then slowly increase again to another high at 80 mbsf, perhaps responding to volcanic ash layer. Below 80 mbsf, gamma values show no significant highs or lows to 123 mbsf.

The Unit I/II boundary has been identified at 130 mbsf. However, the gamma-ray values increase markedly at 123 mbsf, perhaps reflecting increased volcanic ash input that is not obvious within the cores. Unit II is marked by a slight decrease in gamma-ray values followed by a slight increase downsection to basement. Values throughout the unit are higher than in the overlying Unit

I, however, with the higher values most probably caused by the increased volcanic ash within the sediment.

#### Resistivity and Sonic Velocity Logs

The resistivity (SFLU; Fig. 55) and the sonic velocity log (VEL; Fig. 55) are similar in character. These logs show little change throughout Unit I until 118 mbsf, where the velocity and resistivity values increase slightly for 5 m at the top of the mud clast conglomerates seen in Cores 135-835A-13H and -14H. Below the conglomerate, the values decrease again. The average velocity value through Unit I is slightly higher than 1500 m/s, with an apparent increase from 1500 m/s at 54 mbsf to about 1520 m/s at the base of the unit at 130 mbsf. These velocities are similar to those measured on discrete samples and recorded by the P-wave logger (see "Physical Properties" section, this chapter).

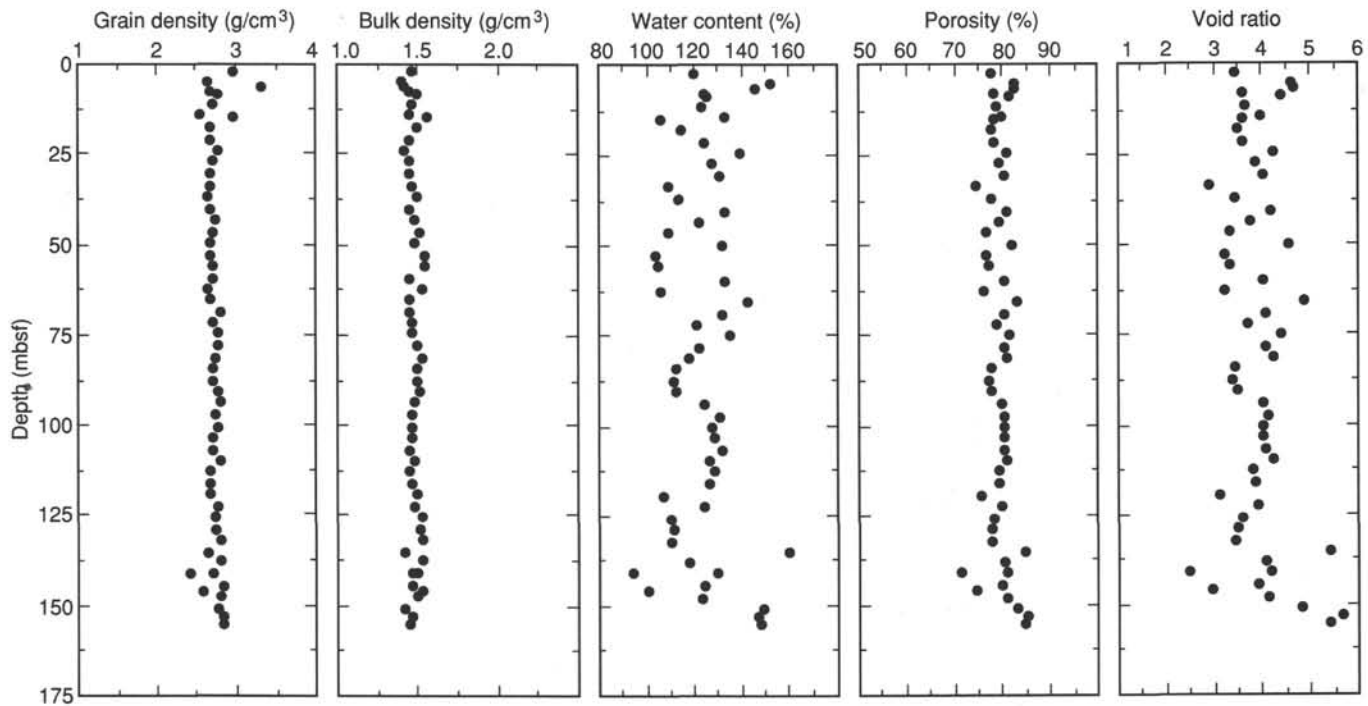


Figure 45. Index property data (grain density, bulk density, water content, porosity, and void ratio) vs. depth for the sedimentary section from Hole 835A.

Table 14. Physical properties data, Hole 835B.

Core, section, interval (cm)	Depth (mbsf)	TC (W/[m <sup>2</sup> K])	Bulk density (g/cm <sup>3</sup> )	Grain density (g/cm <sup>3</sup> )	Porosity (%)	Water content (%)	Void ratio	$V_p$ (m/s)	$V_p$ dir.
135-835B-									
2R-1, 35-37	145.05							1906	C
2R-1, 39-40	145.09							1837	C
2R-1, 40-41	145.10		1.55	2.57	73.0	93.5	2.7	1866	C
3R-1, 23-24	154.53		1.60	2.67	74.7	91.9	3.0	2031	B
3R-1, 23-24	154.53							2039	C
3R-1, 44-46	154.74							2204	A
3R-1, 52-54	154.82							2136	A
3R-1, 71-72	155.01							2001	A
3R-1, 77-78	155.07		1.6	2.69	71.2	83.5	2.5	2237	C
3R-1, 77-78	155.07							2112	A
3R-1, 113-115	155.43		1.56	2.81	78.7	106.2	3.7	2134	C
3R-2, 14-16	155.88		2.54	2.98				4276	A
3R-2, 14-16	155.88							4290	B
3R-2, 14-16	155.88							4541	C
4R-1, 16-18	164.16		2.37	3.00				4580	A
4R-1, 16-18	164.16							4597	B
4R-1, 16-18	164.16							4476	C
4R-1, 92-108	164.92	1.4785							
6R-1, 71-73	174.41			2.49	3.14			4634	A
6R-1, 71-73	174.41							4677	B
6R-1, 71-73	174.41							4626	C
7R-1, 45-47	179.15							4506	C
7R-1, 60-66	179.30	1.5089							
7R-2, 85-87	180.86							4408	C
7R-3, 100-110	182.49	1.4187							
7R-3, 110-112	182.59			2.82	3.04			5106	A
7R-3, 110-112	182.59							5193	B
7R-3, 110-112	182.59							4956	C

Notes: TC = thermal conductivity,  $V_p$  = compressional (P-wave) velocity, and  $V_p$  dir. = velocity direction, where A is the vertical velocity along the core, B is the horizontal velocity parallel to the cut core face, and C is the horizontal velocity perpendicular to the core face.

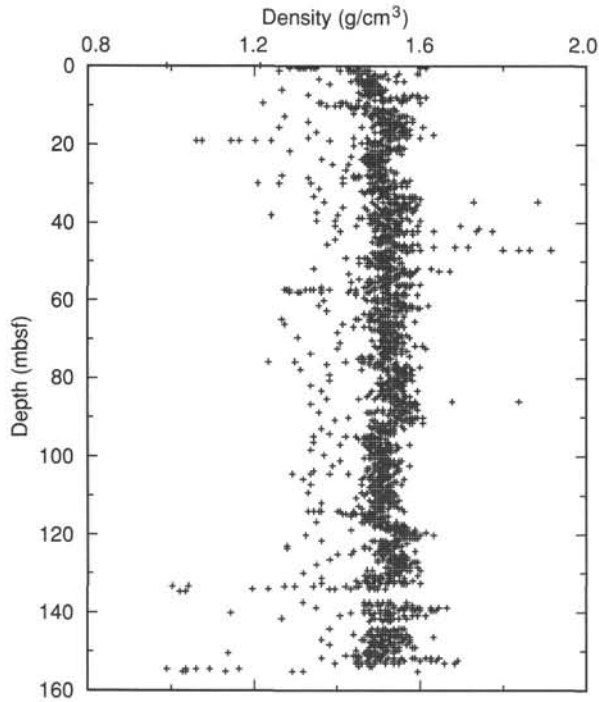


Figure 46. GRAPE bulk density vs. depth, Holes 835A and 835B. Average GRAPE bulk density is similar to the bulk density measured on discrete samples illustrated in Figure 45.

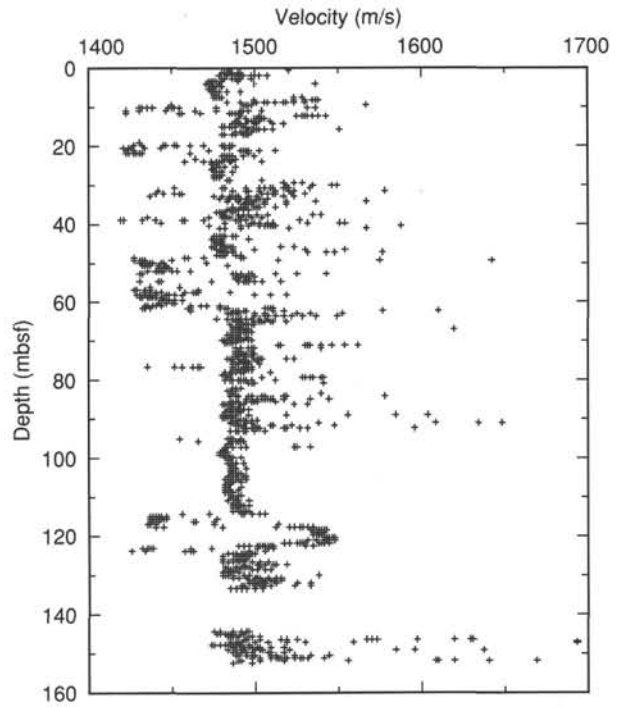


Figure 48. P-wave logger data vs. depth, Holes 835A and 835B.

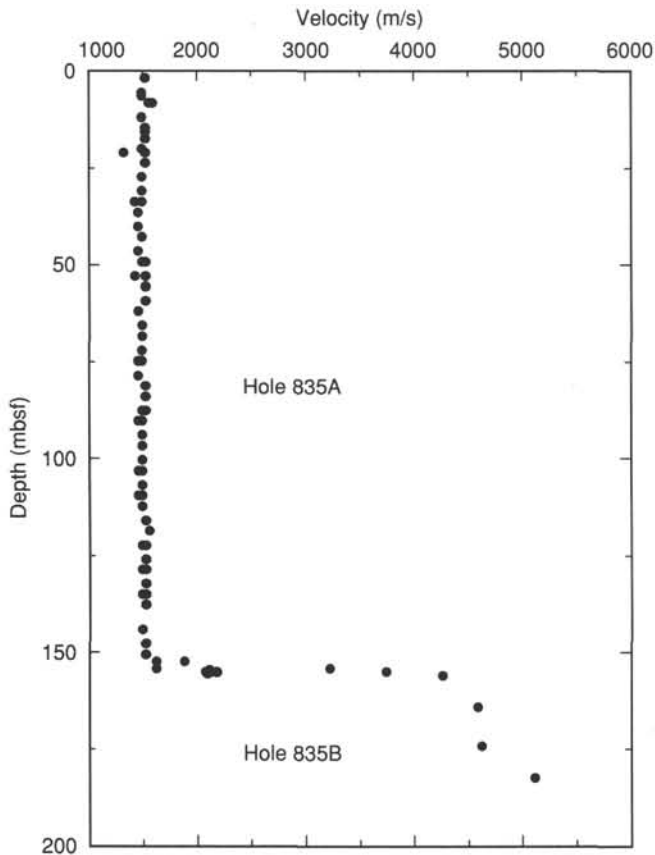


Figure 47. Compressional velocity vs. depth, Holes 835A and 835B.

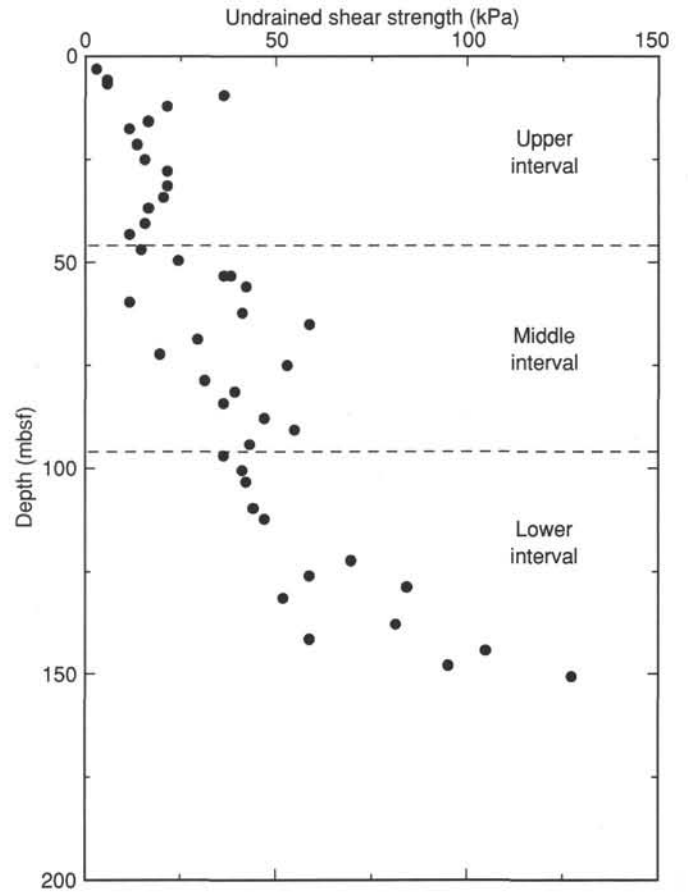


Figure 49. Undrained shear strength vs. depth, Hole 835A. Dashed lines separate the upper, middle, and lower intervals of shear strength discussed in the text.

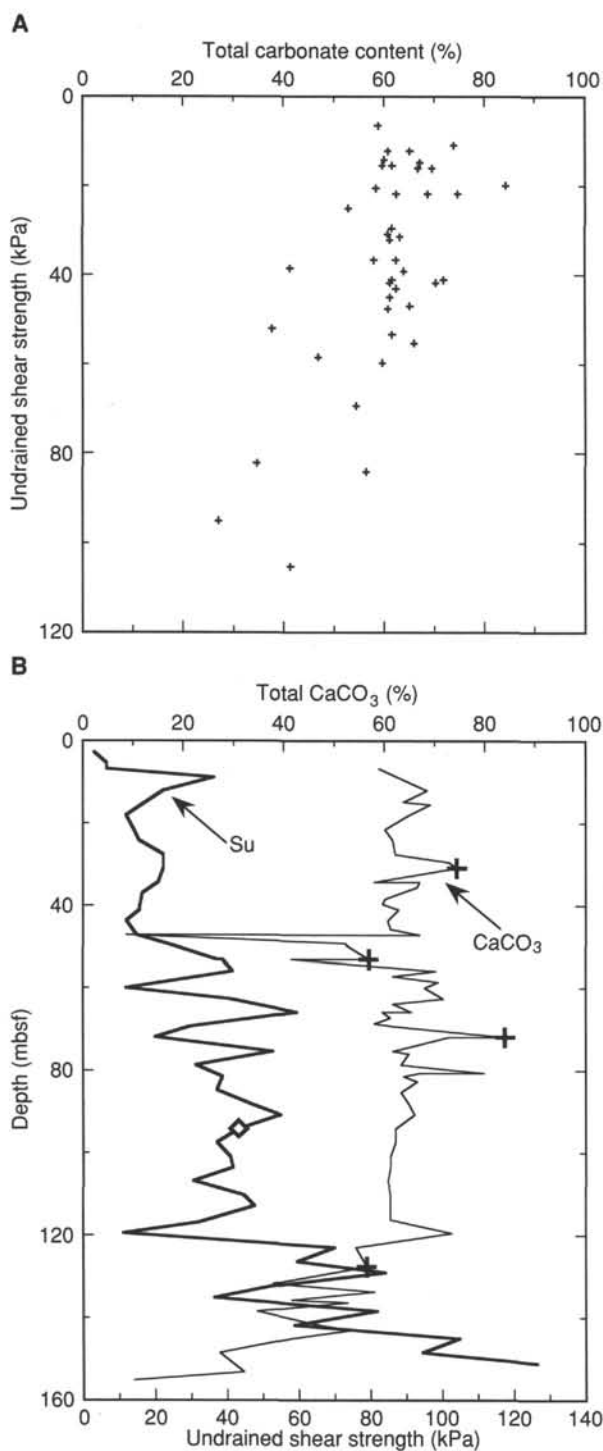


Figure 50. A. Correlation between shear strength and total carbonate content, Site 835. B. Shear strength and total carbonate content vs. depth, Site 835.

Both logs show a slight increase in values at the top of Unit II, with the velocity increasing to an average of about 1550 m/s on the velocity log. Within Unit II, a small increase in values is present between 139.5 and 141.5 mbsf. The caliper log at this point also shows a 7.5-cm (3 in.) increase in the hole size, so the corresponding velocity and resistivity increases could be simply

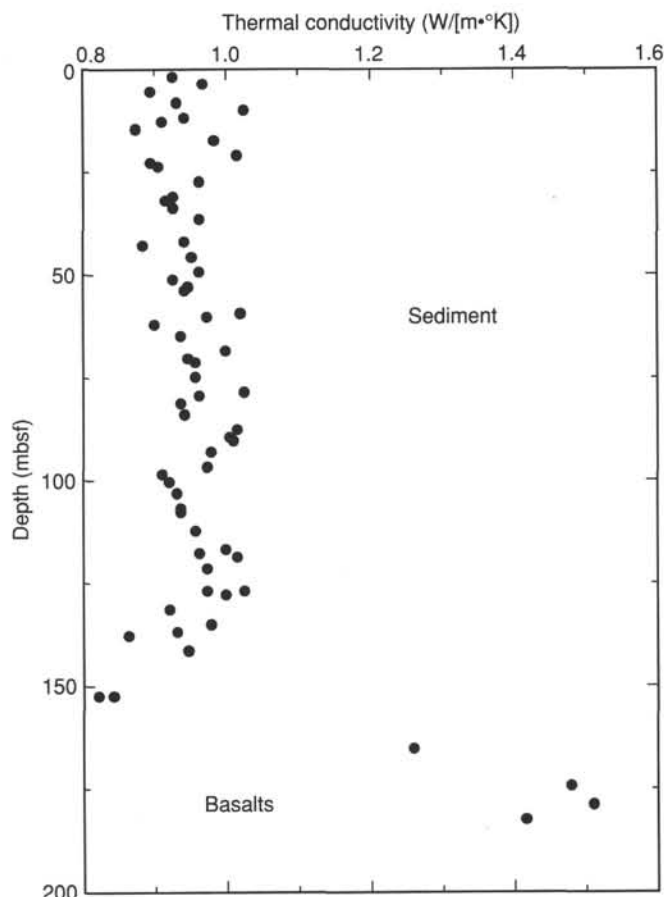


Figure 51. Thermal conductivity vs. depth, Hole 835A.

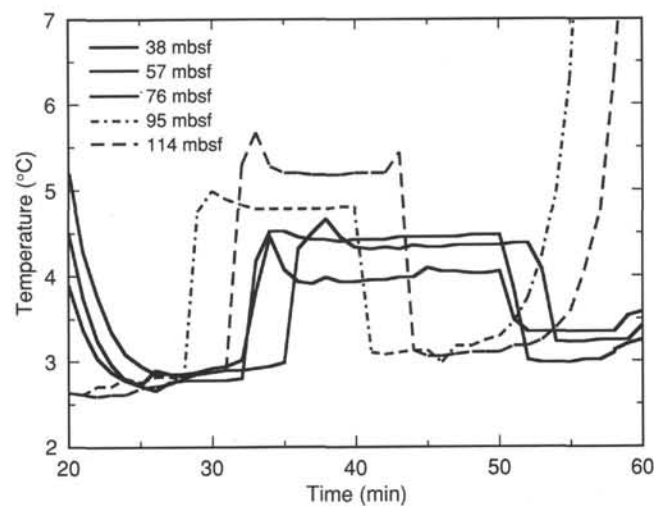


Figure 52. Heat flow measurements, Holes 835A and 835B, from various depths, based on WSTP temperature runs.

a result of this change in borehole diameter. However, hole conditions in general are a consequence of rock properties and drilling conditions, and variations in hole size may correlate with lithologic changes. The increases in velocity and resistivity values occur at the same stratigraphic level as a vitric ash layer seen in Unit II in Section 135-835A-15H-6 (at 141.39 mbsf), and the

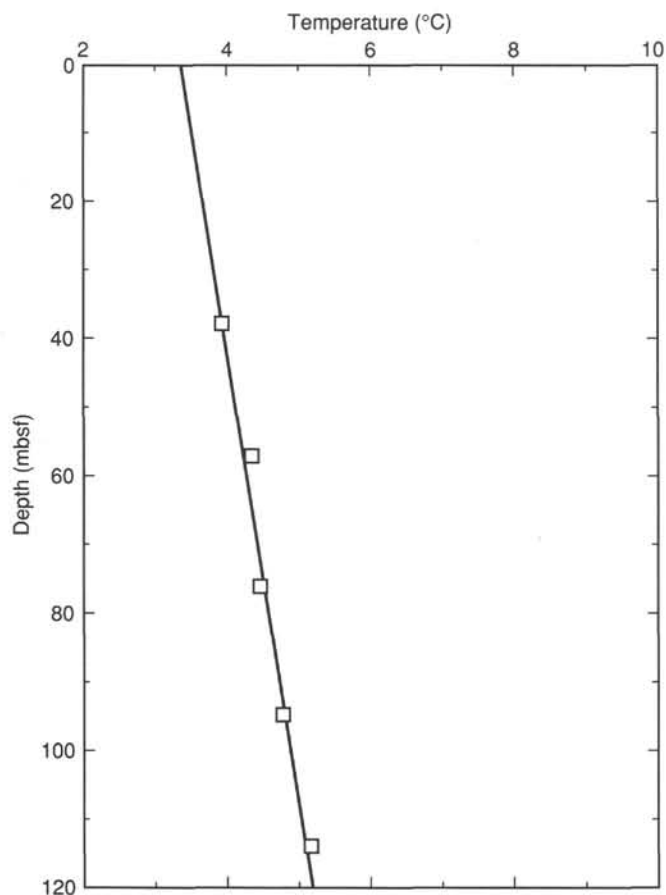


Figure 53. Temperature gradient vs. depth, Holes 835A and 835B. The line through the values indicates a geothermal gradient of 1.53°C/100 m.

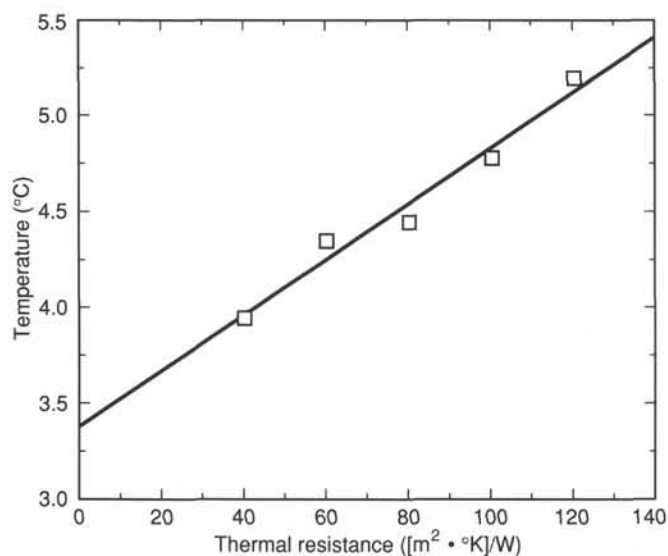


Figure 54. Thermal resistance vs. temperature, Hole 835A. The slope of the line indicates the magnitude of the heat flow for this site, which is 14.5 mW/m<sup>2</sup>.

increases could be related to this change in lithology. Small increases in velocity and resistivity occur between about 149.5 and 151 mbsf. A large increase in both velocity and resistivity values begins at 153 mbsf and correlates with lithified sedimentary rocks encountered just above the basalt basement.

Resistivity and some velocity values increase markedly at 154.5 mbsf and correlate with the top of the basalts. The maximum recorded velocities on the velocity log are approximately 2,060 m/s; this is significantly lower than values for discrete samples that were measured with velocities averaging 4,620 m/s. This is most likely because of increased hole diameter and rugosity in the basalt degrading the velocity data. However, the sonic velocity tool averages across a formation distance of about 0.61 m (2 ft), and the lower velocity in the sonic tool measurements could be caused by fracturing within the basalt. The measurements of velocity data with the seismic stratigraphic tool started at 159 mbsf, so no velocity data were acquired below that depth.

**Density Log**

The bulk density log (RHOB; Fig. 55) shows little variation throughout the sedimentary section. The caliper log (Fig. 55) shows that the hole size was acceptable for valid bulk density values until the bottom of the logged interval below 157 mbsf. The bulk density of Unit I ranges from about 1.4 to 1.45 g/cm<sup>3</sup>, and density values increase slightly in Unit II, ranging from about 1.45 to 1.49 g/cm<sup>3</sup>. Density values measured in these units with the on-board GRAPE system and on discrete sample density determinations varied little with depth and averaged 1.51 and 1.48 g/cm<sup>3</sup>, respectively, throughout the sedimentary section (see “Physical Properties” section, this chapter); the laboratory values are slightly greater than those recorded by the density log.

**Neutron Porosity Log**

The neutron porosity measurement (NPHI; Fig. 55) is an uncalibrated measure of porosity. An overall downhole decrease in the neutron porosity of the logged sedimentary section corresponds to the increasing consolidation and decreasing pore space of the sediments with burial. The neutron porosity values average about 65%–67%, lower than the average laboratory measured value of 79% for discrete samples.

**Formation Microscanner**

The FMS images of the sediments (Figs. 56–57, and presented in full on microfiche in the back pocket of this volume) show several light bands, ranging in thickness from 10 to 20 cm in the interval from 75 to 98 mbsf. We interpret these bands to be the ash and calcareous turbidite horizons that are interbedded with the clayey nannofossil oozes (see “Lithostratigraphy” section, this chapter) and are analogous to those seen on FMS data at Hole 834B (see Fig. 55 in “Downhole Measurements” section, “Site 834” chapter, this volume). The light bands stratigraphically overlie more homogeneous dark areas on the FMS image. At 118 mbsf, the FMS image becomes much lighter, corresponding to a more resistive sequence. This increase in FMS resistivity corresponds to the increase in resistivity and velocity at 118 mbsf that was correlated to the top of the mud-clast conglomerates seen in Cores 135-835A-13H and -14H. The FMS values become less

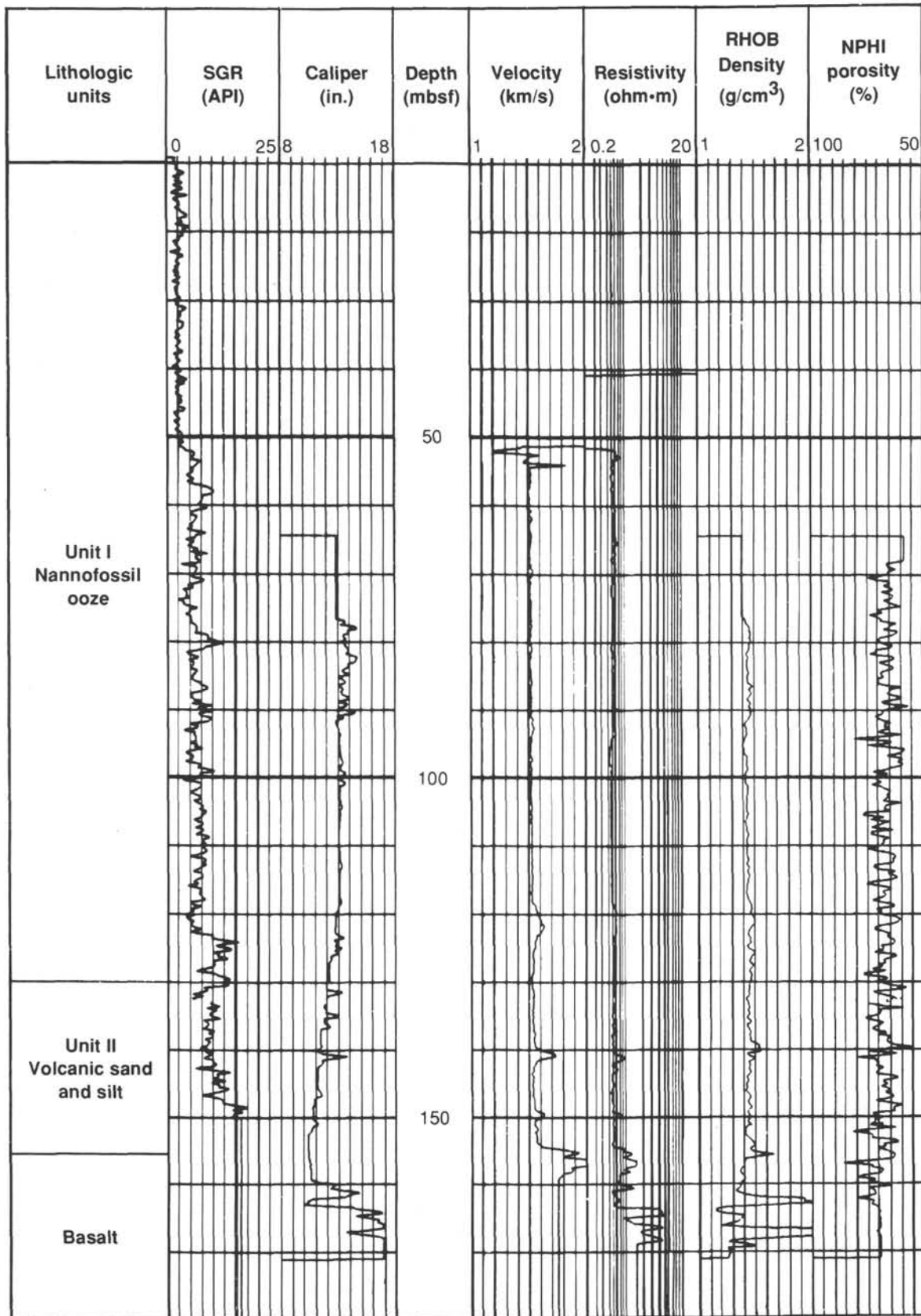


Figure 55. Quad-tool-string logs vs. depth, Site 835. The logs illustrated are as follows: total gamma ray (SGR, in American Petroleum Institute [API] units), caliper hole diameter (in inches), sonic velocity, spherically focused resistivity (SFLU, on logarithmic scale), RHOB bulk density, and NPHI neutron porosity. Lithologic units are illustrated in the left-hand column.

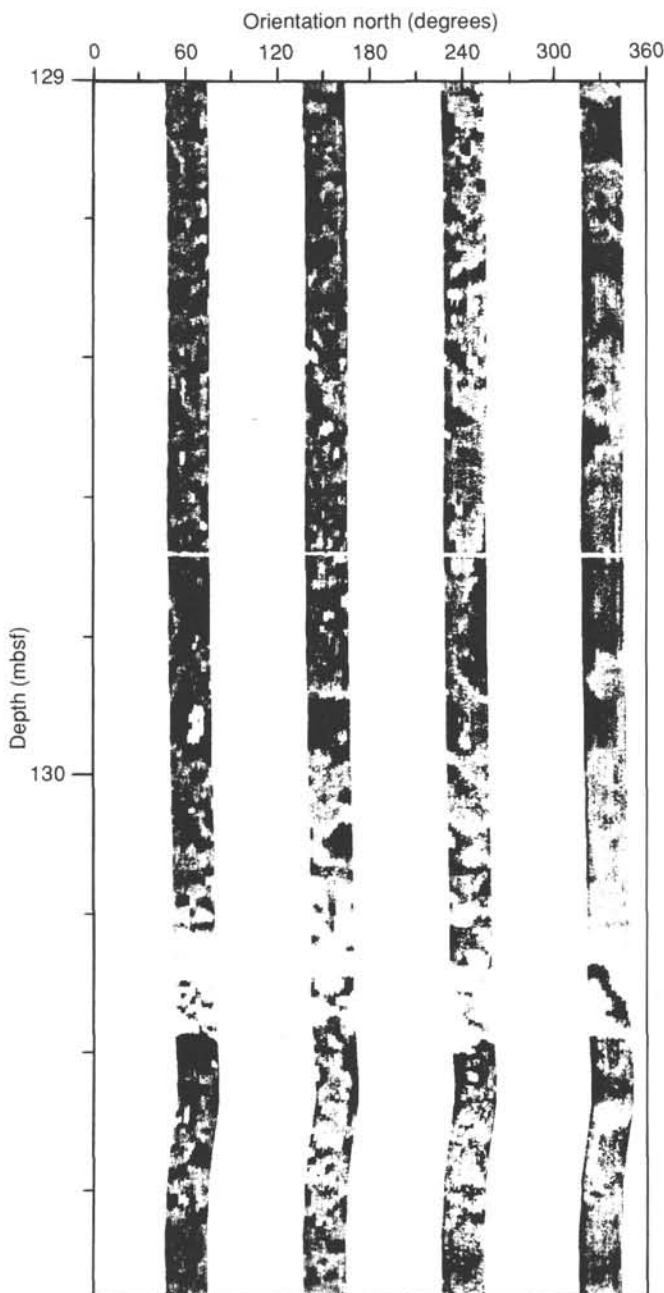


Figure 56. Formation microscanner data from 129 to about 131 mbsf, illustrating the mottled appearance of strata above 130 mbsf in Unit I and the change from Units I to II at 130 mbsf. White spots above 130 mbsf may be pumice fragments. The plot has no vertical exaggeration, and the diameter of the hole is assumed to be 24.84 cm (9.78 in., the size of the drill bit used).

resistive downsection to the base of Unit I at 130 mbsf, and this could indicate grading within the mud-clast unit. At 123 mbsf, the resistivity decreases and shows a mottled appearance on the FMS data to the base of Unit I (Fig. 56). The change at 123 mbsf corresponds to the increase in gamma-ray values. The mottled appearance could be caused by mud clasts of different composi-

tions, by volcanic ash content, or by a lack of well-defined bedding within the conglomerate.

Banding is prominent in Unit II from 130 to 154 mbsf (Fig. 57). These white bands may correlate with individual volcanic turbidite units of Unit II (see "Lithostratigraphy" section, this chapter). Increasing resistivity at the base of the sedimentary section probably reflects the increasing consolidation of the sediments just above the basalt. A greater number of bands occur between 154 and 160 mbsf and between 162 to 163.5 mbsf, below which the images are degraded because of the large borehole size.

Irregular bright patches are locally common on the FMS images (Fig. 56). These bright patches occur locally within otherwise homogeneous zones of a low-resistivity section that are thought to be brown iron-oxide/hydroxide-stained nannofossil oozes. The brighter patches also occur in more heterogeneous mottled zones in which higher proportions of the resistive material are present. The patches are tentatively interpreted as pumice fragments. Pumice fragments are common and found interspersed irregularly throughout the sedimentary succession, either isolated within nannofossil ooze or forming pumice-rich layers.

Although preliminary comparison of the FMS data with the sedimentological interpretation suggests that a close correlation between the ash horizons and the pale bands on the FMS images may be possible, the relationship does not appear to be exact; the pale horizons on the FMS images are often considerably thicker than those light-colored portions of the ash turbidite flows in the core. We suggest that the FMS image may show more of the upper fine-grained fraction of a turbidite, for example, than is readily visible in the core.

#### FMS Dipmeter Information

For Hole 835B, dipmeter processing (designated as mean-square dip or MSD) was successfully completed on data from the second pass of the tool. Figure 58 shows a processed dipmeter plot for the interval 75–160 mbsf in Hole 835B, and compares it with an equivalent presentation of dips measured from the core itself reoriented using the multishot orientation tool and paleomagnetic data (see "Structural Geology" section, this chapter). Open symbols on the dipmeter plot are dip computations with an associated empirical quality rating higher than the rejection threshold but lower than the high-quality threshold (i.e., correlations made by the program at lower levels of statistical significance than the filled symbols; see "Downhole Measurements" section, "Explanatory Notes" chapter, this volume).

Comparison of the data reveals reasonably close correlations between the manually calculated dips and those picked by the dipmeter-calculation program at, for example, 85 mbsf, and between 130 and 155 mbsf; elsewhere, however, the two sets of data differ substantially. The difference is probably largely a result of the error inherent in measuring near-horizontal strata in the core. This is discussed in more detail in the "Structural Geology" section of the "Explanatory Notes" chapter (this volume). In addition, however, the nature of the section penetrated by Site 835 lends itself to computation error (see "Downhole Measurements" section, "Explanatory Notes" chapter, this volume). An example of an erroneous MSD dip computation is illustrated in the interval 121–128 mbsf in Figure 58. This interval corresponds to a mud-clast conglomerate horizon (see "Lithostratigraphy" section, this chapter), which contains rounded clasts that may be many tens of centimeters or even a few meters in diameter. The intersection of these clasts with the borehole wall will generate what appears to be bedding but with random orientation. The dips shown on

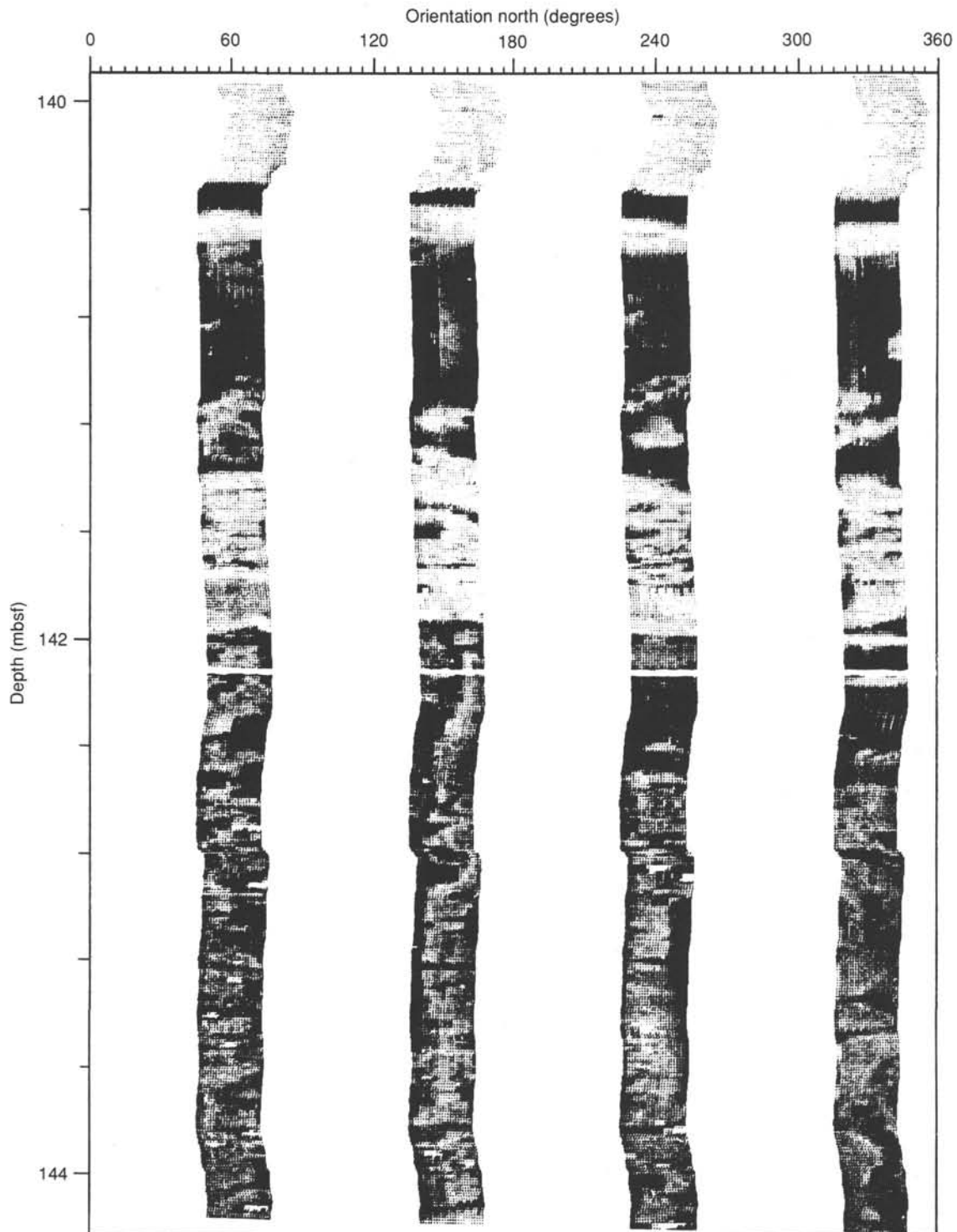


Figure 57. Formation microscanner data from 140 to 144 mbsf, illustrating the banded appearance of Unit II strata. Particularly noticeable are bands just below 140 mbsf and a wide, slightly variably resistive band just above 142 mbsf, both of which probably correlate with increased volcanic content in volcanic turbidite units. The vertical exaggeration of the plot is 4:1, with the diameter of the hole assumed to be 24.84 cm (9.78 in., the size of the drill bit used).

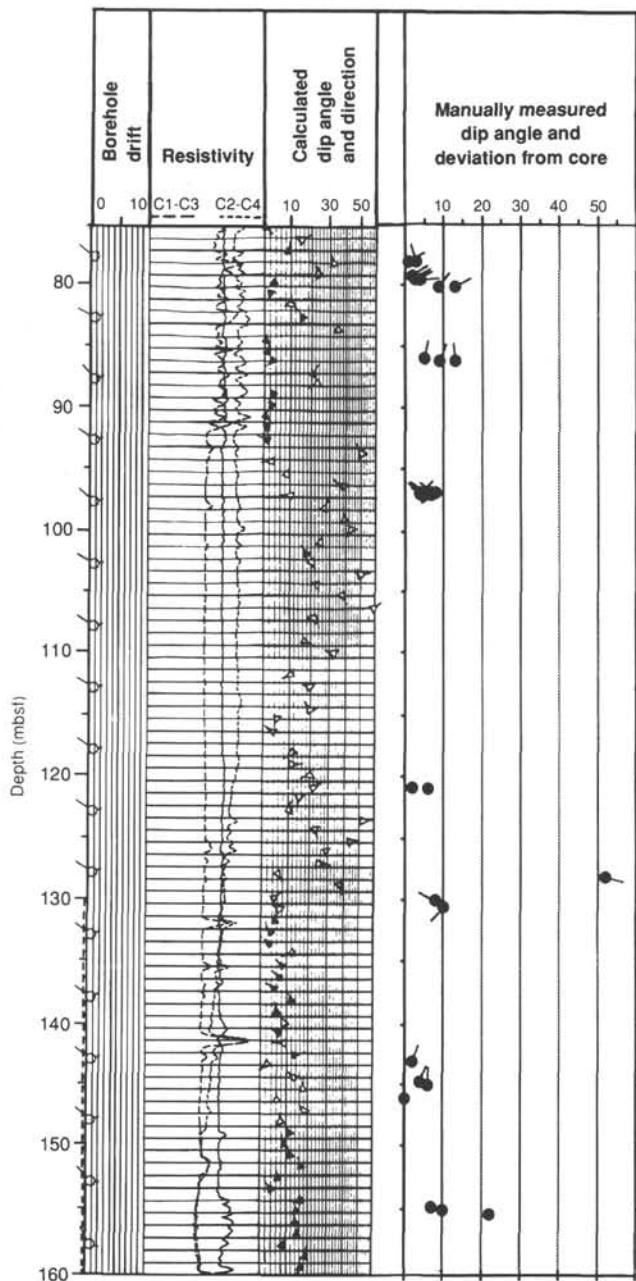


Figure 58. Calculated vs. measured dips for Hole 835B on dip vs. depth plot. The azimuth of the dip direction is indicated by a tick on the dip symbol. Dips calculated from FMS data are plotted in the center of the figure; dips measured in cores aboard the ship are plotted on the right side. The plot includes the resistivity log (solid curve, 10–0 ohms, left to right) and caliper curves (caliper C1–C3 long-dash curve on the left; caliper C2–C4 short-dash curve on the right; scale = 6–16 in., left to right). Borehole drift (dip and azimuth) is plotted on the left-hand side. The filled symbols on the calculated dips have a higher statistical significance than the open symbols, as discussed in the text.

Figure 58 at this depth are consequently steeper than elsewhere and of random azimuth.

### DISCUSSION

The objectives for Site 835 were addressed in two holes that collectively penetrated a total of 183.20 m, with a recovery of 155.2 m of sediment and 28.0 m of volcanic rock. The drilling identified the age and composition of the basement rocks; as-

essed the composition, age, and environment of deposition of the sedimentary cover sequence; and used biostratigraphic and paleomagnetic data to define a 15-m-thick allochthonous raft of Pliocene sediments that had slumped during the lower Pleistocene.

The sediment section includes two lithologic units. Unit I extends down to 130 mbsf and comprises clayey nannofossil ooze. Unit II, 130–154.5 mbsf, contains mixed sediment with volcanic silts and epiclastic ash horizons of andesitic composition. Laminated mudstones and oozes indicate gentle, low-energy deposition of this pelagic sequence, although rare crossbeds support some suggestion of increased transport energy. The lower Pleistocene, Unit I sequence is interrupted between 55 and 70 mbsf by a raft of Pliocene nannofossil ooze that appears to have slumped from the eastern inward-facing scarp bounding the basin. In the section both below and above this allochthonous block, mud-clast conglomerates occur at several levels, indicating a prolonged period of slope instability. The shallow dips of the bedding planes toward the north confirm the north-to-south sediment transport direction surmised from the regional bathymetric compilation.

The igneous basement rocks comprise a single plagioclase olivine clinopyroxene phyrlic basalt unit, the chemistry of which is clearly more arclike than that of any of the units sampled at Site 834. The presence of lithologies with arc signatures, both in the basement and in the overlying volcanoclastic deposits, demonstrates the importance of this type of volcanism in the generation of the floor of the western Lau Basin. The age of the basement at Site 835 is 3.4 Ma, corresponding to the earliest part of the 2' seafloor-spreading magnetic anomaly. This is younger than most predictions of basin age at this longitude, with the consequence that, should normal spreading have created the remaining floor to the east, the spreading rate must be significantly higher than previous models predicted. An approximate half spreading rate would have to be at least 48 mm/yr, compared to the present-day rate of approximately 30 mm/yr. We have speculated in the "Introduction and Principal Results" chapter (this volume) on several models for Lau Basin formation, but one of the least likely is that the western Lau Basin formed by "normal" seafloor spreading or, indeed, is formed entirely of MORB-like basaltic crust. The relative youth of Site 835 basement, the lack of regionally continuous magnetic "striping" in the Lau Basin, the inferred difference of the mantle source for the Site 835 basalts from a MORB mantle source, and the recognition of proximally deposited arc-derived epiclastic sediments all shed doubt on this model. The source for the volcanoclastic sediments could have been the Tofua/Tonga Arc, the Lau Ridge, or sites within the developing basin. Although andesitic basalt volcanism of the Lau Ridge Korobasaga Group (5–3.5 Ma) was in decline at the time the Site 835 basement formed, this still represents a possible candidate as a source for the clastic sediment. However, the distance between the axis of the Lau Ridge and Site 835 is presently approximately 160 km, and contrasts with that between Site 835 and the restored 2' (3.4 Ma) position of the proto-Tofua/Tonga Arc (ca. 60 km). This may preclude the Lau Ridge contribution or suggest that intrabasin arc volcanism is a more plausible source for the volcanic sediments.

### REFERENCES

- Anderson, R. N., Langseth, M. G., and Sclater, J. G., 1977. The mechanisms of heat transfer through the floor of the Indian Ocean. *J. Geophys. Res.*, 82:3391–3409.
- Berggren, W. A., Kent, D. V., Flynn, J. J., and Van Couvering, J. A., 1985. Cenozoic geochronology. *Geol. Soc. Am. Bull.*, 96:1407–1418.
- Blow, W. H., 1969. Late middle Eocene to Recent planktonic foraminiferal biostratigraphy. In Brönniman, P., and Renz, H. H. (Eds.), *Proc. First Int. Conf. Planktonic Microfossils*, Geneva, 1967. Leiden (E. J. Brill), 1:199–422.
- Bouma, A. H., 1962. *Sedimentology of Some Flysch Deposits*: Amsterdam (Elsevier).

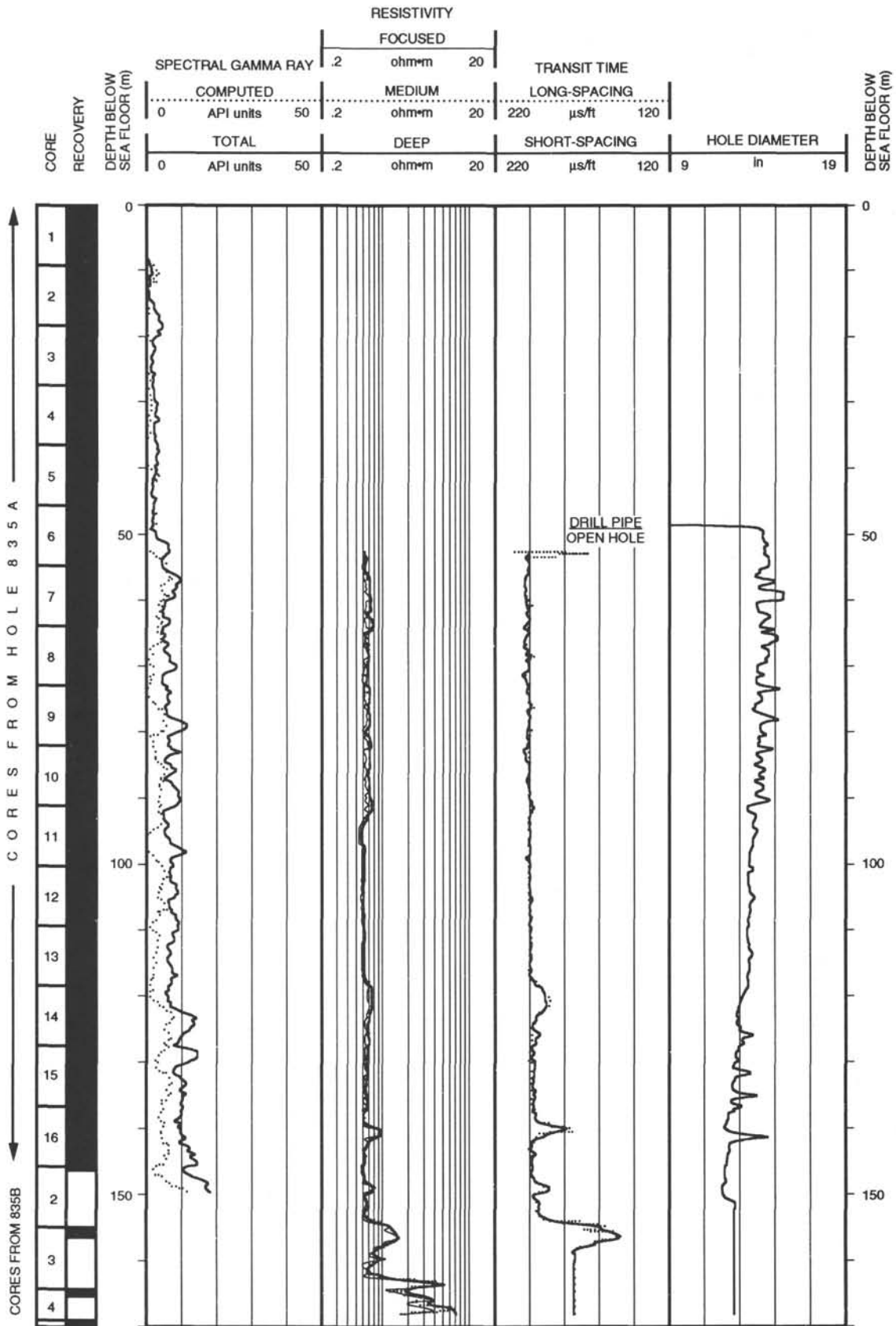
- Chaproniere, G.C.H., in press. Pleistocene to Holocene planktic foraminiferal biostratigraphy of the Coral Sea, offshore Queensland, Australia. *BMR J. Aust. Geol. Geophys.*
- Chase, C. G., 1971. Tectonic history of the Fiji plateau. *Geol. Soc. Am. Bull.*, 82:3087-3110.
- Church, B. N., and Johnson, W. M., 1980. Calculation of the refractive index of silicate glasses from chemical composition. *Geol. Soc. Am. Bull.*, 91:619-625.
- Claypool, G. E., and Kaplan, I. R., 1974. The origin and distribution of methane in marine sediments. In Kaplan, I. R. (Ed.), *Natural Gases in Marine Sediments*: New York (Plenum), 99-140.
- Clement, B. M., and Robinson, F., 1987. The magnetostratigraphy of Leg 94 sediments. In Ruddiman, W. F., Kidd, R. B., Thomas, E., et al., *Init. Repts. DSDP*, 94, Pt. 2: Washington (U.S. Govt. Printing Office), 635-650.
- Cole, J. W., Gill, J. B., and Woodhall, D., 1985. Petrologic history of the Lau Ridge, Fiji. In Scholl, D., and Vallier, T. (Eds.), *Geology and Offshore Resources of Pacific Island Arcs—Tonga Region*. Circum-Pac. Council. Energy Miner. Resour., Earth Sci. Ser., 379-414.
- Cronan, D. S., Glasby, G. P., Moorby, S. A., Thomson, J., Knedler, K. E., and McDougall, J. C., 1982. A submarine hydrothermal manganese deposit from the south-west Pacific island arc. *Nature*, 298:456-458.
- Cunningham, J. K., and Anscombe, K. J., 1985. Geology of 'Eua and other islands, Kingdom of Tonga. In Scholl, D., and Vallier, T. (Eds.), *Geology and Offshore Resources of Pacific Island Arcs—Tonga Region*. Circum-Pac. Council. Energy Miner. Resour., Earth Sci. Ser., 221-258.
- Eguchi, T., 1984. Seismotectonics of the Fiji Plateau and Lau Basin. *Tectonophysics*, 102:17-32.
- Emeis, K.-C., and Kvenvolden, K. A., 1986. Shipboard organic geochemistry on JOIDES Resolution. *ODP Tech. Note*, No. 7.
- Ernewein, M., Pearce, J. A., Bloomer, S. H., Parson, L. M., Murton, B. J., and Johnson, L. E., in press. Geochemistry of Lau Basin volcanic rocks: influence of ridge segmentation and arc proximity. *Contrib. Mineral. Petrol.*
- Ewart, A., and Hawkesworth, C. J., 1987. The Pleistocene-Recent Tonga-Kermadec arc lavas: interpretation of new isotopic and rare earth data in terms of a depleted mantle source model. *J. Petrol.*, 28:495-530.
- Gieskes, J. M., 1983. The chemistry of interstitial waters of deep-sea sediments: interpretation of Deep-Sea Drilling data. In Riley, J. P., and Chester, R. (Eds.), *Chemical Oceanography* (Vol. 8): London (Academic Press), 222-269.
- Gill, J. B., 1976. Composition and age of Lau basin and ridge volcanic rocks: implications for evolution of an interarc basin and remnant arc. *Geol. Soc. Am. Bull.*, 87:1384-1395.
- Hamburger, M., and Isacks, B., 1988. Diffuse back-arc deformation in the southwestern Pacific. *Nature*, 332:599-604.
- Harland, W. B., Cox, A. V., Llewellyn, P. G., Pickton, C.A.G., Smith, D. G., and Walters, R., 1982. *A Geologic Time Scale*: Cambridge (Cambridge Univ. Press).
- Hawkins, J. W., 1974. Geology of the Lau Basin, a marginal sea behind the Tonga Arc. In Burk, C., and Drake, C. (Eds.), *Geology of Continental Margins*: Berlin (Springer-Verlag), 505-520.
- \_\_\_\_\_, 1976. Petrology and geochemistry of basaltic rocks of the Lau Basin. *Earth Planet. Sci. Lett.*, 28:283-296.
- \_\_\_\_\_, 1988. Cruise Report—PAPATUA Expedition, Leg 04, R/V Thomas Washington. *SIO Ref. Ser.*, No. 88-14.
- \_\_\_\_\_, 1989. Cruise Report—ROUNDABOUT Expedition, Legs 14, 15, R/V Thomas Washington. *SIO Ref. Ser.*, No. 89-13.
- Hawkins, J. W., and Melchior, J. T., 1985. Petrology of Mariana Trough and Lau Basin basalts. *J. Geophys. Res.*, 90:11431-11468.
- Herzig, P. M., von Stackelberg, U., and Petersen, S., 1990. Hydrothermal mineralisation from the Valu Fa Ridge, Lau back-arc basin (SW Pacific). *Mar. Min.*, 9:271-301.
- Hyndman, R. D., Langseth, M. G., and Von Herzen, R. P., 1987. Deep Sea Drilling Project geothermal measurements: a review. *Rev. Geophys.*, 25:1563-1582.
- Johnson, G. R., and Olhoeft, G. R., 1984. Density of rocks and minerals. In Carmichael, R. S. (Ed.), *CRC Handbook of Physical Properties of Rocks* (Vol. 3): Boca Raton, FL (CRC Press), 1-38.
- Karig, D. E., 1970. Ridges and basins of the Tonga-Kermadec Island arc system. *J. Geophys. Res.*, 75:239-254.
- Malahoff, A., Feden, R. H., and Fleming, H. S., 1982. Magnetic anomalies and tectonic fabric of marginal basins north of New Zealand. *J. Geophys. Res.*, 87:4109-4125.
- Malahoff, A., Kroenke, L. W., Cherkis, N., and Brozena, J., in press. Magnetic and tectonic fabric of the North Fiji Basin and Lau Basin. In Kroenke, L., and Eade, J. V. (Eds.), *Basin Formation, Ridge Crest Processes, and Metallogenesis in the North Fiji Basin*. Circum-Pac. Council. Energy and Miner. Resour., Earth Sci. Ser.
- Mazzullo, J. M., Meyer, A., and Kidd, R., 1987. New sediment classification scheme for the Ocean Drilling Program. In Mazzullo, J., and Graham, A. G. (Eds.), *Handbook for Shipboard Sedimentologists*. ODP Tech. Note, 8:45-67.
- Munsell Soil Color Charts, 1975. Baltimore (Munsell Color).
- Murthy, S.K.M., 1990. Seafloor spreading magnetic lineations in Lau back-arc basin, southwest Pacific. *Inst. Oceanogr. Sci. Deacon Lab. Tech. Rep.*
- Nilsson, K., Florendo, F. F., and Hawkins, J. W., 1989. Petrology of a nascent triple junction, northeastern Lau Basin. *Eos*, 70:1389.
- Ninkovich, D., Sparks, R.S.J., and Ledbetter, M. T., 1978. The exceptional magnitude and intensity of the Toba eruption, Sumatra: an example of the use of deep-sea tephra layers as a geological tool. *Bull. Volcanol.*, 41:286-297.
- Okada, H., and Bukry, D., 1980. Supplementary modification and introduction of code numbers to the low-latitude coccolith biostratigraphic zonation (Bukry, 1973; 1975). *Mar. Micropaleontol.*, 5:321-325.
- Parson, L. M., et al., 1989. RRS Charles Darwin Cruise 33/88, 5 May-1 June 1988. Geophysical and geological investigations of the Lau back-arc basin, SW Pacific. *Inst. Oceanogr. Sci. Deacon Lab. Cruise Rep.*, No. 206.
- Parson, L. M., Pearce, J. A., Murton, B. J., and RRS Charles Darwin Scientific Party, 1990. Role of ridge jumps and ridge propagation in the tectonic evolution of the Lau back-arc basin, southwest Pacific. *Geology*, 18:470-473.
- Rezak, R., and Lavoie, D. L., 1990. Consolidation-related fabric changes of periplatform sediments. *Geo-Mar. Lett.*, 10:101-109.
- Rosenfeld, J. K., 1979. Ammonium adsorption in nearshore anoxic sediments. *Limnol. Oceanogr.*, 24:356-364.
- Ross, C. S., and Smith, R. L., 1955. Water and other volatiles in volcanic glass. *Am. Mineral.*, 40:1071-1089.
- Sato, H., 1979. Segregation vesicles and immiscible liquid droplets in ocean-floor basalt of Hole 396B, DSDP Leg 46. In Dmitriev, L., Heirtzler, J., et al., *Init. Repts. DSDP*, 46: Washington (U.S. Govt. Printing Office), 283-291.
- Schmincke, H.-U., 1981. Ash from vitric muds in deep sea cores from the Mariana Trough and fore-arc regions (south Philippine Sea) (Sites 453, 454, 455, 458, 459). In Hussong, D. M., Uyeda, S., et al., *Init. Repts. DSDP*, 60: Washington (U.S. Govt. Printing Office), 473-481.
- Slater, J. G., Hawkins, J. W., Mammerickx, J., and Chase, C. G., 1972. Crustal extension between the Tonga and Lau Ridges: Petrologic and geophysical evidence. *Geol. Soc. Am. Bull.*, 83:505-518.
- Sun, S.-S., and McDonough, W. F., 1989. Chemical and isotopic systematics of oceanic basalts: implications for mantle composition and processes. In Saunders, A. D., and Norry, M. J. (Eds.), *Magmaism in the Ocean Basins*. Geol. Soc. Spec. Publ. London, 42:313-345.
- von Breyman, M. T., and Suess, E., 1988. Magnesium in the marine environment: Mg-NH<sub>4</sub> ion exchange. *Chem. Geol.*, 70:359-371.
- von Stackelberg, U., 1990. R.V. Sonne Cruise SO48: summary of results testing a model of mineralisation. *Mar. Min.*, 9:135-144.
- Weissel, J. K., 1977. Evolution of the Lau Basin by the growth of small plates. In Talwani, M., and Pitman, W. C. (Eds.), *Island Arcs, Deep Sea Trenches and Back Arc Basins*. Am. Geophys. Union, Maurice Ewing Ser., 1:429-436.
- Woodhall, D., 1985. Geology of the Lau Ridge. In Scholl, D., and Vallier, T. L. (Eds.), *Geology and Offshore Resources of Pacific Island Arc—Tonga Region*. Circum-Pac. Council. Energy Miner. Resour., Earth Sci. Ser., 2:351-378.

Ms 135A-105

**NOTE: All core description forms ("barrel sheets") and core photographs have been printed on coated paper and bound separately as Part 2 of this volume, beginning on page 681.**

**Formation microscanner images for this site are presented on microfiche in the back of Part 2.**

Hole 835B: Resistivity-Sonic-Natural Gamma Ray Log Summary



Hole 835B: Density-Natural Gamma Ray Log Summary

